Universiteit Utrecht

Early middle Eocene (53 – 47 Ma) climate change in the southern Tethys

Master thesis Yannick Bats[1]

Supervisors: prof. dr. Appy Sluijs[1] and dr. ir. Francien Peterse[1]

In cooperation with: Chris Fokkema[1], Claudia Agnini[2], Agnese Mannucci[3,4], Simone Galeotti[3,4], Or Bialik[5,6] and Nicolas Waldmann[6]

1. Department of Earth Sciences, Utrecht University, The Netherlands

2. Department of Geosciences, University of Padova, Padova, Italy

3. Dipartimento di Scienze Pure e Applicate, Università degli Studi di Urbino, Italy

4. Institute for Climate Change Solutions, Via Sorchio 61040, Frontone, Pesaro e Urbino, Italy

5. Institute of Geology and Palaeontology, University of Münster, Germany

6. The Dr. Moses Strauss Department of Marine Geosciences, Charney School of Marine Sciences, University of Haifa, Israel

1. Abstract

Several paleotemperature reconstructions suggest the onset of global Cenozoic cooling started close to the early to middle Eocene transition, around 49 Ma, but the timing and magnitude of this trend remain ambiguous, particularly at low-latitudes. Moreover, Eocene hydrological change is poorly understood for (sub)tropical arid regions. To address these issues, I generated orbital-scale ocean temperature and hinterland hydrological data on lower to middle Eocene (~53 – 47 Ma) sediments deposited on the southern Tethyan slope at ~15 °N (present day Negev desert, Israel). TEX_{86} paleothermometry indicates ~1 °C sea (sub)surface cooling at 49.2 Ma, consistent with deep sea and high latitude records, suggesting changes in global greenhouse gas concentrations were likely an important driver for the onset of Cenozoic cooling. Furthermore, the TEX_{86} record shows the presence of transient warming events coinciding with previously identified carbon isotopic excursions and deep sea hyperthermals. The limited supply of terrestrial sedimentary components, including branched GDGTs, clay minerals and plant leaf wax n-alkanes indicate arid conditions, with increasing aridification throughout the early Eocene climatic optimum (EECO, ~53-49 Ma), but no detectable change over the onset of the cooling. Spectral analyses of these hydrological records show the presence of precession and obliquity forced variability, indicating the North African monsoon system was a robust feature of Cenozoic climate.

Contents

2. Introduction

2.1. The early middle Eocene climate

From the late Paleocene (~58 Ma) to Early Eocene Climatic Optimum (EECO; ~53 – 49 Ma) the global climate gradually warmed to temperatures 10 – 16 °C warmer than present (Inglis et al., 2020); Fig. 1), making the Eocene epoch (~56 – 34 Ma) the warmest period of the Cenozoic era. Palms and alligators inhabited the Arctic region, and at southern high latitudes (>60°), sea surface temperatures (SST) reached at least 30 °C during the early Eocene (Fig. 1) (e.g., Bijl et al., 2021; Eberle & Greenwood, 2012; Sluijs et al., 2009). The early Eocene was characterised by negative carbon isotopic excursions (CIE) linked to a periodic release of ^{13}C-depleted carbon into the ocean atmosphere system and shoaling of carbonate compensation depth (CCD) (Harper et al., 2020; Lourens et al., 2005; Westerhold et al., 2017; Zachos et al., 2005). Some of these CIEs have been found to correspond to superimposed transient (10^4 – 10^5-year) warming events, known as 'hyperthermals', most notably the Paleocene-Eocene Thermal Maximum (PETM; ~56 Ma) (e.g. Bijl et al., 2021; Cramwinckel et al., 2018). It has been proposed (e.g. Kirtland Turner et al., 2014; Sexton et al., 2011; Zeebe et al., 2017) the CIEs, and some associated hyperthermals, are the result of eccentricity forced global carbon cycle perturbations, and this has been validated by deep sea temperature records (i.e. benthic δ^{18}O records) on orbital resolution (e.g. Lauretano et al., 2018; Westerhold et al., 2018). Only two surface ocean temperature records have recorded hyperthermals on orbital resolution (Fokkema et al., 2023, 2024), however these records spanned only to the first half of the EECO (~52 Ma).

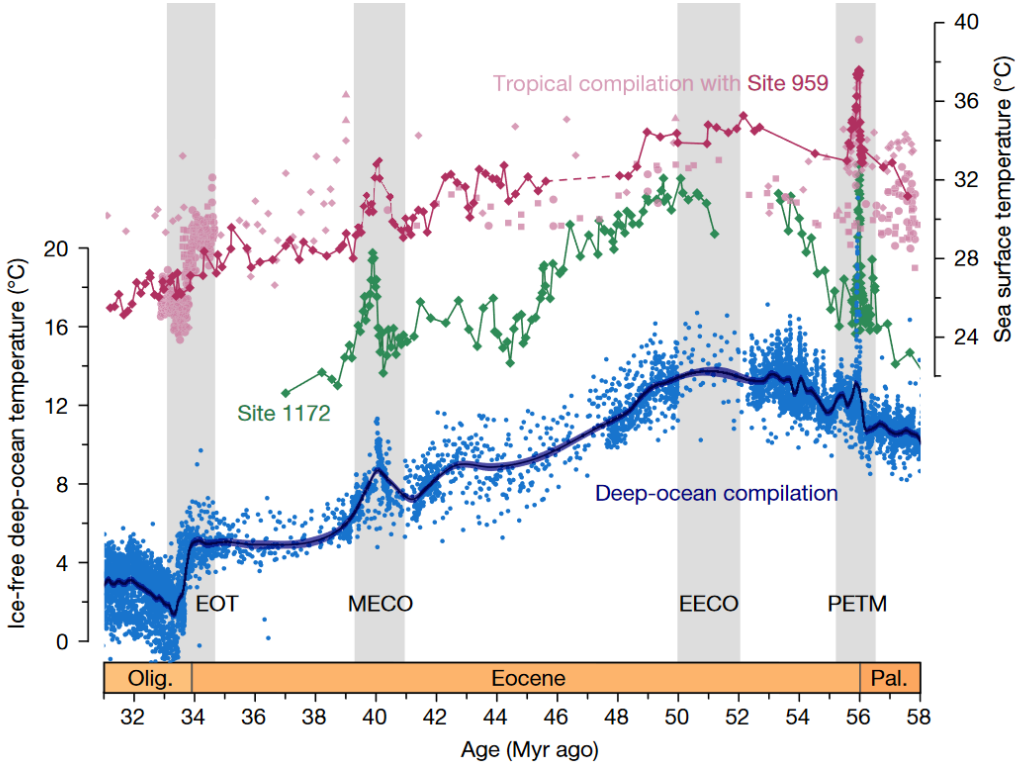

Figure 1. TEX_{86} based SST record for the tropics (purple), and southern high-latitudes (green; 60° S), and δ^{18}O based deep-ocean temperature reconstructions (blue) through time. Age follows the Geologic Time Scale 2012 (GTS2012). Pal., Palaeocene; Olig., Oligocene; EOT, Eocene–Oligocene transition. Adapted from Cramwinckel et al. (2018).

Global Cenozoic systematic cooling was initiated during the early to middle Eocene transition (~50 – 45 Ma) after the EECO. Around 49 Ma, the climate around the southern high latitudes cooled (Bijl et al., 2021). This cooling is also reflected in the deep ocean (Shackleton, 1986) and in some, but not all, records from tropical regions (Cramwinckel et al., 2018; Inglis et al., 2015; Pearson et al., 2007; Fig. 1). Therefore, it seems a systematic change during the early to middle Eocene transition forced the onset of global Cenozoic cooling.

It has been suggested (Anagnostou et al., 2016; 2020) that the onset of Cenozoic cooling was initiated by a global decrease in atmospheric pCO_2, which would have caused a global climate cooling. This cooling would have been enhanced in the higher latitudes as compared to the tropics. This is known as polar amplification, and is caused by lapse rate, water vapour and surface albedo feedback mechanisms (Lunt et al., 2012). In contrast, in apparent absence of low-latitude SST cooling (Pearson et al., 2007), Bijl et al. (2013) proposed that the opening of the Tasmanian Gateway (TG) around 50 Ma could have been the major cause of the observed synchronous onset of Antarctic cooling. TG opening would have resulted in the development of the Antarctic Circumpolar Current (ACC), isolating Antarctica in a cold water region and limiting meridional heat transport (Bijl et al., 2013; Sijp et al., 2011). This would have cooled the Southern Ocean, while heating the tropics (Sijp et al., 2011). However, a more recent record from the tropical band indeed shows cooling across the early to middle Eocene transition (Cramwinckel et al., 2018), but the timing, extent and exact cause of the presumable early middle Eocene cooling remain ambiguous. Most high resolution paleoclimatological studies on the Eocene are focused on high latitude reconstructions of the PETM and other climatic optima, as these are interesting potential analogues to the current climate change in its most extreme scenario (IPCC: RCP8.5) (Bijl et al., 2010; Carmichael et al., 2017; Sluijs et al., 2009), and therefore low-latitude paleoclimatological cover remains scarce.

2.2. Hydrological changes during the early middle Eocene

Through a decrease in convective mass fluxes, and a subsequent increase in horizontal moisture transport, it is proposed that a warmer climate globally increases the variance in the latitudinal and temporal pattern of precipitation over evaporation (*P-E)* (Held & Soden, 2006; Pierrehumbert, 2002). This implies wet regions get wetter, and dry regions get drier, as global temperatures increase. However, a recent study by Cramwinckel et al. (2023) found discrepancies between these expected and observed hydrological patterns during the Eocene. Eocene model simulations of the Deep-Time Model Intercomparison Project (DeepMIP) show inter-model differences on the response of the Mean Annual Precipitation (MAP) to changes in Global Mean Surface Temperature (GMST) for subtropical latitudes (15° – 30° N/S) (Cramwinckel et al., 2023). These differences are due to model discrepancies in the simulated latitudinal temperature gradient (LTG). Weaker LTGs result in Hadley cell strength reduction, and accordingly, partly compensate for increased subtropical moisture divergence caused by GMST increase, resulting in a higher, although still negative, simulated subtropical *P-E*. Moreover, the same study showed there is also a significant proxy-model discrepancy. Proxy-based reconstructions suggest smaller LTGs than any DeepMIP model, and coherently, higher subtropical MAP estimates (Cramwinckel et al., 2023). However, these floral-proxy derived MAP estimates are biased towards wetter regions due to the better preservation of floral assemblages in such regions, meaning the arid regions are either underrepresented in the subtropical reconstructions, or absent (Cramwinckel et al., 2023). Other proxy types (i.e. carbonate nodules and deuterium enriched leaf wax n-alkanes) do seem to be more in line with models predicting long seasonal dry periods associated with the hot early Eocene climate (Handley et al., 2012; Schmitz & Pujalte, 2007).

These model and proxy uncertainties highlight the need for additional information to further investigate the relationship between LTGs and subtropical hydrology. LTGs are naturally related to the polar amplification principle previously mentioned, confirming the need for more data on (sub)tropical (versus polar) temperature developments. Particularly, there is a strong need for data from relatively arid regions in the subtropical band.

2.3. The North African monsoon

For many subtropical places on Earth the monsoonal wet season supplies most of the annual precipitation, meaning local agriculture and food supply strongly depend on it (e.g. Monerie et al., 2013). For this reason, it is crucial to understand the response of monsoon systems to climatic changes. A monsoon is defined as the change in atmospheric circulation in response to the seasonal migration of

the tropical convergence zones (Geen et al., 2020). Monsoons are accompanied by substantial changes in precipitation due to reversals of winds, resulting in monsoonal wet and dry seasons (Geen et al., 2020). Variability in the North African monsoon system has been crucial for the state of the North African hydroclimate and vegetation. During the last ~8 million years, periods with increased latitudinal extent of North African monsoon precipitation have resulted in more than 200 intervals (~10^4-year) with savanna-type vegetation in the present-day Sahara region. These intervals are known as green Sahara periods (GSP), and seem to be largely orbitally forced (Larrasoaña et al., 2013). Furthermore, the well-recorded (~13.5 Ma – present) (quasi-)periodic formation of organic carbon rich layers called 'sapropels', in Mediterranean sediments, are likewise linked to orbitally forced changes in the North African monsoon and associated river runoff (e.g. Hilgen, 1991; Larrasoaña et al., 2003, 2013; Rohling et al., 2015, and references therein).

By focussing on seasonal extremes and differences, past monsoon systems can be studied on annual time scales. For example, Licht et al. (2014) used gastropod shells and mammal teeth to infer modern-like Indian monsoonal seasonality in $\delta^{18}O$ values (i.e. precipitation) during the late Eocene (~40 Ma). However, the examples of GSPs and sapropels have shown the importance of studying monsoon systems on orbital timescales (10^4 – 10^5-year), as the influence of Earth's orbital configurations (i.e. Milankovitch cycles) on the North African monsoon seems to be an important determining factor for the overall state of the North African hydroclimate (e.g. Bosmans, Drijfhout, Tuenter, Hilgen, & Lourens, 2015; Lourens & Tuenter, 2009).

2.3.1. Orbital forcing of the North African monsoon

Monsoon systems are orbitally forced due to associated changes in summer insolation. Northern Hemisphere (NH) summer insolation for the low latitudes is primarily determined by precession, affecting North African summer monsoon precipitation and vegetation changes (Bosmans, Drijfhout, Tuenter, Hilgen, & Lourens, 2015; Ehrmann et al., 2017; Hilgen, 1991). During precession minima, North African convergence zones reach farther north and latitudinal pressure gradients are enhanced, causing increased moisture transport towards Northern Africa. This increases precipitation and run-off into the present-day Mediterranean Sea (Bosmans, Drijfhout, Tuenter, Hilgen, & Lourens, 2015; Bosmans, Drijfhout, Tuenter, Hilgen, Lourens, et al., 2015). This effect of precession dominates over the effect of obliquity. However, obliquity forces the summer inter-tropic insolation gradient (SITIG), i.e. the difference in insolation between the northern and southern hemisphere around 23° N/S on 21 June. An enhanced SITIG determines the strength and latitudinal extent of winds and moisture transport in the summer hemisphere (Bosmans, Hilgen, Tuenter, & Lourens, 2015). So even though obliquity has negligible effect on tropical NH summer insolation, it is still an important forcing of North African monsoon variability. Eccentricity modulates the effect of precession through the amplification of seasonal contrasts (Braconnot et al., 2008). For these reasons precession (modulated by eccentricity) and obliquity signals in North African and Mediterranean hydrological records can be indicative of a North African monsoon system.

2.3.2. The Eocene North African monsoon

For the last part of the Cenozoic (~13.5 Ma – present), this orbital response is quite well understood. North African monsoon forced sapropels and vegetation changes have been thoroughly studied on orbital timescales (e.g. Hilgen, 1991; Larrasoaña et al., 2003, 2013; Rohling et al., 2015). However, for the early Eocene, the monsoon system is not as well understood due to the lack of proxy data on orbital resolution (cf. Licht et al., 2014). Nonetheless, model simulations (Huber & Goldner, 2012) show that the Eocene global monsoon system was not substantially different from the modern, with geographical differences, such as Tibetan Plateau (TP) uplift (Song et al., 2010; Wang et al., 2010), affecting local monsoon dynamics (Molnar et al., 1993), rather than the global monsoon system.

In North Africa, orbitally forced insolation changes may be a greater determinant of the regional hydroclimate than global warming or cooling (e.g., Bosmans, Drijfhout, Tuenter, Hilgen, & Lourens,

2015; Huber & Goldner, 2012; Williams et al., 2022). This suggests that the early Eocene North African hydroclimate was possibly primarily influenced by orbital forcing, with minimal effects from background climatic changes. An orbital scale Eocene pre-TP uplift North African hydroclimate record could elucidate this matter. Sediments deposited on the southern Tethys margin may offer insights into early Eocene North African monsoon dynamics, analogous to the studies done on Miocene to Holocene sapropels in Mediterranean sediments (~13.5 Ma to ~9 ka) (e.g. Hilgen, 1991; Larrasoaña et al., 2003, 2013; Rohling et al., 2015, and references therein).

2.4. This study

Above we presented the three main issues that will be addressed in this study: the need for an orbital-scale low-latitude temperature record during the early to middle Eocene transition, the associated long-term hydrological change, and the orbital forcing of the early Eocene North African hydroclimate. This study aims to shed light on these issues, using a sedimentary sequence recovered in the RH-323 core, from the Negev region in Israel (Fig. 2) (Fokkema et al., 2022). The sediments, marls, cherts and chalks, accumulated in the southern Tethys on the northern continental slope of Africa during the late Paleocene and early to middle Eocene, around 59 – 45 Ma (Fokkema et al., 2022). Previous geochemical analyses indicate that they are suitable for various paleoclimatological proxies (Fokkema et al., 2022). Recent analyses (Fokkema et al., 2024; Chapter 6) of this material have shown the presence of biomarkers including isoprenoid and branched glycerol dialkyl glycerol tetraethers (GDGTs) which can be used for paleoclimatological reconstructions.

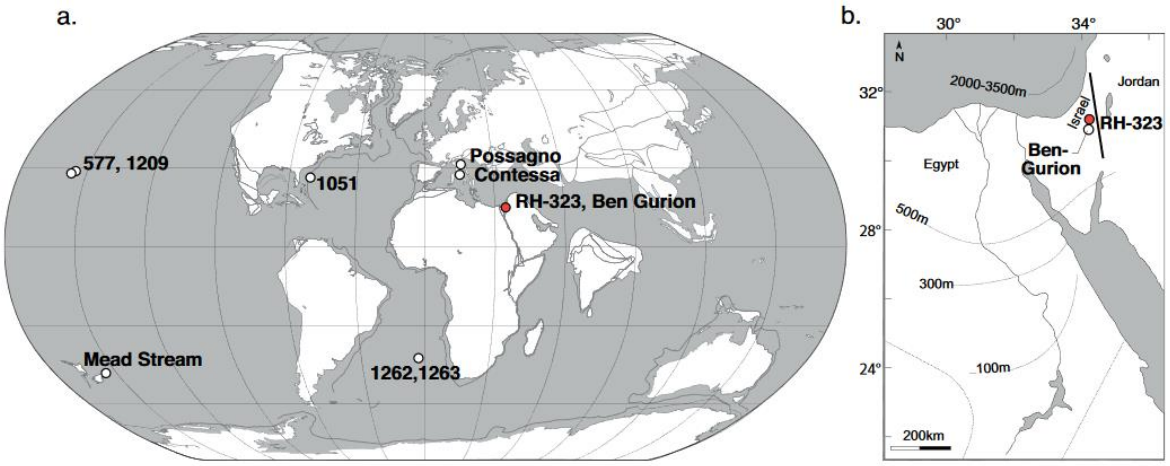

Figure 2. Map showing paleolocation (a) and present-day location (b) of the RH-323 core drillsite at 56 Ma (red dot). Other locations mentioned in Fokkema et al. (2022) are also visualised (white dots). Adapted from Fokkema et al. (2022).

Present-day Negev is characterised by a hot desert climate with little precipitation. It is located around 31 °N, while its early Eocene paleogeographical position was around 15 – 20 °N (www.paleolatitude.org version 3.beta.3; Van Hinsbergen et al., 2015). The RH-323 core provides an opportunity to study (sub)tropical temperature development during the early middle Eocene transition at high resolution. This could offer insights into the timing and extent of the potential post-EECO cooling and the occurrence of CIE-associated hyperthermals on an orbital scale. While there is another tropical early Eocene SST record (ODP 959; Cramwinckel et al., 2018; Fokkema et al., 2023), its data resolution for the EECO to post-EECO interval (~52 – 47 Ma) is insufficient for detailed analysis of the recorded cooling and late EECO hyperthermals. Moreover, hyperthermals have been recorded in the earlier part of core RH-323 (~57 – 52 Ma) (Fokkema et al., 2024; Chapter 6). Therefore, it would be valuable to extend the temperature record across the entirety of the EECO, to explore the possibility of consistently recording hyperthermal events throughout this period on orbital scale. Such an extensive SST record currently does not exist.

According to the DeepMIP simulations, the paleolocation of site RH-323 was located along the margins of the dry (sub)tropical band during the early Eocene (Cramwinckel et al., 2023). However, the DeepMIP simulations are highly inconsistent regarding the zonally averaged mean annual precipitation for the subtropics, and more specifically, for the North African region (Williams et al., 2022). In accordance with the basic presumption that dry climates should be drier with higher global temperatures (Held & Soden, 2006), there is evidence there were drier conditions during the EECO around this location (Fokkema et al., 2022, 2024; Chapter 6). It is therefore interesting to study if the region became wetter following the onset of presumed global Eocene cooling, as this would be in line with a 'dry-gets-wetter' principle in the case of global cooling (Held & Soden, 2006). Furthermore, the paleolocation of the site seems to be in the margins of the North African monsoon precipitation area (Huber & Goldner, 2012). With the latitudinal extent of this precipitation area being orbitally forced (Bosmans, Drijfhout, Tuenter, Hilgen, & Lourens, 2015), it is likely that the site was either located within or outside of the monsoon precipitation area depending on Earth's orbital configurations. Therefore, the core is suitable for studying the effect of orbital forcing on the southern Tethys region hydroclimate variability, as a likely representation of past monsoon dynamics.

Building on previous work (Fokkema et al., 2022, 2024; Chapter 6, Mannucci et al., in prep), samples corresponding to roughly 52 – 47 Ma, ~250 – 130 meters below land surface (mbs), will be taken to produce various types of proxy data. Bulk carbonate stable carbon and oxygen isotope data will be used for stratigraphic purposes and to study general climatic trends (e.g. Fokkema et al., 2022; Westerhold et al., 2018). Using the bulk carbonate $\delta^{13}C$ record, CIE peaks will be chemostratigraphically correlated with the benthic foraminiferal stable carbon isotope compilation of Westerhold et al. (2017, 2018), to extend the age model for RH-323. Bulk sediment magnetic susceptibility (MS) data will be generated to study changes in river discharge and/or dust input of clay minerals (cf. Larrasoaña et al., 2008). Moreover, specific organic biomarkers will be analysed. These include thaumarcheotal membrane lipids, which consist of the isoprenoid GDGT lipids (isoGDGTs). The distributions of these lipids are used for TEX_{86} inferred SST reconstructions (Schouten et al., 2002).

In addition to this, branched GDGTs (brGDGTs) that are produced by bacteria will be used to assess the relative contribution of fluvially-discharged, terrestrially sourced GDGTs (Hopmans et al., 2004; Sinninghe Damsté, 2016; Xiao et al., 2020). Furthermore, distributions of plant leaf wax n-alkanes will be used as an aridity proxy. Plants accustomed to arid climates, like grasses, are assumed to produce relatively more leaf wax n-alkanes with longer aliphatic chains (i.e. C_{33} and C_{35}) than plants accustomed to less arid climates (Bliedtner et al., 2018; Bush & McInerney, 2013; Carr et al., 2014). Therefore, the average chain length of the n-alkanes (ACL), can be used as a proxy for aridity in the hinterland of the site. Plant leaf wax n-alkanes are deposited in oceans and sediments through river discharge and dust deposition (Castañeda et al., 2016; Hemingway et al., 2016; Schreuder et al., 2018; Yedema et al., 2023). Lastly, spectral analyses will be done on the MS, $\delta^{18}O$ and n-alkane records to investigate orbital forcing of the hydroclimate in the southern Tethys region.

With these proxies combined the aim of this study is to characterise climate variability in this region during the early middle Eocene transition period, summarised as follows:

1. Establishing a high resolution stratigraphy of the period of ~52 – 47 Ma, in Northern Negev, Israel (Southern Tethys), using bulk carbonate stable oxygen and carbon isotope ratios.
2. Comparing the climatic conditions between the end of the EECO and the early middle Eocene, for this location. Reconstructed sea surface temperatures will be compared to published records to evaluate if the early - middle Eocene cooling recorded at higher latitudes is a global phenomenon, and to see if the hyperthermals as found for the earlier part of the core (~56 – 52 Ma) (Fokkema et al., 2024; Chapter 6) are a consistent feature of the EECO in the southern Tethys region.

3. Characterise hydrological change in the southern Tethys region during the early middle Eocene transition, using proxies for the supply of terrestrial materials to the basin (BIT index, MS) and hydrological regime on land (plant leaf wax n-alkanes).
4. Investigating the influence of a potential early monsoon system on the hydroclimate through spectral analysis.

3. Methods and materials

3.1. Materials

Core RH-323 (31.143°N, 34.798°E) was retrieved as part of a hydrogeological survey in Revivim Valley southern Israel (Adar et al. 1999). The core is stored at the University of Haifa in 77 boxes of about 3 meters, numbered 1 to 77. The core covers approximately 350 m of upper Paleocene to middle Eocene sediments. These sediments consist of marls, chalks and cherts, corresponding to several regional lithostratigraphical units. For a full lithological description of RH-323 in the regional context, describing long term changes and superimposed variation, see Fokkema et al. (2022, 2024; Chapter 6) and references therein.

Guided by biostratigraphic tie-points, Fokkema et al. (2022) chemostratigraphically correlated the bulk stable carbon isotope record (n=116) covering the interval ~93 – 350 meters below surface (mbs), to the astronomically tuned benthic foraminiferal isotope compilation of Westerhold et al. (2020), to develop a first age-depth model of the core (Fig. 3). The core's age interval was determined to be around 45 – 59 Ma (Fokkema et al., 2022). Follow-up high resolution cyclostratigraphic work by Mannucci et al. (in prep) led to an orbital stratigraphy from a core depth of 306.5 to 247.6 mbs, corresponding to ~55.6 – 51.4 Ma (Fig. 3).

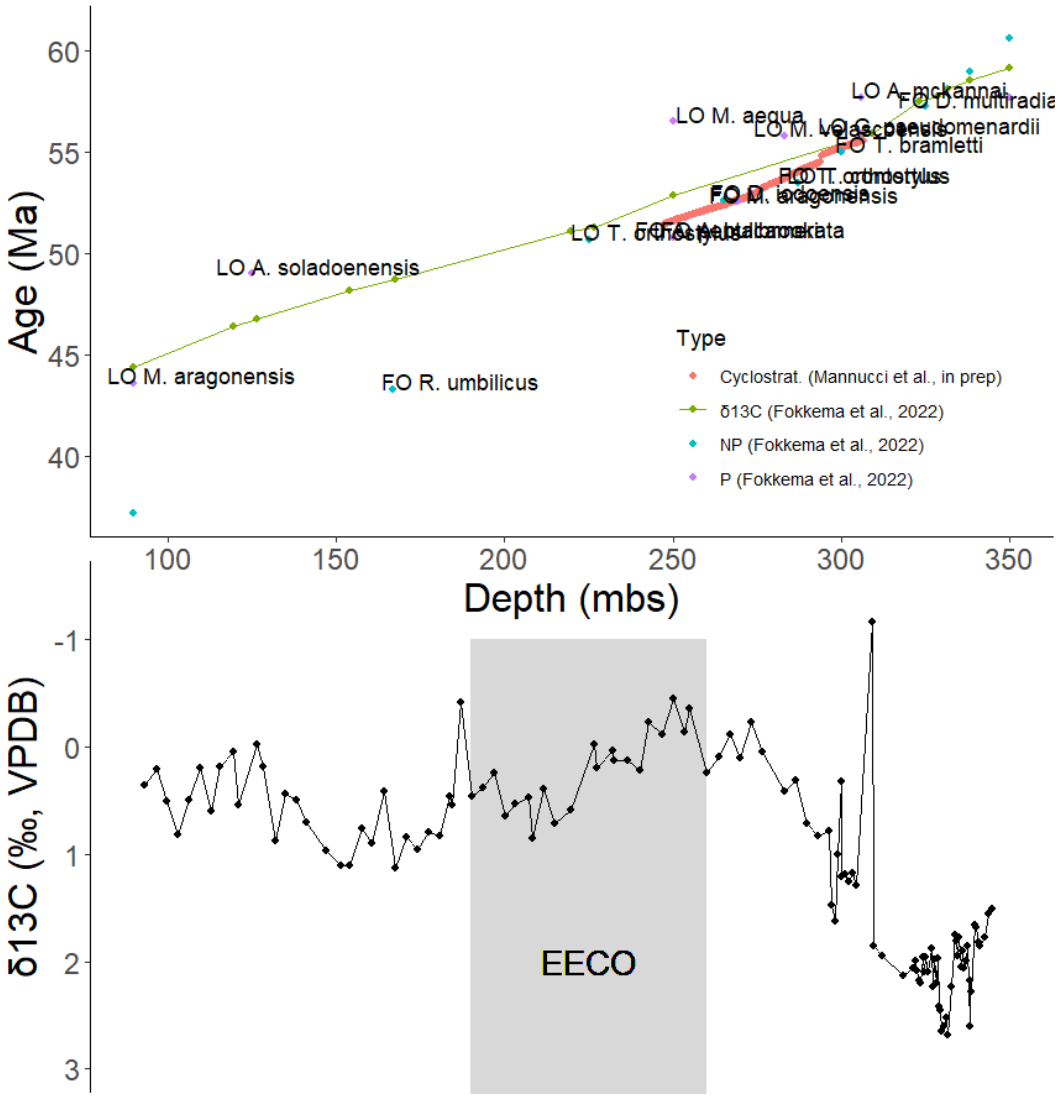

Figure 3. Top: The age-depth model based on $\delta^{13}C$ chemostratigraphic correlation (green; Fokkema et al., 2022), bio-stratigraphic tie-points based on first and last occurrence (FO and LO, resp.) of calcareous nannofossils (NP; blue) and planktonic foraminifera (P; purple) (Fokkema et al., 2022), and cyclostratigraphic tuning (orange; Mannucci et al., in prep). Bottom: the bulk $\delta^{13}C$ record of Fokkema et al. (2022), with grey shaded area representing the EECO (~53 – 50 Ma).

Guided by these stratigraphic constraints, a total of 635 samples of ~25 g were taken from the interval 247.5 – 118.3 mbs using a hammer and chisel, in August 2023. From boxes 46 – 49, 103 samples were taken with ~10 cm resolution. This interval (~247.5 – 236.7 mbs) covers the stable carbon isotope trends found in Fokkema et al. (2022), corresponding to the body of the EECO. From boxes 10 – 45, 532 samples were taken with a ~20 cm resolution. This interval (~235.2 – 118.3 mbs) covers the presumed end-EECO to middle Eocene transition. According to the average sedimentation rate of the first age-depth model (~1.50 cm/kyr; Fig. 3), a sampling resolution of 20 cm results in a resolution of ~14 kyr/sample, which would allow for the detection of obliquity cycles (~41 kyr) in the record, if present. The 10 cm resolution for the 247.5 – 236.7 mbs interval was chosen to be able to study the majority of the early Eocene (~PETM to EECO; ~56 – 50 Ma) in the resolution of precession (~20 kyr), in combination with the data from Fokkema et al. (2022, 2024; Chapter 6).

The depth below surface of all sedimentary material was assumed to be measured from the top of each box. If gaps in the material were present, the material was moved to the top of the box. Some boxes had large gaps in material (Fig. 4), for which the pieces of core on each side of the gap did not fit structurally or colour wise. This resulted in potentially inaccurate depth measurements, which also potentially affected the age-depth calibration.

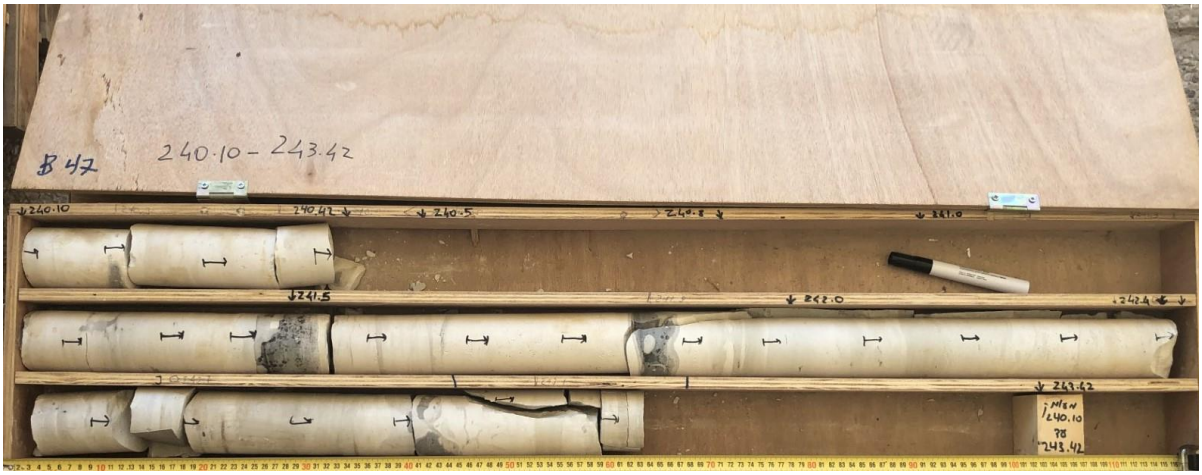

Figure 4. An example a core box (box 47) with gaps in material. In this core box all material is shifted to the top.

This study focuses specifically on the depth interval of 129 – 275 mbs, which spans the EECO to early middle Eocene transition. Of this studied interval, all data deeper (older) than 247.03 mbs (51.438 Ma) originates from Fokkema et al. (2024; Chapter 6) or Fokkema et al. (2022).

For the interval of 247.04 to 129 mbs, a total of 330 samples were analysed for magnetic susceptibility, 333 for bulk stable isotope analyses, and 219 samples for biomarker analyses, in this study.

3.2. Bulk magnetic susceptibility

Samples were freeze-dried and scraped clean for preparation. Subsamples of about 30 cm^3 were crushed to ~2 cm sized pieces by mortar and pestle. Mass-specific bulk magnetic susceptibility (MS) measurements were done on Multi-Function Kappabridge (MFK1-FA), with values reported in χ. Positive χ values indicate an overall paramagnetic property of the bulk sample (e.g. due to phyllosilicates and iron containing feldspars), whereas negative χ values indicate overall bulk diamagnetism (e.g. due to quartz and calcite) (Parés, 2015). The analytical precision of the MS measurements was determined by calculating the standard deviation of repeated measurements of all samples (n=2 or n=3). The mean

standard deviation was $7.7x10^{-11}$±$1.05x10^{-11}$ (95% CI) (Fig. S1). This means that the MS signal is most likely (>95% probability) a true signal when the MS variability has a magnitude larger than 8.75e-11.

3.3. Bulk carbonate stable isotope analysis

For stable carbon and oxygen isotope measurements of bulk carbonate, a powdered subsample of each sample was weighed (between 55 and 206 μg) and analysed on a Thermo Finnigan GasBench II system coupled to a Thermo Delta-V mass spectrometer over 7 runs. Results were calibrated using standard bracketing against an in-house carbonate standard NAXOS and the international atomic energy agency carbonate standard IAEA-603. Measurements were corrected for temporal drift through a linear regression of the standard measurements over time. Measurements with a *m/z* 44 peak that was ~2V higher than the highest measured *m/z* 44 peak of the standards were remeasured, as this results in less reliable measurement corrections. All values are reported in standard delta notation relative to the Vienna Pee Dee Belemnite (VPDB). The analytical precision of the bulk stable isotope measurements was determined by calculating the standard deviations of repeated (n=4 to 11, see supplementary material) NAXOS measurements of the 7 runs done for this study. For $\delta^{18}O$, the mean NAXOS standard deviation was 0.057±0.020‰ (95% CI), with a maximum of 0.105‰, and for $\delta^{13}C$ this was 0.067±0.017‰ (95% CI), with a maximum of 0.094‰ (Fig. S2). This means the $\delta^{18}O$ and $\delta^{13}C$ signals are most likely (>95% probability) true signals if the magnitude of variability exceeds 0.077 and 0.084‰ respectively.

Bulk $\delta^{18}O$ based SST reconstructions (see section 3.5.5 and 5.3.2) were based on the following equation (Reghellin et al., 2015):

$$SST = 16.1 - 4.64((\delta^{18}O_{bulk} - 1) - \delta^{18}O_w) + 0.09((\delta^{18}O_{bulk} - 1) - \delta^{18}O_w)^2 \quad \text{(Equation 1)}$$

The seawater $\delta^{18}O$ value ($\delta^{18}O_w$) is assumed to be -0.15, based on the polynomial regression of the modern-day latitudinal $\delta^{18}O_w$ gradient, and the assumption of an ice-free world (Zachos et al., 1994).

3.3.1. $CaCO_3$ content estimations

$CaCO_3$ weight percentages were estimated using the mass-spectrometer *m/z* 44 peak intensity of the samples, which reflects the amount of [$CaCO_3$] in each sample. It is assumed that non-$CaCO_3$ components in the sediment result in a *m/z* 44 peak intensity of 0 mV, and that the in-house carbonate standards consist 100% of $CaCO_3$. Of the 7 runs a regression was done of the standard weights as a function of *m/z* 44 peak intensity. This regression was applied to the *m/z* 44 peak intensity values of each sample of that run, divided by weight, to calculate $CaCO_3$ weight percentages:

$$[CaCO3](wt\%) = \frac{a*(m/z\ 44\ intensity)+b}{mass} * 100\%$$

To be conservative, the precision of this method is determined by calculating the standard deviation of the estimated [$CaCO_3$] applied to the standard measurements of all runs combined, which was 19%. This is relatively high (cf. Fokkema et al., 2022), and is likely the result of the inaccurate weighing of samples using the Sartorius Cubis® II Lab Balance, which has a programmed drift correction applied to each weight measurement. Through this low precision, interpretation of the [$CaCO_3$] record should be done with caution.

3.4. Chemo- and cyclostratigraphy

Further chemo- and cyclostratigraphic work was done to extend the first age-depth model (Fig. 3) in orbital resolution, to a depth of 129 mbs.

3.4.1 Chemostratigraphy

Using the bulk carbonate $\delta^{13}C$ record (247.03 – 129.1 mbs), negative carbon isotopic excursion (CIE) peaks were stratigraphically correlated with CIE peaks of the benthic foraminiferal stable carbon isotope compilation of Westerhold et al. (2017).

3.4.2 Cyclostratigraphy

In addition to this, the short eccentricity cycles (~100 kyr) were identified and filtered from the bulk $\delta^{13}C$ and MS record, using spectral analysis (multi-taper method) and Gaussian bandpass filtering, through the Acycle (version 2.8) application (Li et al., 2019). Westerhold et al. (2017) have shown the negative benthic deep sea CIEs to correspond well with eccentricity maxima, of the Laskar2010b astronomical solution (Laskar et al., 2011) . This is due to short term global carbon cycle changes, as reflected by deep sea benthic $\delta^{13}C$ records, to be substantially eccentricity forced (Anagnostou et al., 2020; Zeebe et al., 2017). This relationship allows for the short eccentricity filters to serve as a reference for chemostratigraphic correlation.

For the identification of the Gaussian bandpass filter frequencies corresponding to the various orbital parameters, the ratios between the various peaks in the spectral analysis were taken as a reference, knowing the long eccentricity : short eccentricity : obliquity : precession ratios are ~405:100:41:24 (see supplementary material; fig S7). The bulk $\delta^{13}C$ data was prepared for spectral analysis by sorting, deletion of empty values, interpolation for equal sample rate, and by detrending through subtracting residuals from a fitted *locally weighted scatterplot smoothing* (LOWESS) line, using the Acycle (version 2.8) application (Li et al., 2019). Detrending was also done for the bulk $\delta^{18}O$ record, as this allowed for correlation testing of short term variability between the $\delta^{13}C$ and $\delta^{18}O$ records. Spectral analyses done on other records (see discussion) followed the same data preparation steps (i.e. sorting, deletion, interpolation, and detrending).

The sedimentation rate throughout the studied interval was determined by differentiating the *locally estimated scatterplot smoothing* (LOESS) line of the age-depth model throughout the studied interval (see supplementary material, Fig. S8).

3.5. Lipid biomarkers

Lipid biomarkers were extracted from ~6 – 8 g of freeze-dried and homogenized sediment with 25 ml dichloromethane (DCM):methanol (MeOH) (9:1 by volume:volume) using a Milestone Ethos X Microwave Extraction System, set to 70 °C for 50 minutes. The obtained total lipid extracts (TLEs) were passed over a $NaSO_4$ column using DCM:MeOH 9:1 and subsequently dried under a gentle N_2 stream. A known amount of a syntehetic C_{46} GTGT standard was added to the TLEs prior to separation into apolar, neutral and polar fractions using AlOx column chromatography, with hexane:DCM (9:1), hexane:DCM (1:1) and DCM:MeOH (1:1), respectively as eluents. Fractions were again dried under N_2 and weighed.

3.5.1. GDGT analysis

The polar fractions, containing the GDGTs, were diluted in hexane:isopropanol (99:1) to a concentration of 2 mg/ml, and pressed through a 0.45 μm polytetrafluoroethylene filter into a 1 ml glass vial. Per sample, 10μl of filtered polar fraction was analysed by an Agilent 1290 infinity ultra high-performance liquid chromatography (UHPLC) coupled to an Agilent 6135 single quadrupole mass spectrometer with settings according to Hopmans et al. (2016). A signal-to-noise ratio of three times background noise and a peak area>3000 was maintained as detection limit. One sample was excluded due to the absence of any peak, presumably due to a misinjection.

Analytical precision was estimated by analysis of a systematically injected in-house GDGT standard, which resulted in a SD of 0.007 TEX_{86} units, corresponding to a temperature uncertainty between 0.22 and 0.27 ºC (using the TEX_{86} calibration of Kim et al. (2010) (Eq. 3)) and between 0.13 and 0.16 ºC (using the subSST calibration by Ho and Laepple (2016) (Eq. 4)) in the TEX_{86} range of the studied interval. This error represents the instrumental error of temperature variability estimates, so any recorded variability with larger magnitude implies a significant climatological signal. The SDs of BIT index, IR, and $\#Rings_{tetra}$ were 0.02, 0.005 and 0.016 respectively, based on brGDGTs in the same in-house standard.

3.5.2. Alkane analysis

The apolar fractions containing n-alkanes were diluted in hexane in a 1 ml glass vial with insert. Per sample 1 µl of diluted apolar fraction was analysed by an HP 6890 Series Gas Chromatography (GC) System. Two samples were analysed on an Agilent 7890B GC coupled to an Agilent 5977B mass spectrometer to identify the different n-alkanes. To target higher plant-derived compounds, C_{25} – C_{35} n-alkanes were integrated. Only samples with a clear odd (i.e. C_{25}, C_{27}, C_{29}, C_{33} and C_{35}) over even (i.e. C_{26}, C_{28}, C_{30}, C_{32}, C_{34}) n-alkane distribution, indicative of well-preserved higher-plant compounds, were analysed. A total of 147 apolar fractions were analysed for n-alkanes along the core interval of 247 – 129 mbs, with a general resolution of around 1 sample per 2 meters. Two intervals (~10 m), within and after the EECO section, were chosen to be analysed in higher resolution (~1 sample/0.25 m), as this would presumably allow these intervals to be studied on orbital resolution.

3.5.3. Isoprenoid GDGTs

The isoGDGTs used for the TEX_{86} based temperature reconstructions are membrane lipids produced by Thaumarchaeota inhabiting the water column (Fig. 5). The TEX_{86} proxy is based on the homeoviscous adaptation of the Thaumarchaeota to increasing temperatures, whereby an increasing number of cyclopentane rings is incorporated into the membrane lipids as temperatures increase (Schouten et al., 2002). TEX_{86} (Eq. 2) takes into account GDGT-1, GDGT-2, GDGT-3 and the stereoisomer of crenarchaeol (cren') (Fig. 5). GDGT-0 is excluded from TEX_{86} as it is also produced by many different archaea that do not produce any of the other cyclopentane containing GDGTs, and accordingly it could potentially distort the temperature signal (Schouten et al., 2002). Crenarchaeol is excluded from TEX_{86} as it shows a poor correlation with SST, and overpowers the index through its substantially higher abundance than the other GDGTs (Schouten et al., 2002).

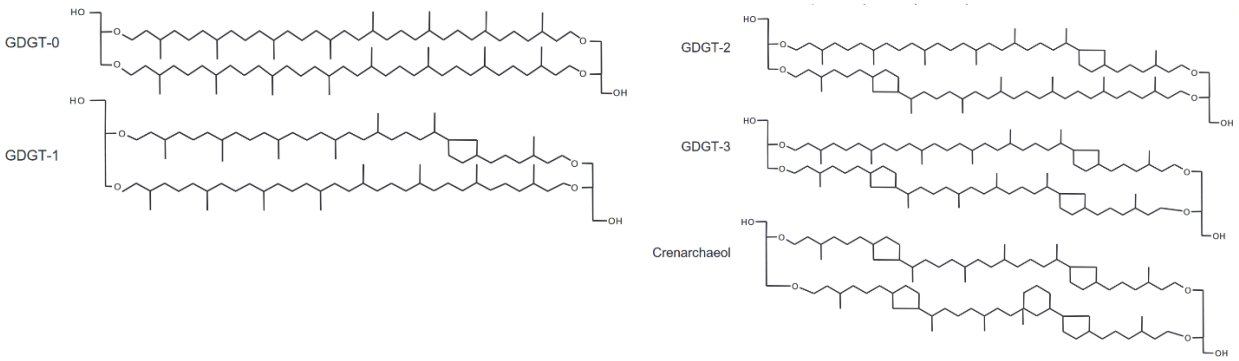

Figure 5. Isoprenoid GDGT Thaumarchaeotal membrane lipids discussed in the text. Crenarchaeol has a stereoisomer (cren'). Adapted from Kim et al. (2010).

$$TEX_{86} = \frac{[GDGT\text{-}2]+[GDGT\text{-}3]+[cren']}{[GDGT\text{-}1]+[GDGT\text{-}2]+[GDGT\text{-}3]+[cren']} \quad \text{(Equation 2)}$$

$$SST = 68.4 * \log(TEX_{86}) + 38.6 \quad \text{(Equation 3)}$$

3.5.3.1. Non-thermal influences

Before applying TEX_{86} paleothermometry, the isoGDGT assemblages were checked for non-thermal influences. For this, the published R code by Bijl et al. (2021) was used. This script assesses the terrestrial isoGDGT contribution through the branched vs. isoprenoid tetraether (BIT) index (Weijers et al., 2006), and contributions of methanotrophic (Methane Index; Y. G. Zhang et al., 2011), methanogenic (%GDGT-0; Blaga et al., 2009), and anaerobic methane oxidising (AOM index; Weijers et al., 2011) archaea. It also determines the relation between TEX_{86} and the weighted number of rings

through the Ring Index (Δ-RI; Y. G. Zhang et al., 2016), indicative of soil and methane impacts, and the contribution of deep residing archaea, using the GDGT-2/GDGT-3 index (Taylor et al., 2013).

3.5.3.2. TEX_{86} calibrations

Various TEX_{86} to temperature calibrations exist, each potentially better representative of the true temperature of the environment the Thaumarchaeota inhabited. Because TEX_{86} is calibrated to modern mean annual ocean temperatures, extrapolation is necessary when reconstructing temperatures beyond that range, as was likely the case in the (sub)tropics during the early Eocene. Linear calibrations are preferred because of their simplicity, however, since the GDGTs of TEX_{86} do not comprise all the various GDGTs present in the membrane lipids of Thaumarchaeota, linear extrapolation could potentially overestimate reconstructed temperatures. In the high TEX_{86} range (TEX_{86} > 0.7) of the various core-top calibrations, the crenarchaeol/GDGT-0 ratio increases non-linearly as compared to TEX_{86} (Cramwinckel et al., 2018). This suggests the homeoviscous adaptation of Thaumarchaeota in this temperature range is increasingly manifested through an increase in the production of crenarchaeol over GDGT-0. This implies TEX_{86} is less sensitive in this extrapolative temperature range, meaning an exponential calibration, such as Kim et al. (2010) devised (Eq. 3), is better suited for extrapolation. This results in more conservative temperature estimates than linear calibrations.

Furthermore, even though TEX_{86} was initially calibrated to SSTs (Schouten et al., 2002), it is thought the ammonia-oxidising Thaumarchaeota most abundantly inhabit the water column at depths between 50 and ~350 m, corresponding to NO_2- maxima (Hurley et al., 2018). Moreover, Thaumarchaeota are also found in deep (>1000 m) waters (Villanueva et al., 2014). This implies the TEX_{86} proxy plausibly reflects temperatures of deeper depths, below the mixed layer. This suggests a calibration to subsurface temperatures would be appropriate.

For this reason, in addition to the exponential SST calibration of Kim et al. (2010) (eq. 2a), a subsurface temperature calibration was used according to the calibration ensemble produced by Ho and Laepple (2016). This ensemble contains TEX_{86} core-top calibrations for which each possible depth range between 50 and 1000 m depth, with 50 m steps, was analysed with least square regression analysis. To confine the integrated source depths of GDGTs from sediment samples, the GDGT-2/GDGT-3 ratio can be used. This ratio is found to correspond with the export depth of GDGTs (Taylor et al., 2013), and increases rapidly beyond a depth of 200 m, in suspended particulate matter (SPM) (Hernández-Sánchez et al., 2014; Hurley et al., 2018; Van Der Weijst et al., 2022). For the early Eocene interval of RH-323, Fokkema et al. (2024) found GDGT-2/GDGT-3 values in a range of 0.3 – 16.3, with a median of 5.0, from which they inferred the TEX_{86} variability to reflect shallow subsurface temperatures (subSST) in a depth range of 100 – 250 m. For this reason the subSST calibration of the Ho and Laepple (2016) ensemble was chosen based on this depth range (Eq. 4). It is assumed the shallow subSST variability reflects the actual SST variability.

$$\text{subSST (100 - 250 m)} = 45.9 * \log(TEX_{86}) + 25.6 \qquad \text{(Equation 4)}$$

3.5.4. Branched GDGTs

BrGDGTs (Fig. 6) were analysed to study terrestrial input of GDGTs. The BIT index (Eq. 5, adjusted to include 6-methyl brGDGTs) (Hopmans et al., 2004; Sinninghe Damsté, 2016) is a measure of the relative abundance of brGDGTs to that of crenarchaeol, which should reflect terrestrial versus marine sources of GDGTs.

$$\text{BIT} = \frac{[\text{Ia}]+[\text{IIa}]+[\text{IIa'}]+[\text{IIIa}]+[\text{IIIa'}]}{[\text{cren}]+[\text{Ia}]+[\text{IIa}]+[\text{IIa'}]+[\text{IIIa}]+[\text{IIIa'}]} \qquad \text{(Equation 5)}$$

Although brGDGTs were initially assumed to be exclusively produced by soil bacteria (e.g. acidobacteria (Sinninghe Damsté et al., 2018)), and, therefore, a measure of soil organic matter (OM) input (Hopmans et al., 2004), brGDGTs may also be produced *in situ* in the marine realm (e.g. Peterse et al., 2009; Weijers et al., 2014; Zell et al., 2014; Zhu et al., 2011), implying the BIT index alone is

unsuitable to trace soil OM input. For this reason the #Rings$_{tetra}$ (Eq. 6) and isomer ratio (IR) (De Jonge, Hopmans, et al., 2014; Sinninghe Damsté, 2016) (Eq. 7) indices are also calculated.

$$\#\text{RingsTetra} = \frac{[\text{Ib}]+2*[\text{Ic}]}{[\text{Ia}]+[\text{Ib}]+[\text{Ic}]} \quad \text{(Equation 6)}$$

$$\text{IR} = \frac{[\text{IIa'}]+[\text{IIb'}]+[\text{IIc'}]+[\text{IIIa'}]}{[\text{IIa'}]+[\text{IIb'}]+[\text{IIc'}]+[\text{IIIa'}]+[\text{IIa}]+[\text{IIb}]+[\text{IIc}]+[\text{IIIa}]} \quad \text{(Equation 7)}$$

The #Rings$_{tetra}$ index represents the number of rings of tetramethylated brGDGTs (Fig. 6), and correlates to the relative contribution of marine *in situ* production to the pool of brGDGTs in the sediment (Sinninghe Damsté, 2016). Values below ~0.3 represent a predominant soil-origin and values above 0.7 represent dominant marine production, as global soils do not reach values above 0.7 (Sinninghe Damsté, 2016). The major environmental control on cyclisation in brGDGTs is pH; the number of rings of the tetramethylated branched GDGTs are hypothesised to increase with marine production due to the relatively alkaline marine conditions as compared to soils (Dearing Crampton-Flood et al., 2021; Sinninghe Damsté, 2016). The IR represents the relative proportion of 6-methyl brGDGTs over the total sum of brGDGTs. Under the influence of pH (De Jonge, Hopmans, et al., 2014; Sinninghe Damsté, 2016), high relative abundances of 6-methyl brGDGTs can be a characteristic of river *in situ* production of brGDGTs (De Jonge, Stadnitskaia, et al., 2014; Guo et al., 2020), and therefore IR is used to identify river *in situ* production of brGDGTs.

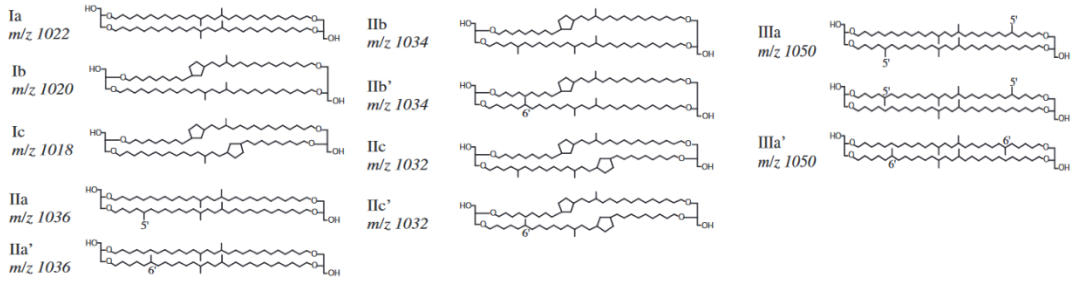

Figure 6. Branched GDGTs referred to in the text. Roman numerals refer to respectively tetra-, penta- and hexa-methylated brGDGTs. Latin letters refer to the absence of (a), or containing a single (b) or two (c) cyclopentane moieties. The apostrophe (‘) refers to 6-methyl isomers.

3.5.5. Average chain length of n-alkanes and nMDS

To assess the n-alkanes in relation to aridity of the hinterland, the n-alkane average chain length of odd C_{25} to C_{35} is calculated (ACL) (Eq. 8).

$$\text{ACL} = \frac{25*[\text{C25}]+27*[\text{C27}]+29*[\text{C29}]+31*[\text{C31}]+33*[\text{C33}]+35*[\text{C35}]}{[\text{C25}]+[\text{C27}]+[\text{C29}]+[\text{C31}]+[\text{C33}]+[\text{C35}]} \quad \text{(Equation 8)}$$

Which n-alkanes actually correspond to woody/non-woody vegetation (i.e. humid/arid) in a specific environment is determined by site-specific adaptational and environmental factors. The ratio of C_{31} and C_{33} over C_{27}, C_{29}, C_{31} and C_{33}, for example, corresponds better to aridity in modern vegetation and soils in the Caucasus region, than ACL (Bliedtner et al., 2018). Carr et al. (2014) found the ratio of C_{31} over C_{29} and C_{31}, to correspond better to aridity in the semi-arid/arid regions of South Africa, than ACL. For this reason a non-metric multidimensional scaling (nMDS) ordination analysis based on a Bray-Curtis dissimilarity matrix of the alkane distributions is done, using *metaMDS()* and *envfit()* of the *vegan* package in R. In this nMDS, SST reconstructions based on the bulk $\delta^{18}O$ values of the samples are used as a colour coding of the samples, as not all n-alkane samples had corresponding TEX_{86} measurements. This allows for the development of a specific ratio that most effectively incorporates the contrast between n-alkane distributions of samples, based on temperature, for this specific core.

For the nMDS the alkane distributions were normalised by dividing each alkane peak area by the sum of alkane peak areas of each sample, due to the lack of using a GC standard for quantification.

4. Results

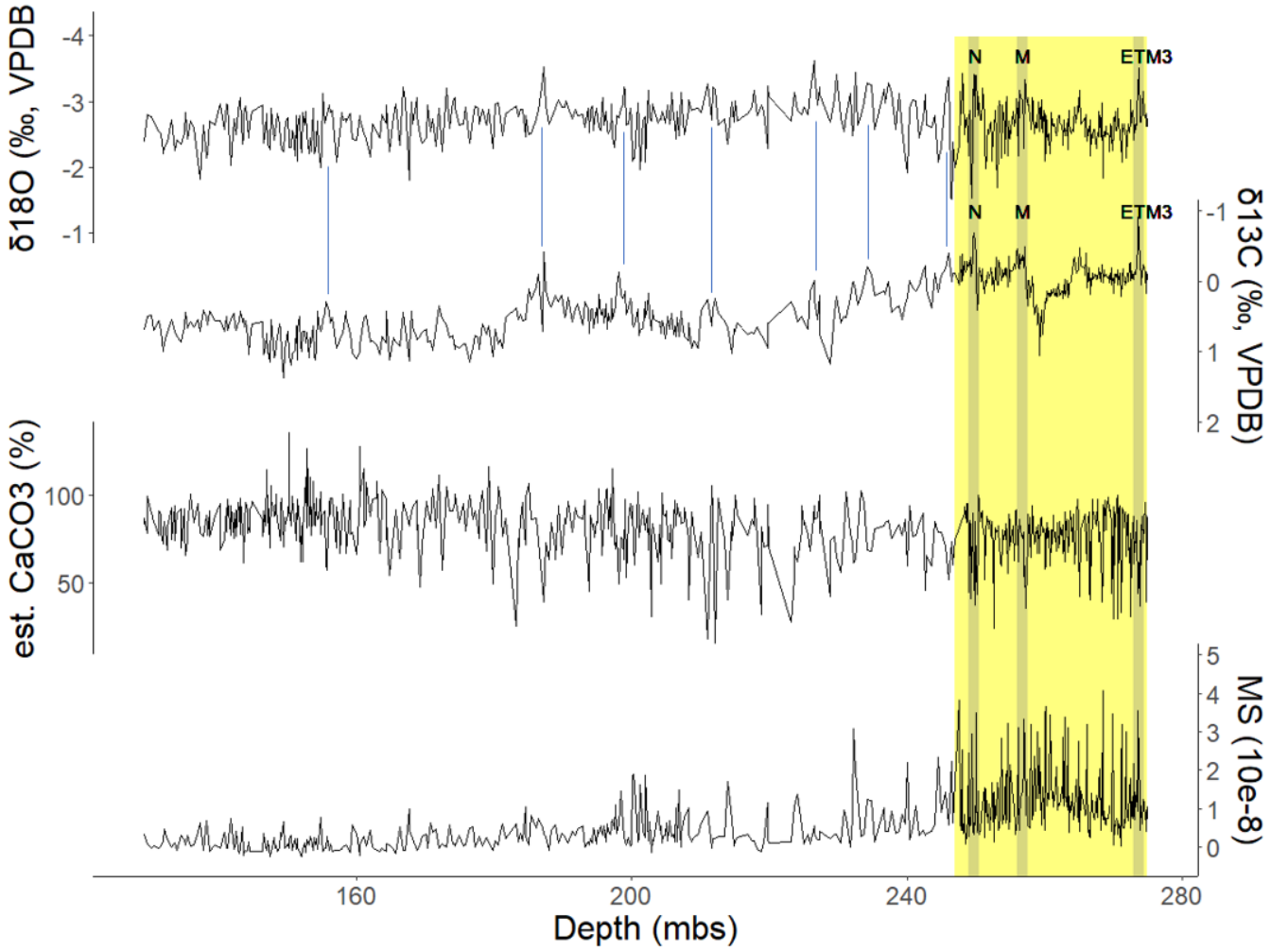

Figure 7. Bulk stable oxygen (top), carbon (top-middle) isotope, est. [$CaCO_3$] (bottom-middle), and magnetic susceptibility (bottom) results. Grey bands represent hyperthermals identified by Mannucci et al. (in prep). Y axes are reversed for the bulk stable isotope records. Data from 275 to 247.03 mbs (orange shaded area) is presented in Mannucci et al. (in prep). The blue lines represent examples of corresponding peaks between the bulk stable carbon and oxygen record.

4.1. Bulk magnetic susceptibility

The bulk MS record shows a gradual decrease throughout the studied interval (Fig. 7), and also throughout the whole core (cf. Fokkema et al., 2024; Chapter 6, Mannucci et al., in prep). For the section of 247.03 – 129 mbs, the MS ranges between -0.26 x 10^{-8} and 3.8 x 10^{-8}, with a median of 0.26 x 10^{-8}. The values of this interval are on average 3-fold lower than the MS values of the section between the ETM3 and N (~275 – 250 mbs) (Fig. 7; Fokkema et al., 2024; Chapter 6, Mannucci et al., in prep), and 12-fold lower than the section between the PETM and ETM3 (~310 – 275 mbs) (not shown; Fokkema et al., 2024; Chapter 6, Mannucci et al., in prep). The amplitude of variability also decreases throughout the studied interval.

4.2. Estimated $CaCO_3$ content

The bulk estimated [$CaCO_3$] shows a gradual increase throughout the studied interval (Fig. 7), from ~70 to 80 wt%. This is generally higher than the [$CaCO_3$] estimations for the PETM – ETM3 section of Fokkema et al. (2024), which were around ~50%. The amplitude of shorter term variability seems to decrease throughout the core. However, as mentioned in section 3.3.1, the [$CaCO_3$] estimates should be interpreted with caution, as the analytical precision of the estimates is relatively low.

4.3. Bulk carbonate oxygen and carbon isotopes

Between 247.03 and 187 mbs, the bulk oxygen and carbon isotope records show an opposite long term trend: $\delta^{18}O$ first decreases from ~-2.3 to 3 ‰, and then around 225 mbs increases again, whereas the $\delta^{13}C$ record shows an increase from ~0 to 1 ‰, and then around 225 mbs a decrease back to ~0.2 ‰ (Fig. 7).

Around 187 mbs, there is a systematic increase in the $\delta^{13}C$ and $\delta^{18}O$ records. The carbon isotope record shows a step-wise increase from ~0.2 to 1 ‰, and the oxygen isotope record shows a gradual increase, from ~-3 to -2.5 ‰, from 187 to 129 mbs. Overall the values are in the range of the post-PETM section of Fokkema et al. (2024), i.e. ~0 to 1 ‰ for $\delta^{13}C$, and ~-3 to -2 ‰ for $\delta^{18}O$.

On shorter time scales many peaks between the $\delta^{18}O$ and $\delta^{13}C$ records align, of which some examples are given with the blue lines in Figure 7. This short term correspondence is further represented by significant ($p<0.005$) linear regressions between the detrended (i.e. long term trends removed) $\delta^{18}O$ and $\delta^{13}C$ records for different depth ranges (Fig. 8).

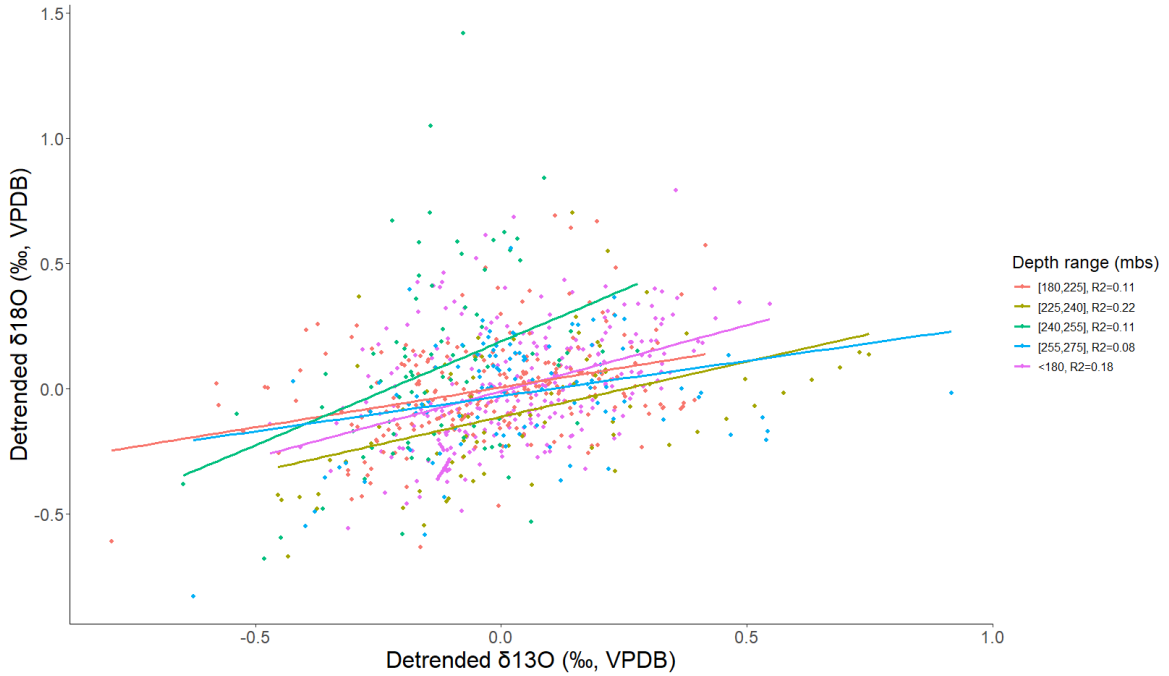

Figure 8. Detrended bulk $\delta^{18}O$ versus $\delta^{13}C$ values for various depth ranges. The lines represent the linear regressions for each depth range, with corresponding R^2 shown on the right. All regressions have $p<0.005$.

4.4. Isoprenoid GDGTs

The GDGT-2/GDGT-3 values for the studied interval (247.03 – 129 mbs) are around 5.03 ± 0.04 (95% CI) (Fig. 9). These values are on average similar to the earlier part of the core between the PETM and hyperthermal N (~309 – 250 mbs) (Fokkema et al., 2024), however the range of values is smaller (3.6 – 8.2, versus, 0.3 – 16.3). In modern oceans, GDGT-2/GDGT-3 ratios quickly increase between the shallow subsurface (50 – 200 m) and the deeper water column (Hurley et al., 2018; Van Der Weijst et al., 2022). Therefore, even small contributions of archaea inhabiting deeper waters can affect the GDGT-2/GDGT-3 ratio substantially, even though they do not result in large changes in TEX_{86} (Varma et al., 2023). For this reason, no datapoints were removed from the TEX_{86} record based on their GDGT-2/GDGT-3 value, as no sample was indicative of a truly deep water signal. These things considered, it is inferred that the peak integrated GDGT source is between 100 and 250 m for the studied interval (Van Der Weijst et al., 2022). This is in line with Fokkema et al. (2024; Chapter 6) and validates the use of Eq. 4, for the TEX_{86} subSST calibration.

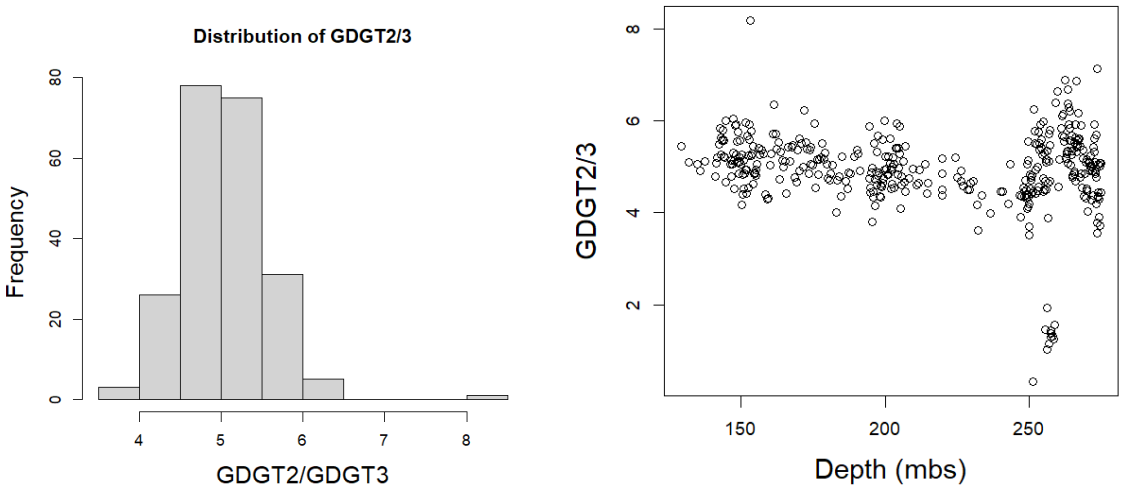

Figure 9. Distribution of the GDGT-2/GDGT-3 values for the studied interval (247.03 – 129 mbs) (left) and scatterplot of the GDGT-2/GDGT-3 values versus depth (275 – 129 mbs) (right). Data from 275 to 247.5 mbs is from Fokkema et al. (2024; Chapter 6).

A single datapoint in the 247.03 – 129 mbs interval was excluded from the TEX_{86} record, based on exceeding the Δ-RI (i.e. Ring Index) criterium of 0.3 (Zhang et al., 2016). The Methane Index (Zhang et al., 2011), AOM index (Weijers et al., 2011), BIT index (Weijers et al., 2006) and %GDGT-0 (Blaga et al., 2009) criteria were not exceeded for the 247.03 – 129 mbs interval.

4.4.1. TEX_{86} paleothermometry

With the outlier excluded, the TEX_{86} values throughout the studied dataset (n = 219) range from 0.79 to 0.93, with a median of 0.87. According to the SST TEX_{86} calibration (Eq. 3), this represents an SST range of 31.4 to 36.4 °C, with a median of 34.4 °C. It represents a subSST (100 – 250 m) range of 20.8 – 24.1 °C, with a median of 22.8 °C (Eq. 4). These values are similar to those of the PETM to EECO interval (~310 – 247.5 mbs) (Fokkema et al, 2024; Chapter 6), but have a smaller spread.

From around 247 to 200 mbs, there is a long term warming trend from ~34 to 35 °C (~22.5 to 23.2 °C subSST). Coinciding with the step-wise increase in $\delta^{13}C$ around 187 mbs is the onset of a long term cooling trend from around 35 to 34 °C (~23.2 to 22.5 °C subSST).

Furthermore, the CIEs in the bulk $\delta^{13}C$ record generally correspond to transient temperature increases of about ~1 – 2 °C SST (~0.7 – 1.3 °C subSST) (Fig. 10). Remarkable is the drop at ~161 mbs, from around 34 to 31.6 °C SST (22.8 to 21.2 °C subSST). This temperature drop is represented by three datapoints that are not analytical outliers.

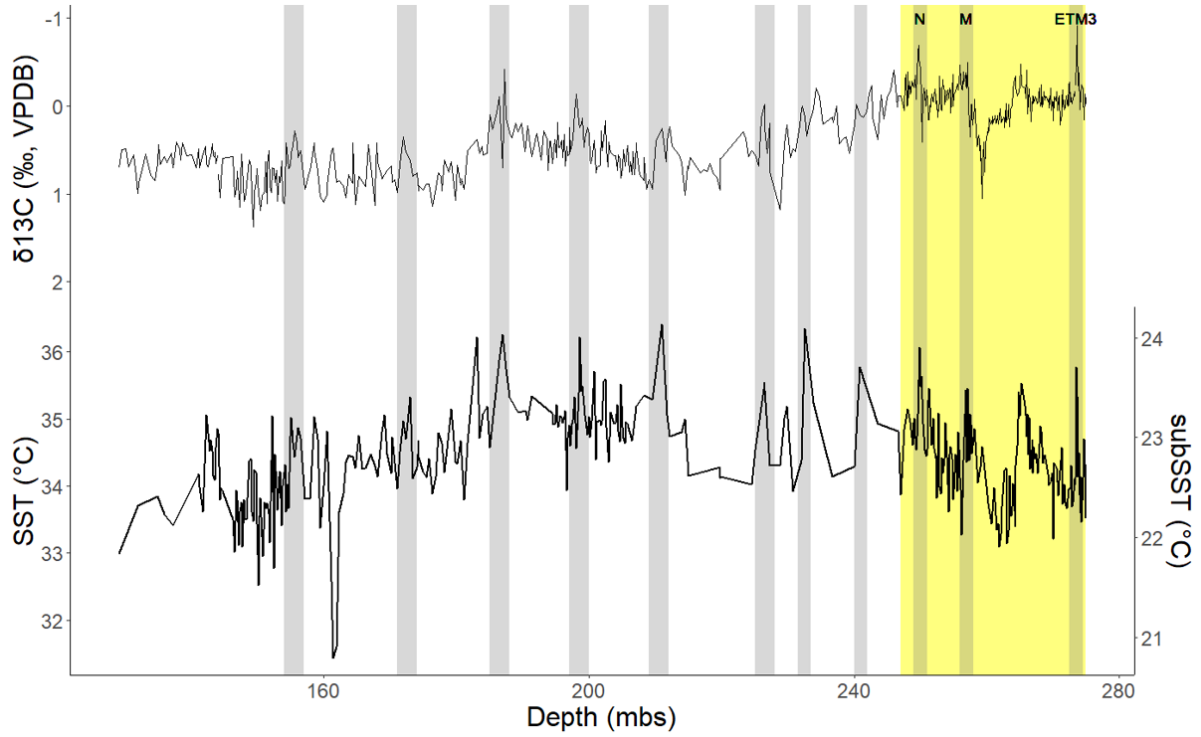

Figure 10. The bulk $\delta^{13}C$ record (top) compared with the TEX_{86} based SST and subSST record (bottom). The grey bars represent examples of CIEs that coincide with temperature peaks. $\delta^{13}C$ and TEX_{86} data from 275 to 247.03 mbs (orange shaded area) is presented in Mannucci et al. (in prep) and Fokkema et al. (2024; Chapter 6), respectively. ETM3, M and N are hyperthermals previously identified by Mannucci et al. (in prep).

4.5. Branched GDGTs

BIT values have a median of 0.027, and a range of 0.002 – 0.19. IR values have a median of 0.55 (range 0.46 – 0.75), and #RingsTetra values have a median of 0.58 (range 0.32 – 0.87) (Fig. 11). Overall, from 247.03 to 129 mbs BIT remains around ~0.027, not exceeding 0.05. From around 190 mbs #RingsTetra gradually start decreasing from ~0.65 to 0.5. IR remains constant around 0.55.

On shorter time scales, the #RingsTetra record varies more than IR and BIT. Two peaks that stand out are the BIT peak to ~0.2 around 243 mbs, and the #RingsTetra drop to ~0.3 around 161 mbs, which coincides with a temperature drop witnessed in the TEX_{86} record (Fig. 10).

Figure 12 depicts the absolute abundances of the total sum of brGDGTs and crenarchaeol. In the long term, the brGDGTs and crenarchaeol abundances increase throughout the studied interval. On shorter time scales, the brGDGTs and crenarchaeol fluctuate coherently, which is confirmed by a cross-correlation (CC) test of the two time series (CC=0.38, $p<0.005$) (testcorr package in R).

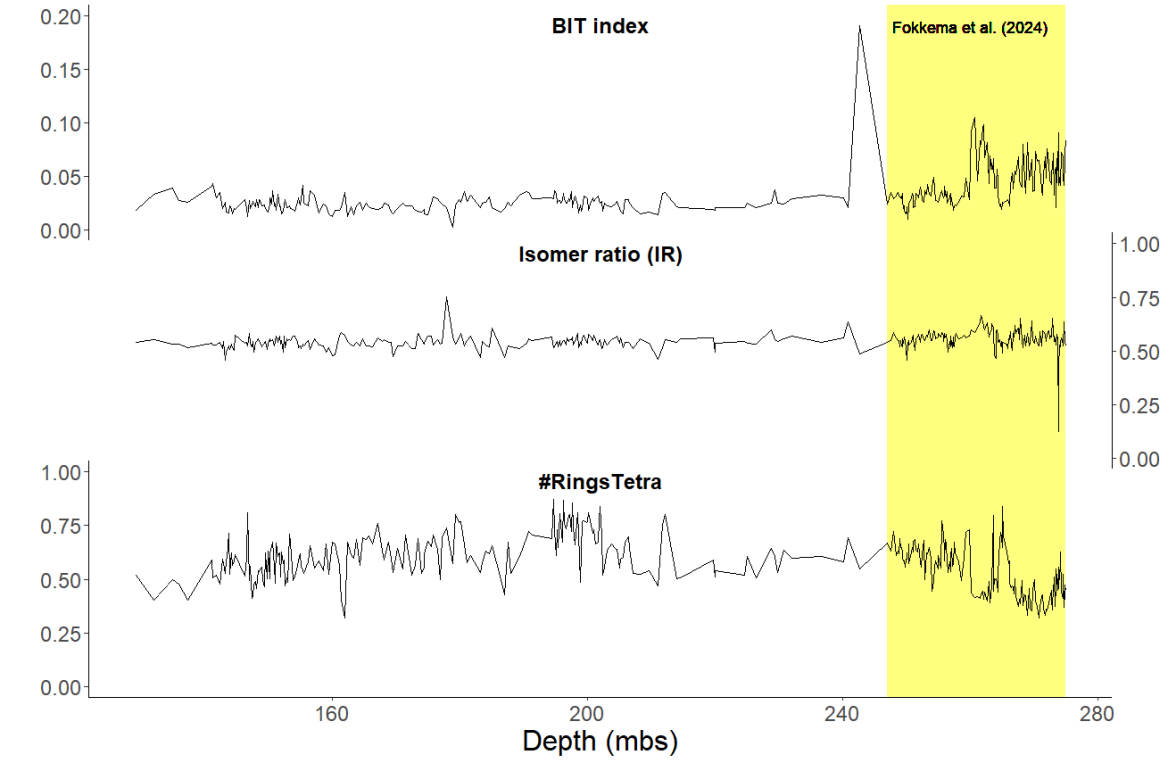

Figure 11. The BIT, IR, and #RingsTetra record. Data from 275 to 247.03 mbs (orange shaded area) is presented in Fokkema et al. (2024; Chapter 6).

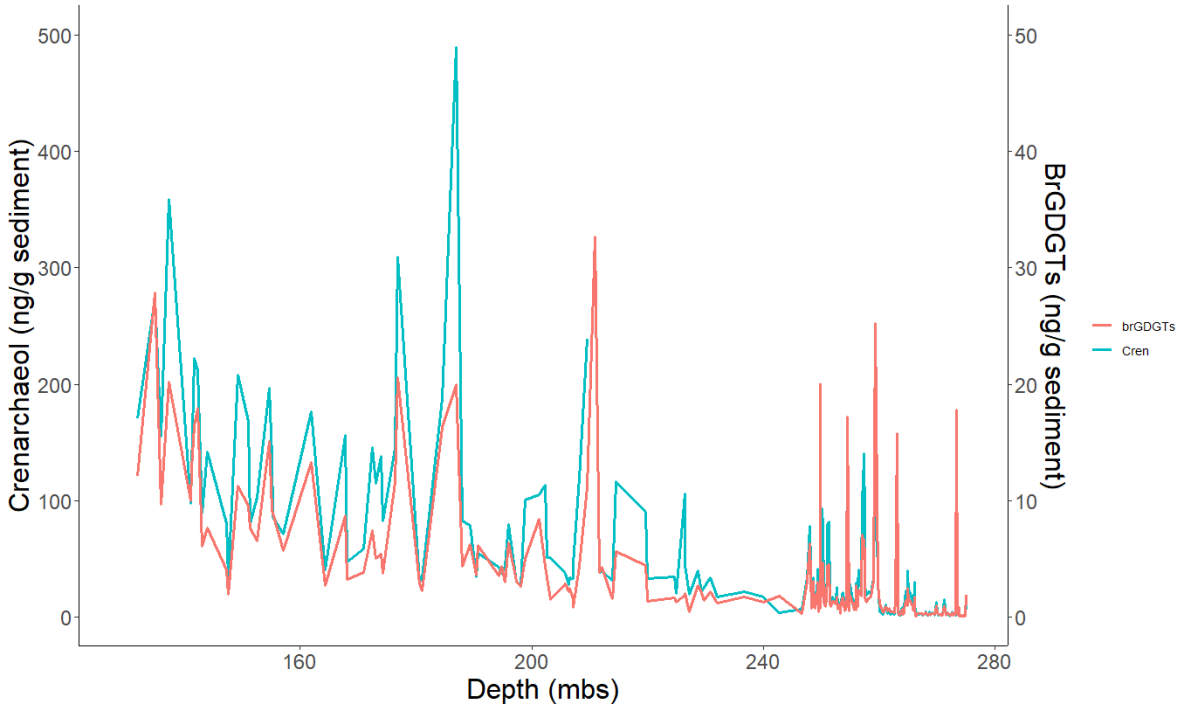

Figure 12. The absolute abundances (in ng/g sediment) of crenarchaeol and brGDGTs. Note the plot is zoomed in for better visualisation of the time series, as around 250 mbs the brGDGT abundance goes to nearly 300 ng/g (not shown), and around 210 mbs crenarchaeol abundance goes to ~1000 ng/g (not shown). Data from 275 to 247.03 mbs is from Fokkema et al. (2024; Chapter 6)

4.6. Plant leaf wax n-alkanes

4.6.1. NMDS

The nMDS shows there is a demarcation between short n-alkanes (i.e. C_{25}, C_{27}, and C_{29}) and long n-alkanes (i.e. C_{31}, C_{33}, C_{35}) along the x-axis of the nMDS plot (i.e. MDS1) (Fig. 13). There is a rough SST gradient in the nMDS plot from the top right to bottom left. It seems the warmer samples correspond to the shorter n-alkanes, however this relation is not statistically significant. The relative proportional abundance of C_{35} and C_{33} in respect to C_{25}, C_{27} and C_{29} (black arrows in Fig. 13) seem to represent this SST gradient best. This relationship will be termed Ratio35 (Eq. 9) and is used in addition to $ACL_{27\text{-}33}$ as a site-specific ratio to study the changes in n-alkane distributions throughout the core.

$$\text{Ratio35} = \frac{C35+C33}{C35+C33+C25+C27+C29} \qquad \text{(Equation 9)}$$

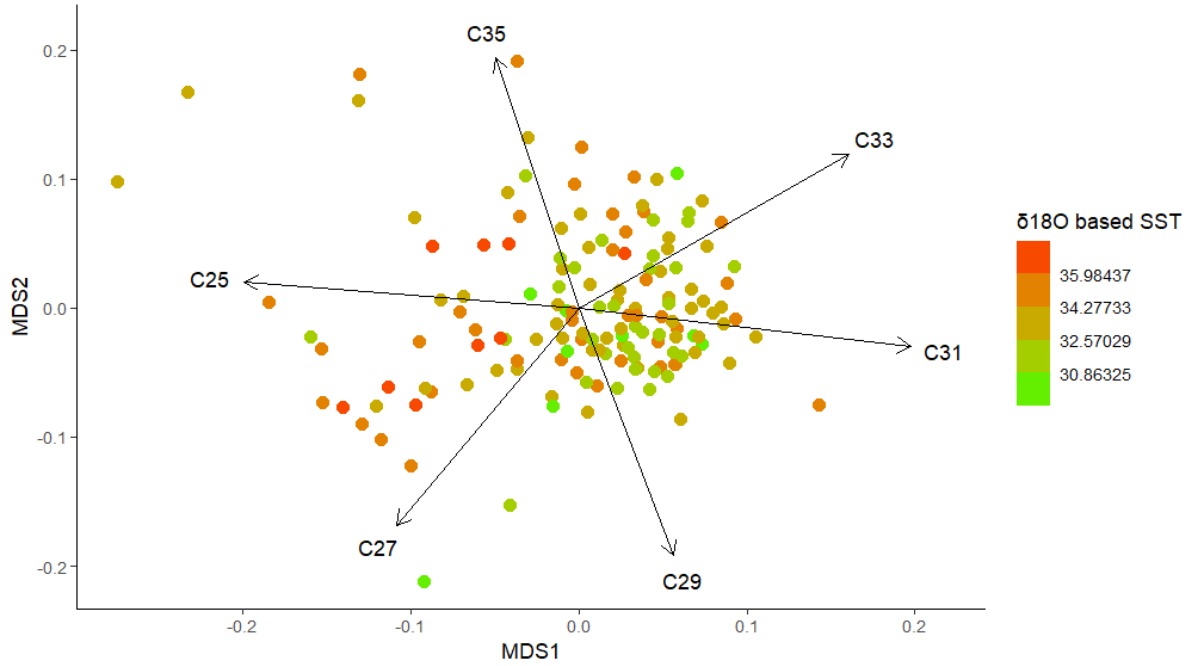

Figure 13. Non-metric multidimensional scaling of the odd n-alkane distributions. Each point represents a sample. Samples are colour coded based on their $\delta^{18}O$ reconstructed SST. Black arrows are gradients representing the direction of greatest change of the relative abundance of the corresponding n-alkane in the distributions.

4.6.2. ACL and Ratio35

ACL and Ratio35 do not show a systematic long term increase or decrease throughout the studied interval (247 – 129 mbs). Both records do show short term fluctuations, in a range of 28.3 – 30.9 (ACL), with a median of 30.2, and 0.19 – 0.56 (Ratio35), with a median of 0.4. ACL generally fluctuates between 29 and 31. Noteworthy is the drop in ACL around 204 mbs, which is due to this sample containing a relatively high amount of C_{25}.

ACL and Ratio35 vary coherently throughout the studied interval (Pearson's correlation test, $\rho = 0.93$, $p < 0.0001$).

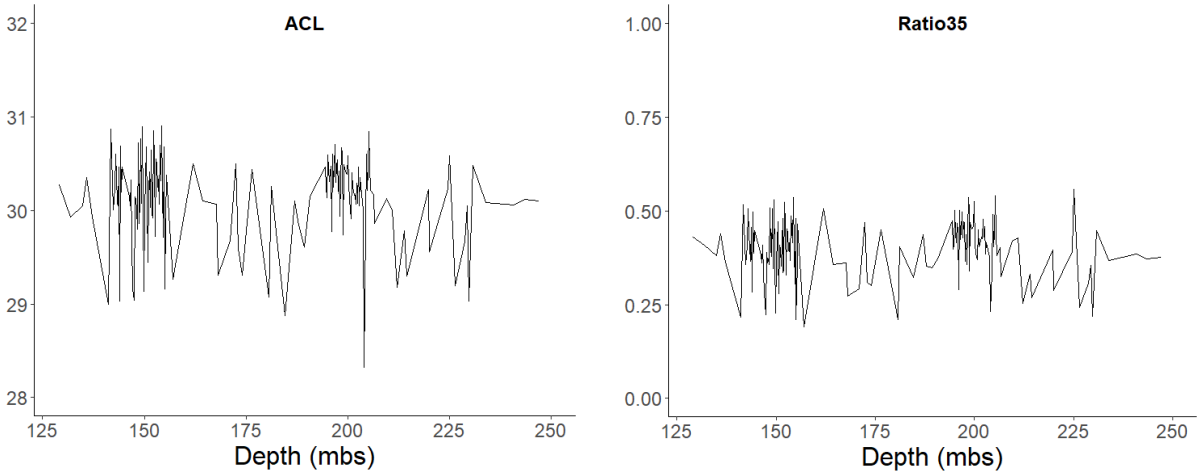

Figure 14. ACL (left) and Ratio35 (right) record.

4.7. Spectral analyses

The spectral analysis of the detrended bulk $\delta^{13}C$ record reveals a long eccentricity signal in the range of ~0.05 – 0.11 cycles/m, a short eccentricity signal in the range of ~0.2 – 0.4 cycles/m, an obliquity signal in the range of ~0.8 – 1.1 cycles/m and a precession signal in the range of ~1.45 – 1.7 cycles/m (Fig. 15).

The spectral analysis of the detrended bulk MS record reveals a long eccentricity signal in the range of ~0.05 – 0.13 cycles/m, a short eccentricity signal in the range of ~0.3 – 0.62 cycles/m, an obliquity signal in the range of ~0.85 – 1.35 cycles/m and a precession signal in the range of ~1.65 – 2.1 cycles/m (Fig. 16), roughly in the same ranges of the orbital signals found in the bulk $\delta^{13}C$ record.

Figure 17 shows the detrended $\delta^{13}C$ and MS records together with the long and short eccentricity Gaussian bandpass filters in their respective ranges.

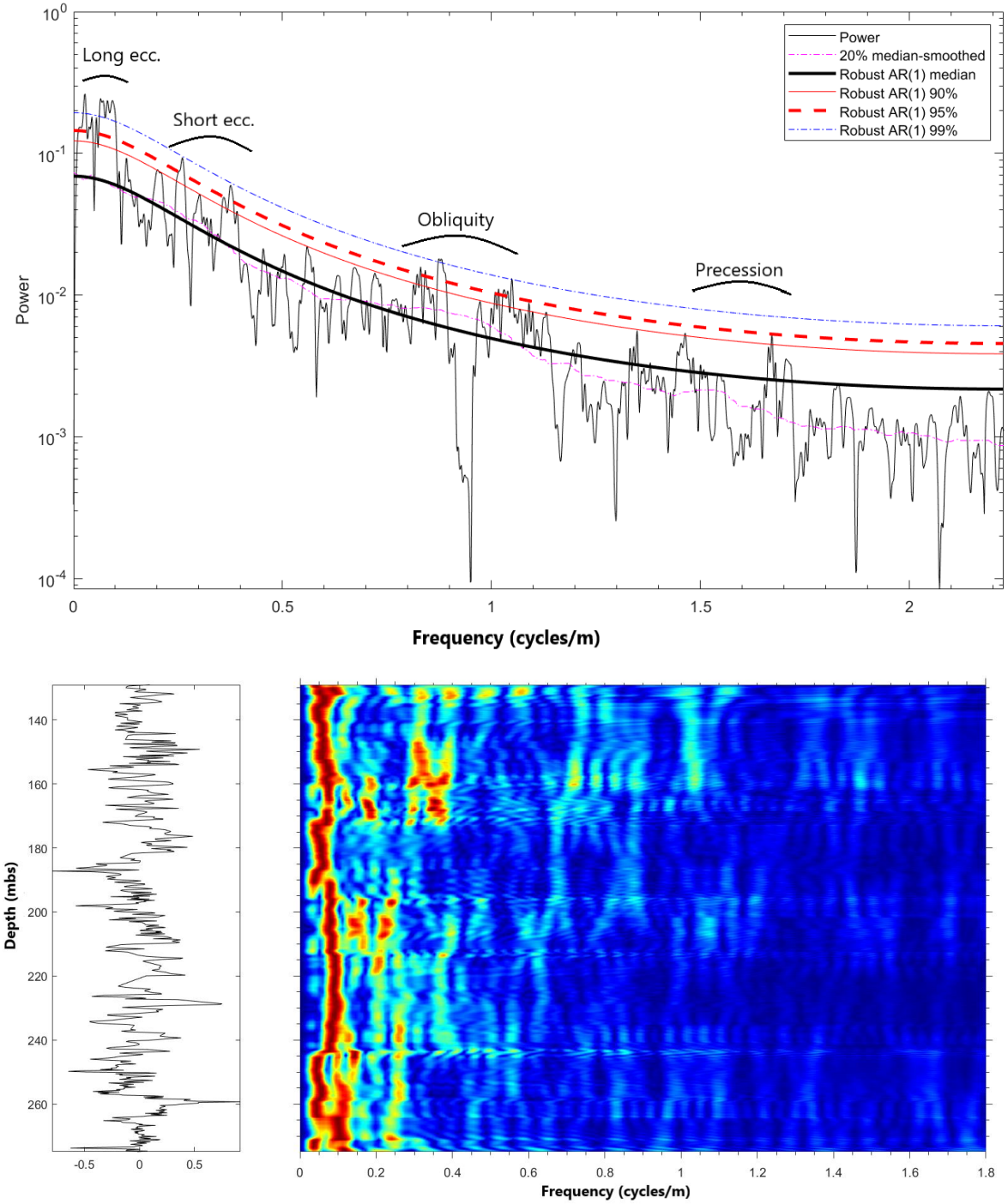

Figure 15. Spectral analysis (top) of the detrended bulk $\delta^{13}C$ record from 275 to 129 mbs (bottom-left) and evolutionary spectral analysis of the detrended bulk $\delta^{13}C$ record (bottom-right). (a) The spectral analysis uses the multi-taper method with robust autoregression (AR) statistical test for significant power of the frequencies, showing the 90%, 95% and 99% confidence limits. The y-axis (top) is on a logarithmic scale. The presumed ranges of frequencies (cycles/m) representing the orbital parameters are shown with curly brackets (i.e. $f_{low} - f_{high}$). Note that the isotope data resolution is not equal along the studied interval, resulting in variable power of the various frequencies along the core. Bulk carbon isotope data from 275 to 247.5 mbs are from Mannucci et al. (in prep).

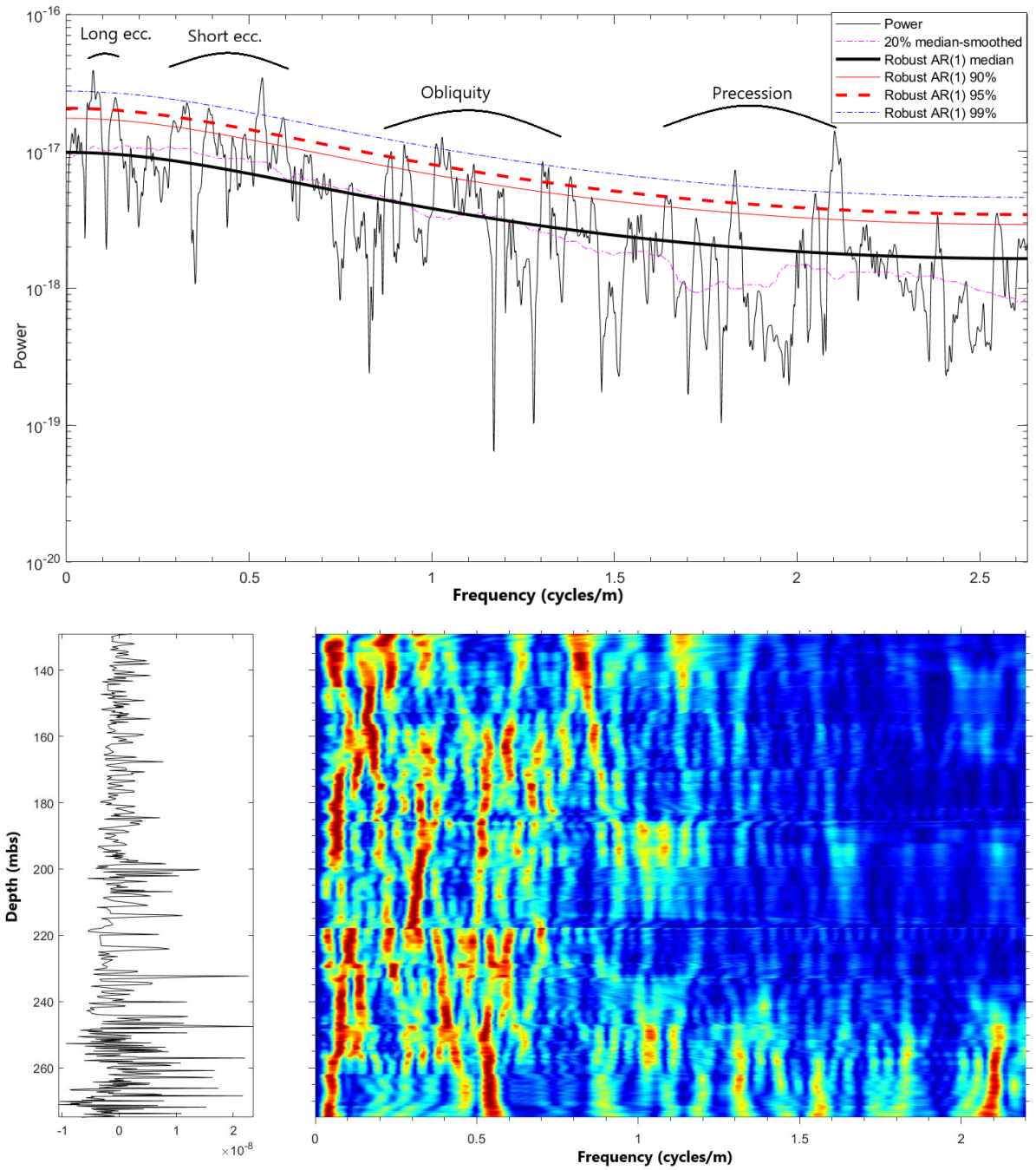

Figure 16. Spectral analysis (top) of the detrended bulk MS record from 275 to 129 mbs (bottom-left) and evolutionary spectral analysis of the detrended bulk MS record (bottom-right). (a) The spectral analysis uses the multi-taper method with robust autoregression (AR) statistical test for significant power of the frequencies, showing the 90%, 95% and 99% confidence limits. The y-axis (top) is on a logarithmic scale. The presumed ranges of frequencies (cycles/m) representing the orbital parameters are shown with curly brackets (i.e. $f_{low} - f_{high}$). Note that the isotope data resolution is not equal along the studied interval, resulting in variable power of the various frequencies along the core. Bulk MS data from 275 to 247.5 mbs are from Mannucci et al. (in prep).

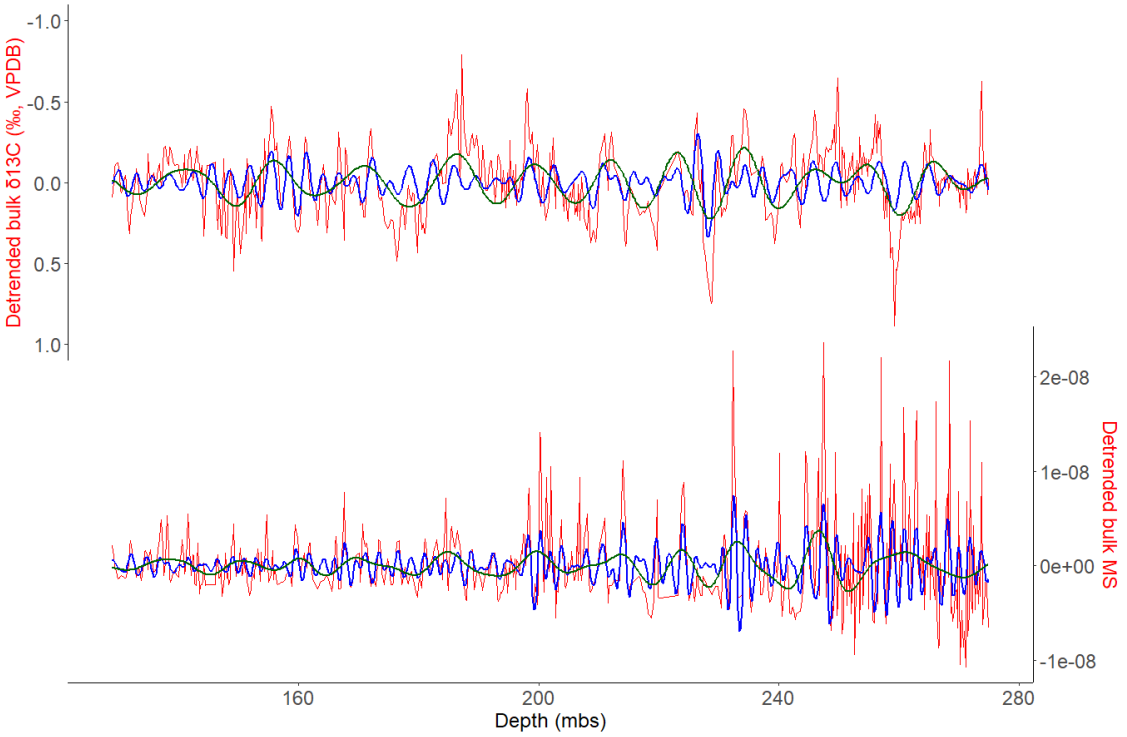

Figure 17. The detrended bulk $\delta^{13}C$ (top) and MS (bottom) records with long (dark green) and short (blue) eccentricity filters as determined through spectral analysis (Fig. 15 and Fig. 16). The relative amplitude of the filters is proportional to the signal strength for that part of the record. Bulk carbon isotope and MS data from 275 to 247.5 mbs are from Mannucci et al. (in prep).

5. Discussion

5.1. Integrated stratigraphy

As Fokkema et al. (2022) discussed, the bulk stable carbon isotope record of RH-323 is of decent quality, with little signs of secondary precipitation or recrystallisation of the carbonate (see Fokkema et al. (2022) for a full discussion on the quality of the RH-323 carbonate). This quality is reflected by the evident short term variability in the stable oxygen and carbon isotope records. Diagenetic alteration of the carbonate would have likely masked this short term variability, and would have resulted in a more uniform set of linear regressions between the records for the various depth ranges (Fig. 8). For Early Paleogene sediments predominated by $CaCO_3$, bulk stable carbon isotope records can be correlated to deep sea benthic records at high temporal resolution (e.g. Lauretano et al., 2016). This is due to orbitally forced rapid carbon cycling between various surficial carbon reservoirs, and the global carbon cycle, during that period (Kirtland Turner et al., 2014; Sexton et al., 2011; Zeebe et al., 2017).

In this study, the bulk stable carbon record was correlated to the deep ocean benthic foraminifera stable carbon isotope record of Westerhold et al. (2017) (i.e. ODP 1258 and 1263, Demerara Rise and Walvis Ridge respectively) (Fig. 18). The eccentricity bandpass filters found in section 4.7 were used as a reference. It was decided to not use the bulk MS record and eccentricity filters to devise the age model, as the filters showed a poorer representation throughout the whole record as compared to the bulk $\delta^{13}C$ record and filters, especially from ~220 – 129 mbs. This is in contrast with the cyclostratigraphic work done by Mannucci et al. (in prep), for the interval of 306.5 – 247.5 mbs, which was primarily based on bulk MS. This inconsistent filter signal is possibly due to the low bulk MS values for the ~220 – 129 mbs interval, causing a clipped eccentricity signal.

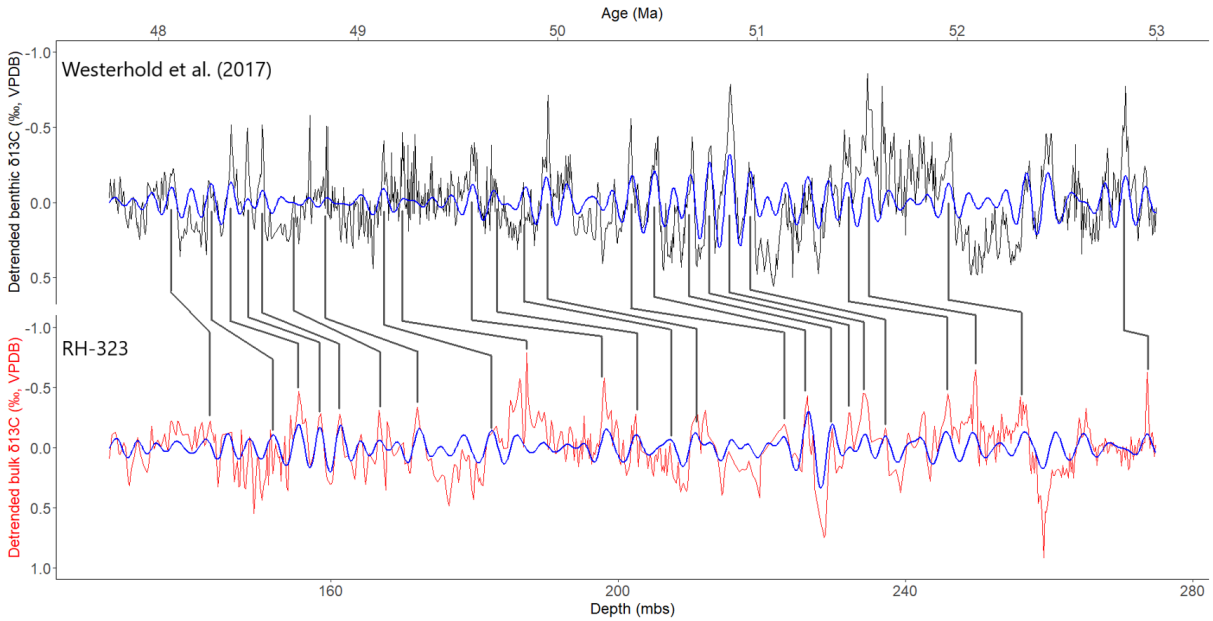

Figure 18. Chemostratigraphic correlation of the bulk $\delta^{13}C$ record (bottom) with the deep sea benthic record of Westerhold et al. (2017) (top). Blue lines represent short eccentricity filters.

Guided by the eccentricity filters and biostratigraphy of core RH-323, the chemostratigraphic correlation resulted in 23 tie-points (Fig. 18), which allowed for an extension of the orbital age model of RH-323 from 247.5 to 134.6 mbs (Fig. 19). Tie-points were based on the identification of known CIEs and hyperthermal events as identified in Westerhold et al. (2017), and the known number of short eccentricity cycles between them, for which the bandpass filters served as a reference. A comparison between the new chemostratigraphic tie-points with the lower resolution $\delta^{13}C$ tie-points of Fokkema et al. (2022), shows the old tie-points were roughly in the same range, albeit with a seemingly more constant sedimentation rate. The new higher-resolution tie-points reveal an increasing sedimentation rate throughout the core (see section 5.2). Ultimately, the age-depth points corresponding to the

cyclostratigraphic work done by Mannucci et al. (in prep) and the chemostratigraphic alignment done in this study (i.e. orange and purple points in Fig. 19), were combined and interpolated to serve as the definitive age model to be applied to study the data in the studied interval of 275 to 129 mbs in the time domain (~53 – 47.8 Ma).

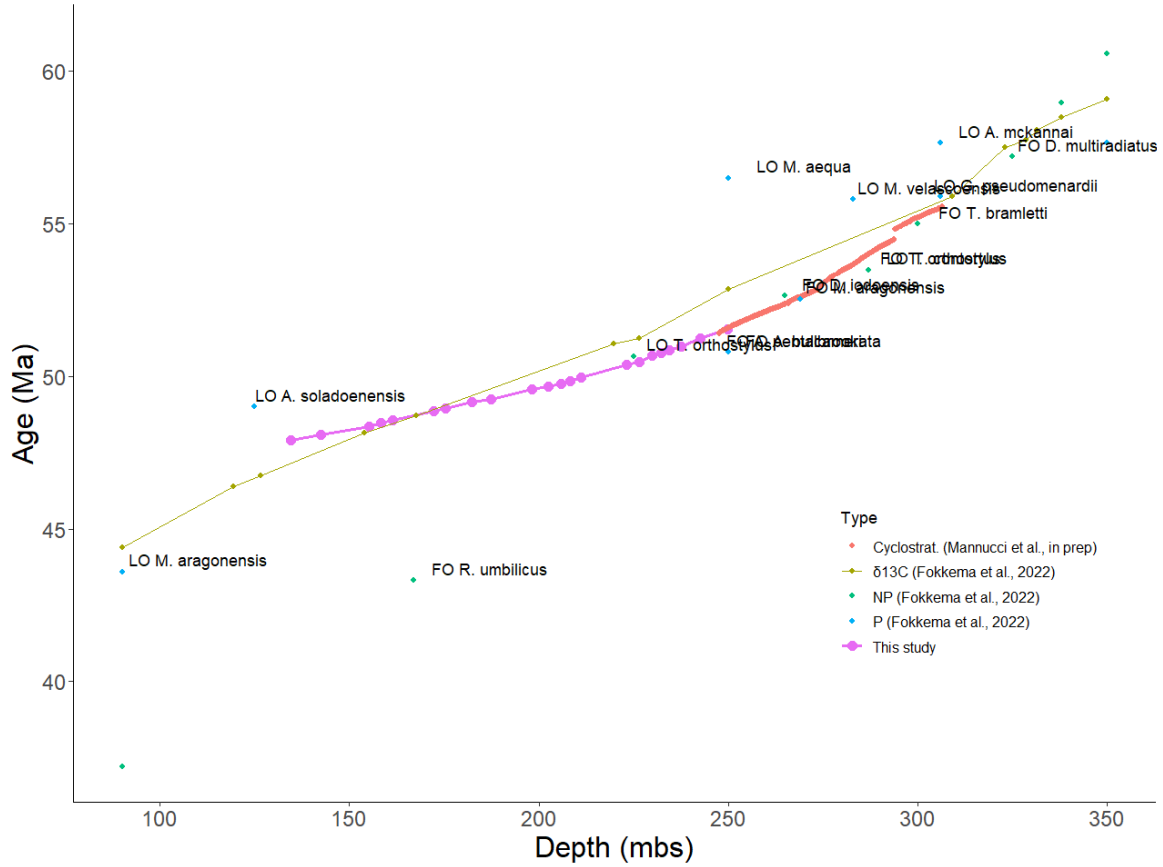

Figure 19. The age-depth model based on $\delta^{13}C$ chemostratigraphic correlation (purple; this study, green; Fokkema et al., 2022), bio-stratigraphic tie-points based on first and last occurrence (FO and LO, resp.) of calcareous nannofossils (NP; blue) and planktonic foraminifera (P; purple) (Fokkema et al., 2022), and cyclostratigraphic tuning (orange; Mannucci et al., in prep). Note the FO *R. umbilicus* biostratigraphic tie-point deviates from the other tie-points, likely due to faulty labelling of the sample.

A comparison of the bulk $\delta^{13}C$ vs. age record with the benthic $\delta^{13}C$ record of Westerhold et al. (2017) shows good correspondence of the long and short eccentricity filters, and CIEs K (ETM3) to W and C22nH4, C21rH1 and C21rH4. This validates the tie-points as depicted in Figure 18, and it implies the derived age model serves as good age reference in a resolution of at least short eccentricity.

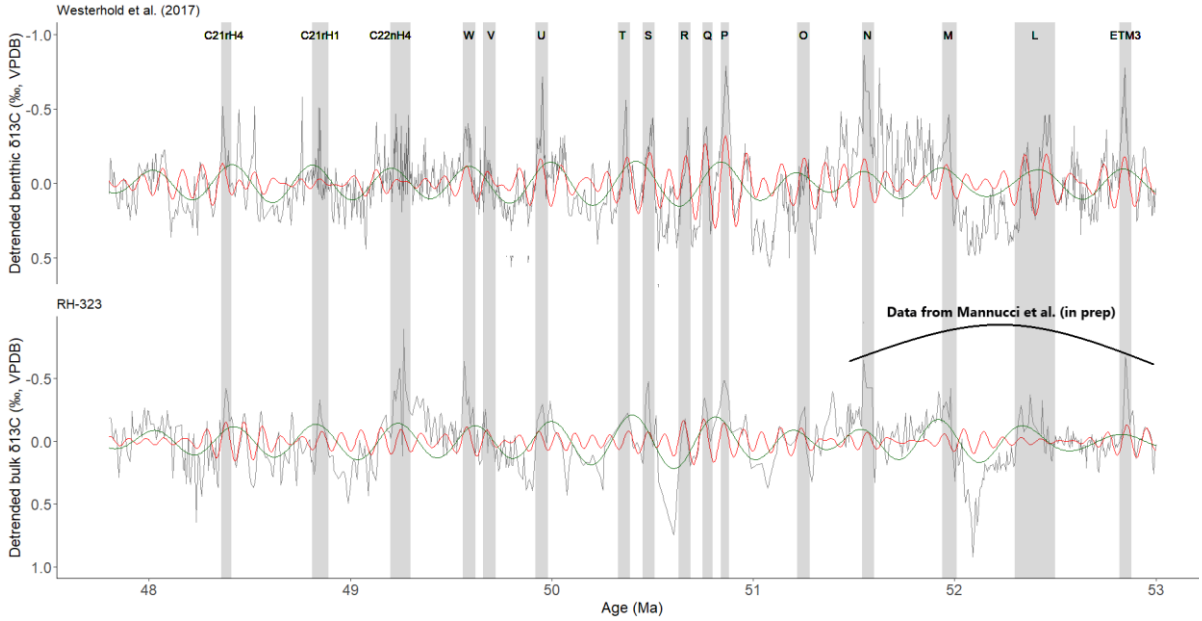

Figure 20. Detrended bulk $\delta^{13}C$ record (bottom) of RH-323 compared to the detrended benthic deep sea $\delta^{13}C$ record of Westerhold et al. (2017). Grey bars represent hyperthermals. Red lines represent short eccentricity filters and green lines represent long eccentricity filters. Range of data originating from Mannucci et al. (in prep) indicated with the black curve.

5.2. Sedimentation rate

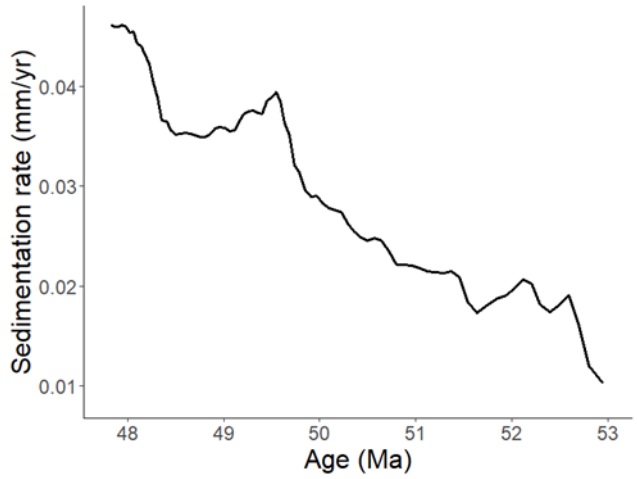

Figure 21. The reconstructed sedimentation rate throughout the studied interval.

Applying the age model to the depth measurements of all samples allows for the determination of sedimentation rate (in mm/yr). This was done by differentiating the resulting age versus depth relationship (see supplementary material; Fig. S8). The reconstructed sedimentation rate increased ~4.5-fold from 53 to 48 Ma, from around 0.01 to 0.05 mm/yr. This long term increase in sedimentation rate corresponds to a recorded long term increase in [$CaCO_3$] and decrease in bulk MS values throughout the whole core (Fig. 7, Fokkema et al., 2024; Chapter 6 and Mannucci et al., in prep). This suggests a diamagnetic forcing, such as $CaCO_3$ production rate, determined sedimentation substantially. This is validated by the correlation between the bulk MS values and reconstructed $CaCO_3$ content (Fig. 22), which shows a significant negative correlation ($\rho(663)= -0.30$, $p<0.00001$). Therefore, it is reasonable to suggest the overall increase in sedimentation was caused by an overall increase in $CaCO_3$ production. This implies primary productivity increased throughout the studied interval, which is validated by the long term increase in crenarchaeol production (Fig. 12). Furthermore, a preliminary assessment of the

dinocyst assemblage showed an increase in abundances from about 270 – 250 mbs (~53 – 52 Ma) onwards (unpublished). A palynological follow-up study is needed to further assess this.

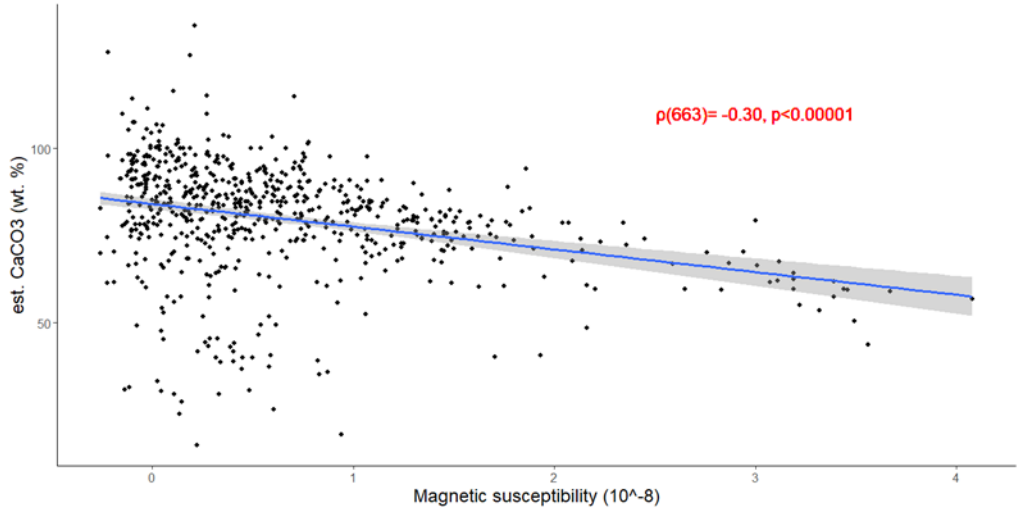

Figure 22. MS versus estimated $CaCO_3$ content (in weight %), with linear regression line with 95% CI envelope in blue and grey respectively. The Pearson's correlation statistics are displayed in red.

5.3. Temperature development

5.3.1. Long term trends

5.3.1.1. Early EECO warming

Figure 23 depicts the TEX_{86} based temperature record of RH-323 tuned with the extended age model. It shows the long term warming trend recorded from 275 to 250 mbs to correspond to early EECO warming (~53 to 51.5 Ma). This warming trend coincides with high resolution deep sea benthic $\delta^{18}O$ records, and also with the lower resolution southern high-latitude record of ODP 1172 (60 °S). In contrast, the single other tropical SST record (i.e. ODP 959; eastern equatorial Atlantic, 9 °S) shows a ~2 °C cooling from 53 to 51.5 Ma, and the mid-latitude (46 °S) Southwest Pacific record of Mid Waipara shows an overall cooling throughout the whole EECO (Crouch et al., 2020; Fokkema et al., 2023).

Considering the correspondence of RH-323 with the deep sea (and high-latitude ODP Site 1172), it seems the southern Tethys temperatures developed synchronously with changes in the global climate, whereas the eastern equatorial Atlantic and Mid Waipara SSTs were likely more influenced by local factors, for example, changes in upwelling intensity (for ODP 959) and Tasman Gateway opening during the early Eocene (for Mid Waipara) (Bijl et al., 2021). Increased upwelling during the EECO seems likely, as the latitudinal temperature gradients (LTG) increased from ~19 to 21 °C, as determined by the difference between tropical mean SST and deep-ocean temperatures (Cramwinckel et al., 2018). Increasing LTGs would have enhanced Hadley Cell circulation (cf. Burls & Fedorov, 2017), possibly inducing increased upwelling and local cooling for the eastern equatorial Atlantic. In the interval of ~54 – 52 Ma, Fokkema et al. (2023) found no signs of upwelling in the dinocyst assemblage. This dinocyst record (and other proxy records for upwelling) should be extended to cover the whole EECO. This will help evaluate potential changes in upwelling during the EECO and assess whether this could account for the deviation in SST trends at ODP Site 959 from global temperature trends.

The SST increase recorded for the southern Tethys ~53 – 52 Ma, could be explained by increasing background levels of pCO_2 throughout the EECO. From around 53 to 51 Ma, reconstructed global $pCO2$ increases from approximately 1300(±150) to 1700(±200) ppm (Anagnostou et al., 2020). Considering an early Eocene climate sensitivity of 4.5 °C per doubling of CO_2 (Lunt et al., 2021), and EECO background CO_2 concentrations of around 1500 ppm, the recorded warming of ~1 °C would require a ~220 ppm forcing in CO_2, which is within the range of reconstructed CO_2 concentrations (Anagnostou

et al., 2020). Since this warming is not witnessed for the eastern equatorial Atlantic, this would imply upwelling at ODP Site 959 may have been enhanced enough to compensate the pCO_2 forced temperature increase.

5.3.1.2. Early to middle Eocene cooling

The systematic cooling of ~1 °C recorded around 187 mbs in the TEX_{86} and $\delta^{18}O$ records corresponds to an age of ~49.2 Ma (Fig. 23). The onset of this long term cooling trend is consistent with the high-latitude ODP Site 1172 (60 °S) and deep sea records (Fig. 23). This suggests it was initiated by a global forcing, such as changing pCO_2 levels. Indeed, a transient drop in reconstructed pCO_2 is recorded around 50.5 Ma, followed by a long term drop from ~49 Ma (Anagnostou et al., 2020). Again, considering an early Eocene climate sensitivity of 4.5 °C per doubling of CO_2 (Lunt et al., 2021), and EECO background CO_2 concentrations of around 1500 ppm, the recorded cooling of ~1 °C would require a ~220 ppm drop in CO_2 concentrations, which is within the range of pCO_2 reconstructions (Anagnostou et al., 2020).

Increased silicate weathering (e.g. Misra & Froelich, 2012) due to orogenic events such as the formation of Patagonia (~50 Ma) (Maffione et al., 2010) and the collision of the Indian plate with Eurasia (~47 Ma) (Zahirovic et al., 2016), could have been an important factor in the recorded CO_2 drawdown. Moreover, increased carbon burial rates, for example associated with the *Azolla* event (Barke et al., 2012; Brinkhuis et al., 2006), could have also contributed to substantial CO_2 drawdown. Freshening of Artic surface waters during the early middle Eocene resulted in favourable conditions for *Azolla* blooms around ~49 Ma (Barke et al., 2012). Bottom water anoxia resulted in increased organic matter burial, which could have potentially resulted in up to 470 ppm CO_2 drawdown (Speelman et al., 2009). Lastly, reduced degassing of CO_2 through lower seafloor spreading rates could have also played an essential role in the observed pCO_2 drop (Bouligand et al., 2006), however this would be paradoxical in respect to the abovementioned increase in orogeny. Clearly, it remains ambiguous what exact driver or synergy of drivers caused the recorded drop in pCO_2, and with that the onset of early middle Eocene cooling. For a more extensive discussion on potential drivers of CO_2 drawdown around 49 Ma, see Anagnostou et al. (2020).

The cooling is also recorded in the Mid Waipara record, however it was initiated at an earlier stage (~51 Ma). The exact cause of this is not clear, however as stated above, possibly ocean circulation changes through gradual Tasman Gateway opening played a role in this (Bijl et al., 2021). Lastly, the cooling is also recorded at ODP Site 959 around 49 Ma, however, the data around the late EECO–onset cooling (~50 – 48 Ma) is too scarce to make a reasonable comparison with RH-323. Possibly due to the further increase of LTGs (Cramwinckel et al., 2018), upwelling along the eastern equatorial Atlantic increased throughout the onset of the cooling, and with a polar amplification (PA) factor of ~1.7 – 2.3 (Fokkema et al., 2023), global cooling could have caused upwelled water to be increasingly colder. For this reason, the magnitude of cooling was possibly amplified in the eastern equatorial Atlantic, in respect to the southern Tethys. Clearly, more integrated model and proxy data for ODP Site 959 are needed to study this in detail, for example through the abovementioned extension of the dinocyst assemblage and other proxies for upwelling (Lazarus et al., 2006; Sluijs et al., 2005), combined with a more extensive SST record for ODP Site 959.

In sum, it seems the long term temperature trends recorded in RH-323 are reflective of global climate change, which suggests that indeed around 49.2 Ma the global climate started cooling systematically, both in low-latitudes as well as high-latitudes (Fig. 23), caused by a global forcing.

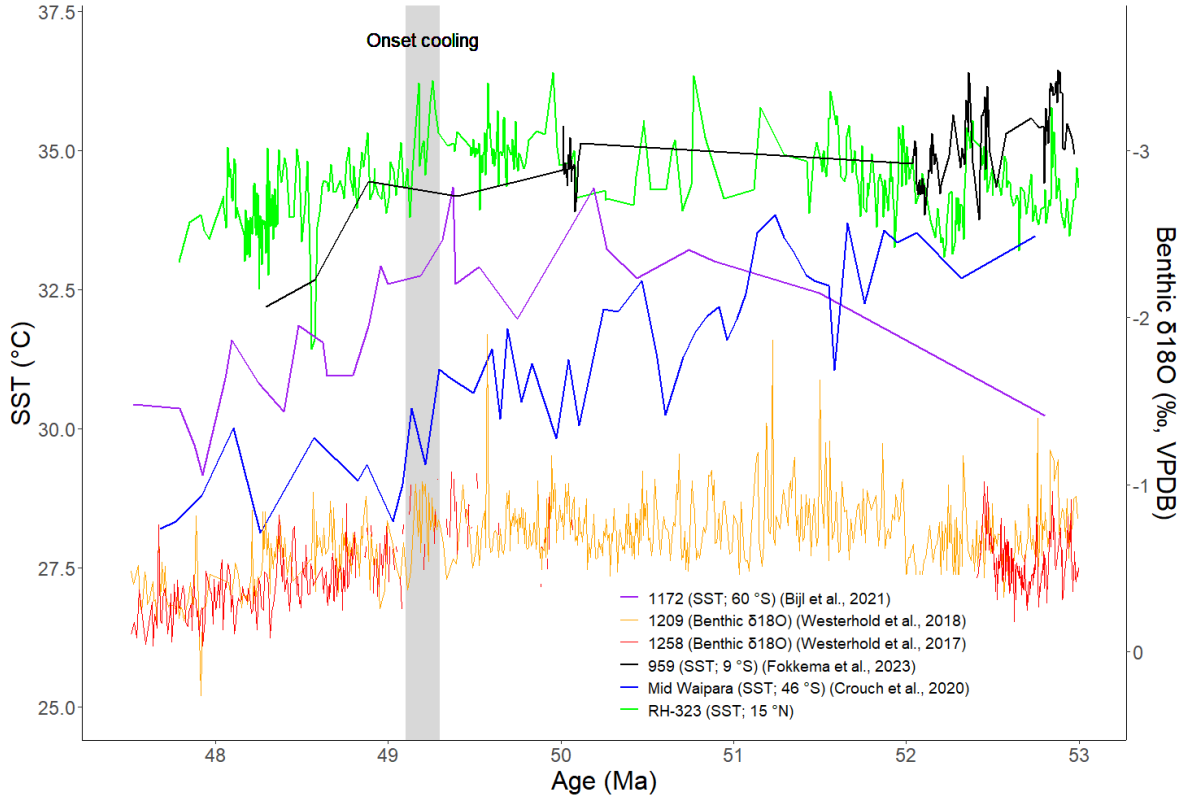

Figure 23. Various TEX_{86} SST and benthic deep sea $\delta^{18}O$ records compared. Onset of southern Tethys cooling shown with grey bar. Numbers in legend represent ODP cores. Paleolatitude of SST records is given. Adapted from (Bijl et al., 2021; Crouch et al., 2020; Fokkema et al., 2023; Westerhold et al., 2017, 2018).

5.3.2. Short term trends

The TEX_{86} based temperature peaks found corresponding with the peaks in the bulk $\delta^{13}C$ record (Fig. 24) all correspond to previously identified CIEs and hyperthermal events in deep sea records (Lauretano et al., 2018; Westerhold et al., 2017, 2018). The RH-323 hyperthermals correspond to a warming in a magnitude of ~1 – 2 °C SST (0.7 – 1.3 subSST), which is in line with the hyperthermals identified in ODP site 959 (Fokkema et al., 2023), but lower than the ~3 – 4 °C PETM and ETM2 SST warming at site RH-323 (Fokkema et al., 2024; Chapter 6). Considering most of the hyperthermals found in the TEX_{86} record are single datum points, interpretation should be done cautiously. However, the hyperthermals are correspondingly found in the bulk $\delta^{18}O$ (temperature) record (Fig. 24), and larger than the analytical uncertainty. It is therefore reasonable to consider these TEX_{86} excursions as true climatological signals. It should be noted that SST reconstructions derived from the bulk $\delta^{18}O$ record should be interpreted as crude estimates of SST and SST variability, and are used here solely as a comparison with the TEX_{86} derived SSTs. It is interesting, however, the $\delta^{18}O$ based temperature trends are more or less in the range of the TEX_{86} based SST trends. This implies that carbonate production primarily occurred within the surface mixed layer, and that the carbonate is indeed minimally affected by diagenetic alteration.

Most EECO hyperthermals as previously recorded in deep sea temperature records (Lauretano et al., 2018; Westerhold et al., 2018), are recorded in the RH-323 TEX_{86} record. Hyperthermal O is absent from the TEX_{86} record as the corresponding sample exceeded the Δ-RI outlier criterium (see section 4.4), and hyperthermals P and T are absent due to no samples being analysed for these time intervals. However, hyperthermals O, P and T are recorded in the $\delta^{18}O$ derived SST record (Fig. 24). Considering all CIEs coincide with eccentricity maxima (Fig. 24) (Westerhold et al., 2017), the RH-323 record is the only SST record besides the ODP Site 959 record (Fokkema et al., 2023), that shows the consistent presence of transient global warming events on orbital (eccentricity) resolution. This confirms the global scale that is associated with the proposed eccentricity forced carbon cycle perturbations, as represented

by these CIEs (e.g. Kirtland Turner et al., 2014; Sexton et al., 2011; Zeebe et al., 2017). Not all eccentricity maxima are correlated with pronounced CIEs and temperature shifts, as observed not only in RH-323 but also in deep-sea records (e.g. Lauretano et al., 2018; Westerhold et al., 2018). This is speculated to stem from the size of charged carbon reservoirs (e.g. methane hydrates, permafrost, and/or marine dissolved organic carbon), which depend on the frequency of surpassing a thermodynamic threshold, triggering carbon release (Kirtland Turner et al., 2014; Sexton et al., 2011). Such thresholds are more easily surpassed in the warmer climate of the EECO, which potentially leads to inhibited carbon reservoir charging. This may have also contributed to the recorded hyperthermals during the body of the EECO (53 – 50 Ma) to be of a smaller magnitude (~1 – 2 °C) than the warming recorded for ETM2 (~3 – 4 °C) (cf. Fokkema et al., 2024; Chapter 6).

Nonetheless, the $\delta^{18}O$ record (Fig. 24) seems to show that all eccentricity maxima are at least associated with some transient temperature increase. This is also confirmed by the spectral analysis of the bulk $\delta^{18}O$ record vs. age, which shows significant power in the short eccentricity band (Fig. 29), in line with what Kirtland Turner et al. (2014) found in their equatorial Atlantic bulk $\delta^{18}O$ record. Therefore, it seems that perturbations in the carbon cycle driven by eccentricity naturally result in some degree of global temperature fluctuations. However, the extent to which these temperature peaks are amplified enough to be classified as 'hyperthermals', as in cases like hyperthermals K (ETM3) – W, possibly depends largely on the amount of carbon initially charged and subsequently released.

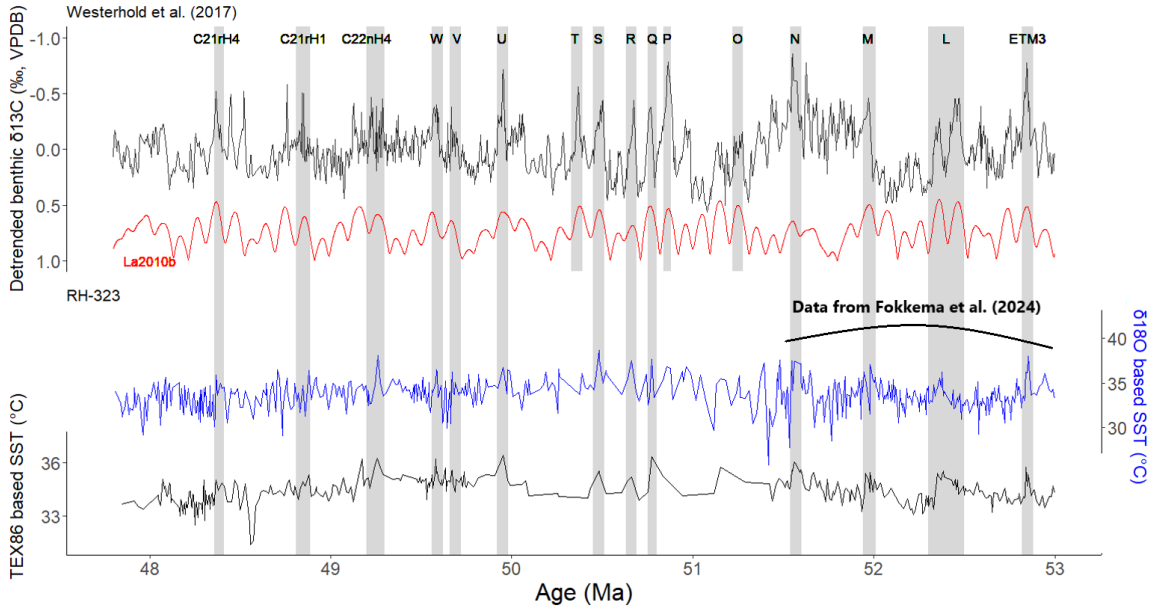

Figure 24. Detrended benthic deep sea $\delta^{13}C$ record of Westerhold et al. (2017) compared with La2010b astronomical solution for eccentricity (red; not to scale), and $\delta^{18}O$ and TEX_{86} derived SST reconstructions of RH-323 (blue and black, respectively). Grey bars represent hyperthermals. Range of data originating from Fokkema et al. (2024; Chapter 6) indicated with black curve.

5.4. Variability in the hydroclimate

Overall, the MS, brGDGT and n-alkane proxies combined suggest the hydroclimate around the paleosite of RH-323 to be arid. The n-alkane distributions are reminiscent of present-day arid and semi-arid environments (Bliedtner et al., 2018; Carr et al., 2014; Struck et al., 2020), and the MS and the BIT values are low, certainly in comparison to the early part of the EECO (Fokkema et al., 2024; Chapter 6), suggesting minimal river discharge. Because of this, any variability in these records should not be interpreted as a shift from wet to dry, but rather from (semi-)arid to more arid, or vice versa.

5.4.1. Hydrological change throughout the early to middle Eocene

5.4.1.1. Overall aridification throughout the EECO

This study assumed the MS record to generally reflect river discharge of clay minerals (e.g. smectite). However, MS values are also affected by the deposition of paramagnetic clay minerals through dust (e.g. palygorskite and kaolinite) (Foucault & Mélières, 2000). Therefore, it remains ambiguous what the exact driver of the MS peaks is, without a measure of dust input. However, these two factors (i.e. dust deposition versus river discharge) don't necessarily contradict the interpretation of the MS record. Atmospheric dust uptake and transport are enhanced in arid conditions (Tegen et al., 2002), however, dust deposition is enhanced through rainfall (i.e. wet deposition) (Löye-Pilot et al., 1986;Van Der Does et al., 2020, 2021). This means the MS peaks possibly reflect amplified seasonal contrasts in rainfall and vegetation cover: arid months enhance atmospheric dust loading, and wet green months enhance dust deposition (Tegen et al., 2002).

This is in line with increases in dust deposition found corresponding with parts of sapropels (Liu et al., 2012). Sapropels reflect enhanced Nile river discharge, and are generally associated with MS peaks and dust deposition minima (Larrasoaña et al., 2003, 2008). However, some sapropels do show a positive correlation between dust input and MS, and/or short bursts of dust input (Liu et al., 2012), possibly reflecting periods of intensified rainfall induced dust deposition. However, generally sapropels are associated with a more humid and vegetation rich North Africa (Grant et al., 2022; Larrasoaña et al., 2013), in which atmospheric dust loading is restricted, and clay minerals are instead sequestrated in lake sediments, soils and river beds (Ehrmann et al., 2017), explaining the positive relationship between MS and river discharge in these humid (i.e. sapropel forming) periods.

The soil clay mineral retention and erosion cycle operates on centennial or millennial scales (Wattel-Koekoek et al., 2003, 2004), making the MS record data resolution insufficient for a detailed study on clay mineral residence time on land. However, hinterland aridification would decrease the total amount of weathered minerals, reducing input to the clay mineral pool (Eberl, 1984). Thus, total clay mineral production, as a function of overall weathering rates (i.e. rainfall) (Eberl, 1984), seems to be the primary determinant of the bulk MS values over the studied timescales, with minimal impact of short-term clay mineral cycling on land.

Taking this into account, the overall decrease in the amplitude of variability of the MS record points towards an overall aridification: overall reduced rainfall led to a reduction in the total amount of clay minerals available to be stored and eroded, decreasing the magnitude of MS peaks. This is in line with the long term aridifying trend found for the earlier Eocene (56 – 51.5 Ma) (Fokkema et al., 2024; Chapter 6).

5.4.1.2. Soil input versus marine in situ production of brGDGTs

Overall aridification is also recorded by the long term decrease in BIT and increase in #RingsTetra for the first half of the EECO (to ~51 Ma) (Fig. 28). Reduced river discharge would cause a relative decrease in brGDGT input (i.e. decreasing BIT). Alternatively there is a reduction of soil formation, however combined with the recorded decrease in MS values throughout the studied interval, it seems the low BIT values indeed reflect limited river discharge. Accordingly, there is an increase in the relative abundance of marine *in situ* produced brGDGTs (i.e. increasing #RingsTetra). The IR index remains relatively

constant throughout the studied interval, which suggests river *in situ* production of brGDGTs did not substantially change.

During the end-EECO and through the onset of cooling (~51 – 47 Ma), the environment appears to have remained in a stable arid state, as indicated by the consistently low MS/BIT values and the #RingsTetra values being generally larger than 0.5 (Fig. 28). Therefore, most of the variability observed in the BIT and #RingsTetra indices is likely attributed to fluctuations in marine *in situ* production or sedimentary preservation of GDGTs.

The coherency in crenarchaeol and brGDGT absolute abundances (Fig. 25) suggests they were influenced by a confounding factor, such as fluctuations in nutrient availability, possibly driven by variations in river discharge or dust deposition. For instance, during hyperthermal N, U, and C22nH4 (Fig. 25), significant increases in brGDGT and crenarchaeol production coincide with MS peaks, despite BIT, #RingsTetra, and IR indicating predominant marine *in situ* brGDGT production. This possibly reflects increased input of minerals from rivers or dust (i.e. increasing MS), leading to elevated marine *in situ* GDGT production (i.e. increasing crenarchaeol and brGDGT abundances).

Alternatively, this coherency could be the result of changing preservation of organic matter throughout the core. Lengger et al. (2013) have shown brGDGTs to be more resistant to oxidative degradation than crenarchaeol, meaning the BIT index would increase during low points in Figure 25 if these fluctuations indeed represent preservation (Lengger et al., 2013). However, the BIT variability is too low (< instrumental error) to differentiate between actual fluctuations in production or preservation for this part of the record. Additional total organic carbon (TOC) measurements could perhaps elucidate this matter.

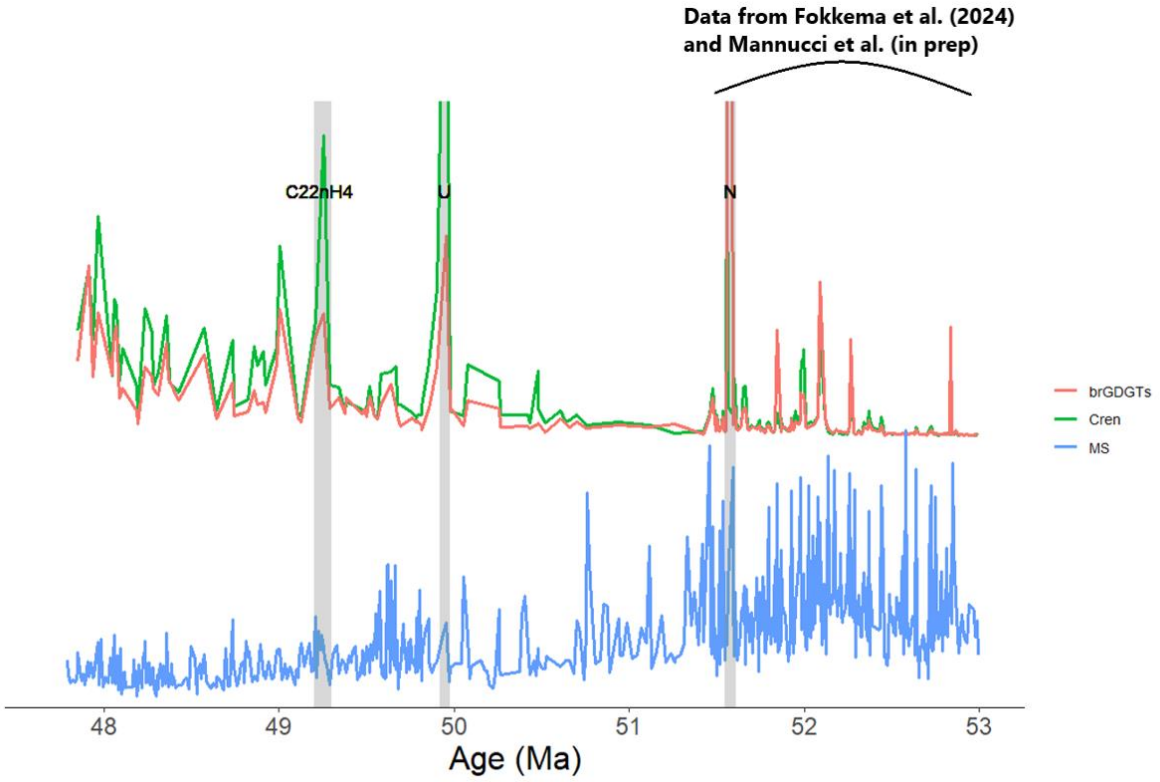

Figure 25. Crenarchaeol (cren) and brGDGT abundances (ng/g sediment) and MS. Grey bars represent examples of hyperthermals in which peaks in abundance are associated with MS peaks. Y scales of the abundances and MS are according to Figure 12 and 7, respectively. Range of data derived from Fokkema et al. (2024; Chapter 6) (GDGTs) and Mannucci et al. (in prep) (MS) indicated with the black curve.

5.4.1.3. Limited terrestrial influence during the end-EECO

All things considered, during the end-EECO and over the onset of the cooling, the brGDGT indices show a small terrestrial contribution to brGDGT input. This could be because of the low river discharge in the area due to arid conditions, as also evident from the MS record. Additionally, the paleolocation of the core could be located too far distally or laterally from rivers to be sufficiently influenced by riverine input of brGDGTs (Yedema et al., 2023; Zell et al., 2014). The reconstructed sedimentation rates indeed reflect open ocean conditions, and so do the absolute abundances of crenarchaeol and brGDGTs (Sinninghe Damsté, 2016). It is most parsimonious to suggest the MS and brGDGT proxies combined show an arid environment, with limited terrestrial influence. The terrestrial influence was most likely restricted to terrigenous nutrient input affecting marine production.

5.4.1.4. Hinterland vegetation

ACL values typically fluctuate between 29 and 31, suggesting an arid/semi-arid hinterland. This range resembles landscapes dominated by savanna herbs (i.e. grasses) and trees, as seen in present-day southern Africa (Fig. 26) (Carr et al., 2014; Vogts et al., 2009). African rain forest vegetation also has ACL values around ~29.7 (Vogts et al., 2009), however considering the bulk MS and BIT values suggest little soil formation and run-off, it is not likely the RH-323 samples with ACL in the lower range represent the presence of regional rain forests. This is validated by paleovegetational model simulations of early Eocene North Africa, which show the environment to generally consist of savanna, shrubland and desert biomes (Herold et al., 2014). As Bush and McInerney (2013) showed, there is high variability of the distribution of the C_{27}, C_{29} and C_{31} n-alkanes within plant groups, which occur widespread in both woody and non-woody plants. The demarcation between non-woody versus woody vegetation is primarily based on the dominance of C_{33} and C_{35} (Bush & McInerney, 2013). This is best represented by the Ratio35 index, which varies coherently with ACL, suggesting both proxies similarly record vegetational variability, as a weighted average of the contributions of non-woody and woody plants.

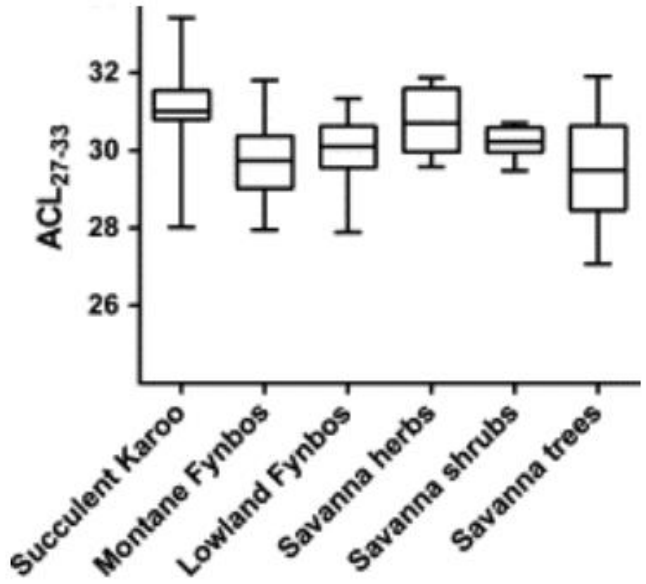

Figure 26. ACL (C_{27} to C_{33}) of different southern Africa vegetation types.
Adapted from: Carr et al. (2014) and Vogts et al. (2009).

Throughout the studied interval there are no systematic long term changes recorded for ACL and Ratio35, suggesting there was no long term trend towards a more woody or non-woody plant dominated environment. On the short term, the integrated source area of the n-alkanes seems to have fluctuated between a more tree rich and herb rich savanna environment. Pollen-based paleovegetational reconstructions of the area are needed to validate this. However, a preliminary assessment (unpublished) of terrestrial palynomorphs has shown pollen to be virtually absent from core RH-323 (Fokkema et al.,

2024; Chapter 6). The ACL drop around 204 mbs (~49.7 Ma) corresponds to hyperthermal V. However, considering the BIT and bulk MS record don't record a hydrological change in a similar magnitude, and considering the little small increase recorded for hyperthermal V (Fig. 24), it is more likely this sample was contaminated than it representing a true environmental signal.

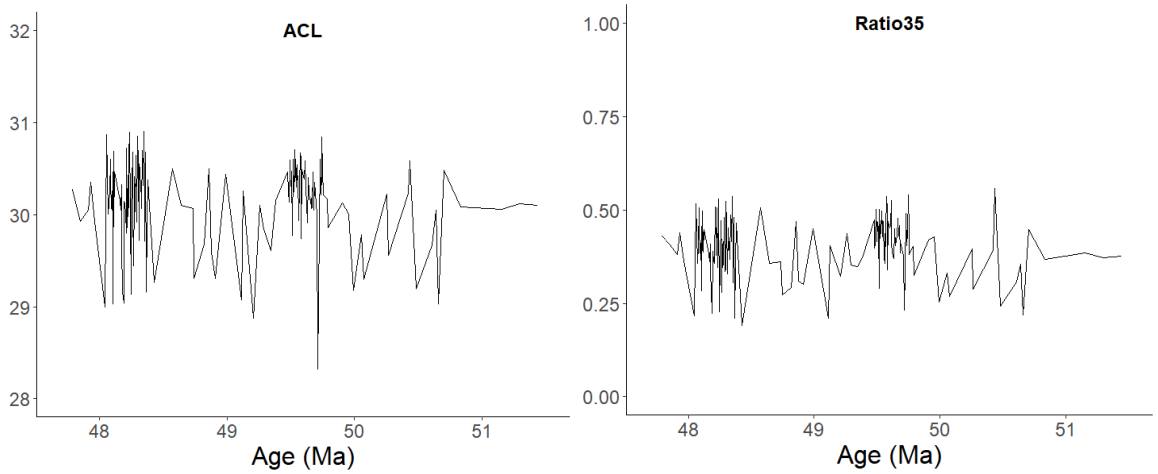

Figure 27. The ACL and Ratio35 records versus age.

5.4.1.5. The hydrological response of hyperthermals

A recent study done on the Horn of Africa climate of the past ~75 ka (Baxter et al., 2023), showed that the background climate state (i.e. overall background temperature state) determines whether there is a positive or negative relationship between temperature and precipitation, depending on the balance between temperature-dependent evaporation (i.e. thermodynamical component) and sea to land moisture transport (i.e. dynamical component). This changing temperature-moisture response has also been proposed to be responsible for the different hydrological responses recorded for some of the early Eocene (56 – 51.5 Ma) hyperthermals for site RH-323 (Fokkema et al., 2024; Chapter 6). For the interval of 247.5 to 129 mbs (~51.5 – 47.8 Ma), most of the identified hyperthermals lack a true hydrological response as recorded in the brGDGT and bulk MS records (Fig. 28). Only hyperthermal O seems to correspond to a peak in the BIT index. However this peak is not associated with a peak in MS, meaning either there is a peak in soil formation without enhanced river discharge of minerals, which seems unlikely; there is a peak in marine *in situ* production of brGDGTs, which also seems unlikely considering there is no peak in absolute abundances (Fig. 25); or the sample was not analysed/integrated properly. Considering it is a singe datum point (and so are the hyperthermals Q to U and C22nH4), it should not be overinterpreted. Overall, in the second half of the EECO (~51.5 – 50 Ma), hyperthermals did not substantially respond to the associated temperature changes hydrologically. This is coherent with the 'dry-gets-drier' principle: the background hydroclimate was so arid during the second half of the EECO (~51.5 – 50 Ma), that further transient warming likely did not result in any recordable additional aridification.

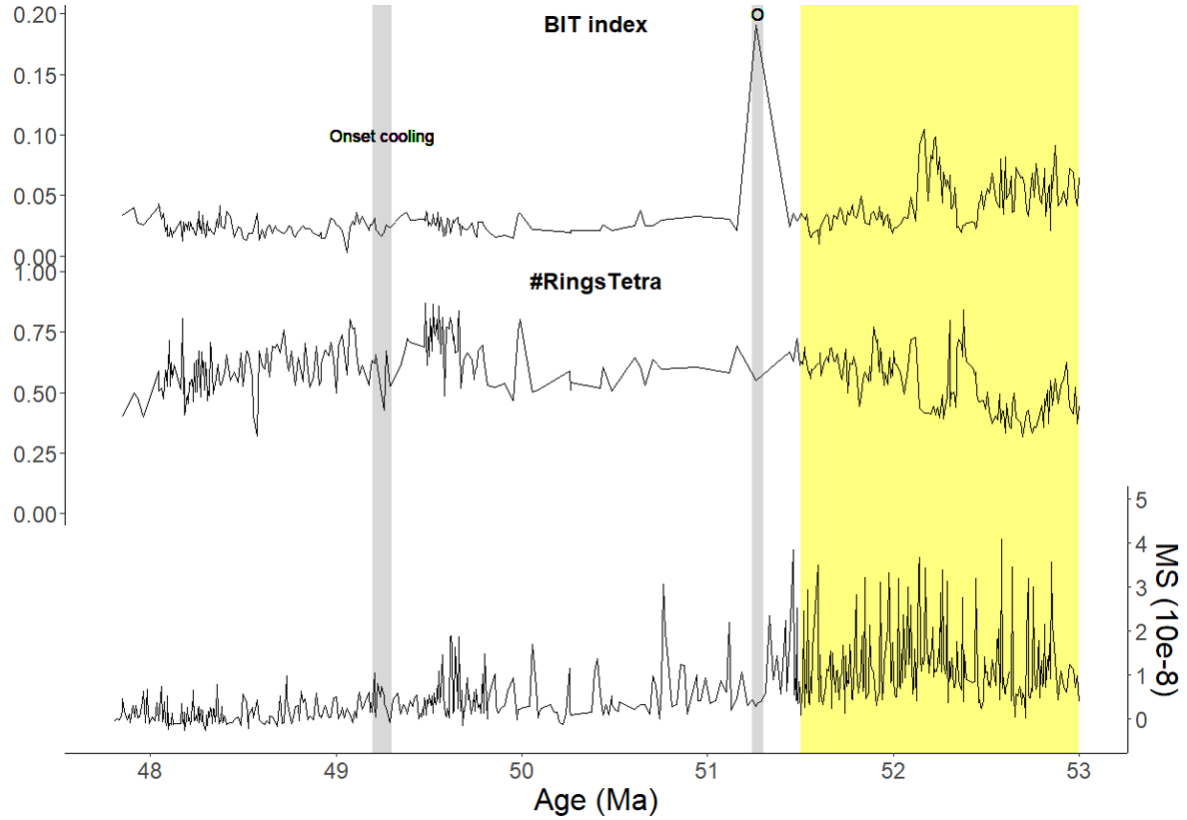

Figure 28. The BIT, #RingsTetra and bulk MS record versus age. Grey bars represent hyperthermal O and the age of the onset of the cooling as witnessed in the SST records. Orange shaded area represents the range of data from Fokkema et al. (2024; Chapter 6) (BIT and #RingsTetra) and Mannucci et al. (in prep) (MS).

5.4.2. Orbital forcing of the hydroclimate

The bulk MS, $\delta^{18}O$, and n-alkane proxy records reveal short-term cyclicities, indicating orbital forcing on the regional hydroclimate with various potential responses, including river discharge (as indicated by MS), salinity variations (reflected in $\delta^{18}O$), and changes in aridity (observed through n-alkanes). To test this, spectral analyses were run on these age tuned records.

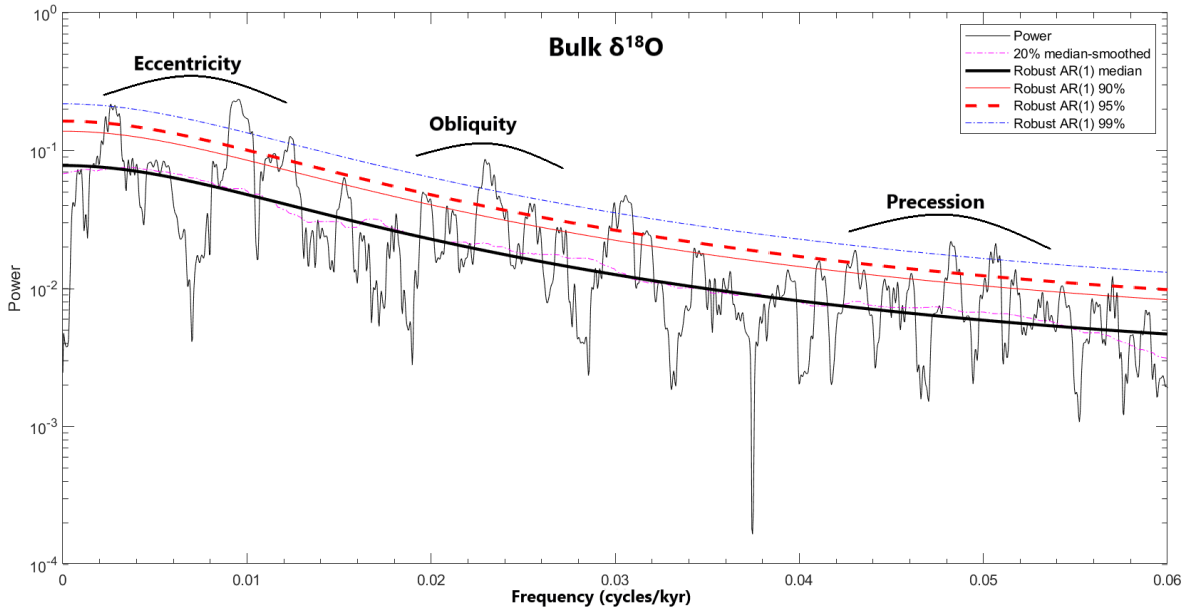

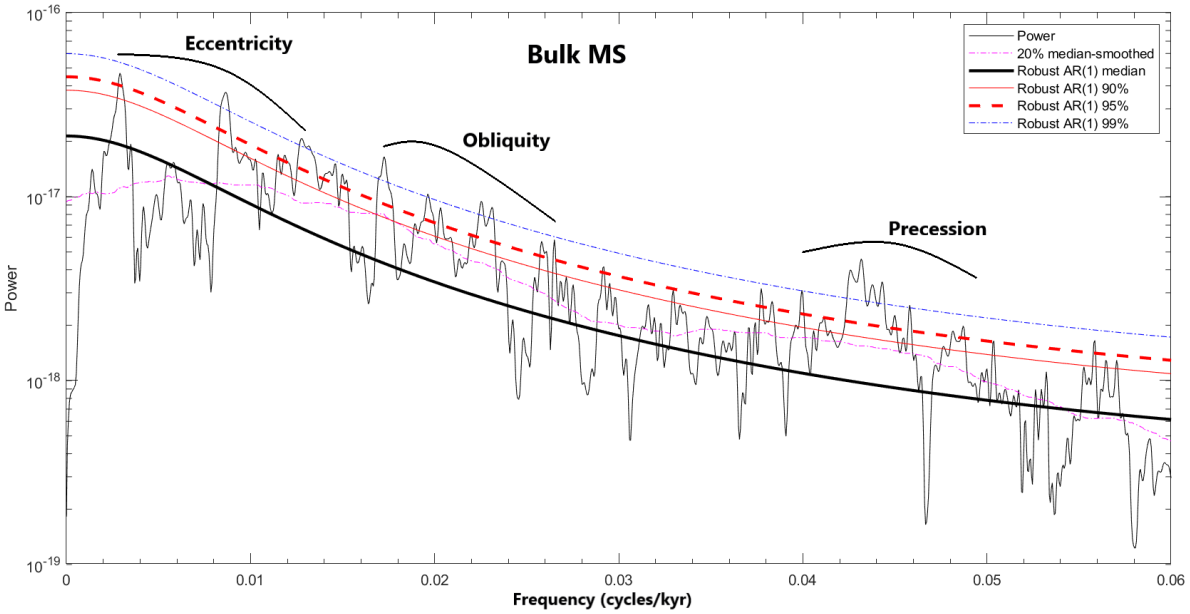
Bulk MS
Eccentricity
Obliquity
Precession
Power
20% median-smoothed
Robust AR(1) median
Robust AR(1) 90%
Robust AR(1) 95%
Robust AR(1) 99%
Power
Frequency (cycles/kyr)

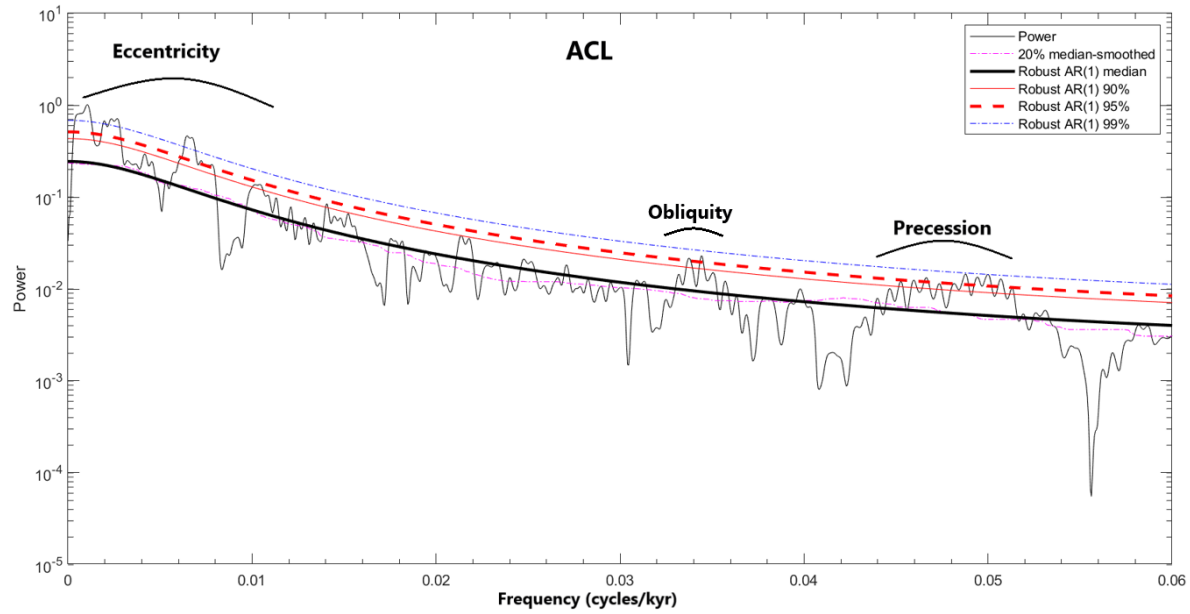
ACL
Eccentricity
Obliquity
Precession
Power
20% median-smoothed
Robust AR(1) median
Robust AR(1) 90%
Robust AR(1) 95%
Robust AR(1) 99%
Power
Frequency (cycles/kyr)

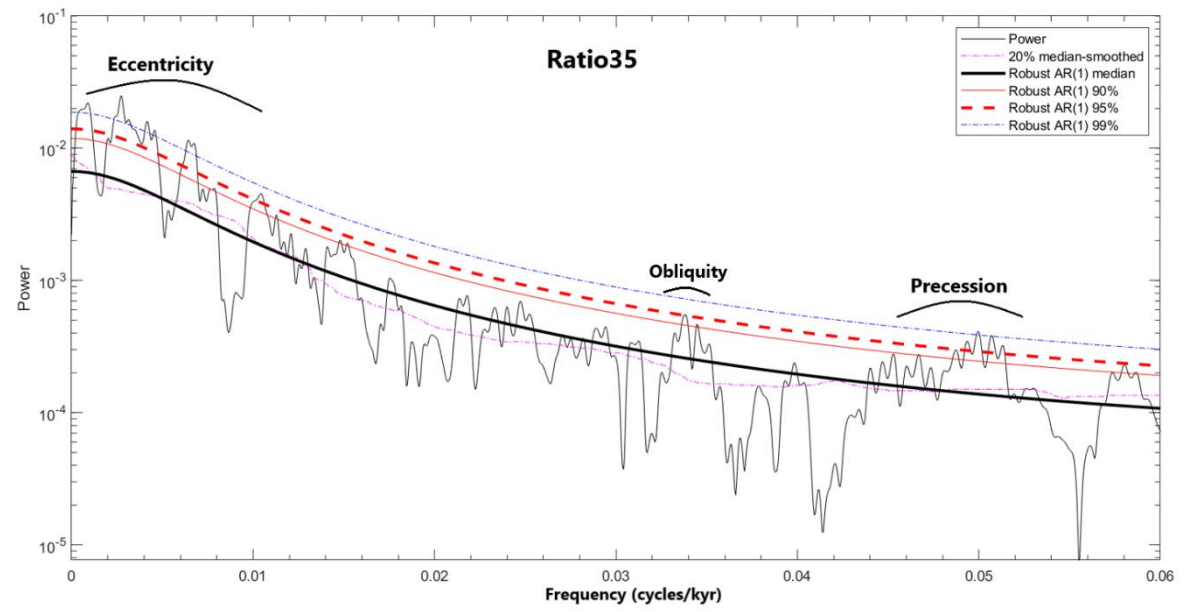
Ratio35
Eccentricity
Obliquity
Precession
Power
20% median-smoothed
Robust AR(1) median
Robust AR(1) 90%
Robust AR(1) 95%
Robust AR(1) 99%
Power
Frequency (cycles/kyr)

Figure 29. Spectral analyses of the bulk $\delta^{18}O$, MS, ACL and Ratio35 records versus age (51.5 – 47.8 Ma). Y-axis are in logarithmic scale. Frequencies are presented in cycles/kyr. 99%, 95% and 90% confidence bands of the robust autoregression (AR) test are depicted with the blue dotted, red dotted and red lines.

5.4.2.1. Precession and eccentricity forced hydrological variability

All records show the presence of a precession forcing (Fig. 29). For the bulk MS record this likely represents a precession driven variability in riverine input of paramagnetic clay minerals. However, MS values are also determined by dust input of clay minerals, which in turn depends on the amount of clay minerals sequestered in soils and riverbeds (Ehrmann et al., 2017). As North Africa aridifies after a humid period, wind-erosion of these terrestrially stored clay minerals is enhanced, increasing their atmospheric loading and subsequent deposition. Therefore it is suggested the intensity of the humid period is a predictor of the intensity of the dust blown into the sea in the succeeding arid period (Ehrmann et al., 2017). A more intense humid period causes more clay minerals to be stored and subsequently eroded.

Hence, there is likely an interplay between predominantly dust determined (during the more arid periods in precession maxima) and riverine determined (during the more humid periods in precession minima) MS peaks (section 5.4.1.1). This would imply the presence of a half-precession signal (~12 kyr) in the record, as the arid and humid periods are half a precession cycle apart (e.g. cf. Ulfers et al., 2022). However, the average data resolution (~8.8 kyr/sample) is too low to confidently detect half-precession signals with spectral analysis. Nonetheless, the bulk MS precession signal likely records a precession driven balance between clay minerals being primarily stored on land and eroded by rivers, and clay minerals being wind-eroded into the basin.

Considering this balance, and given that the magnitude of variability in the $\delta^{18}O$ and n-alkane records remains more or less consistent throughout the core, it is likely that the decrease in total clay mineral production, due to background aridification, caused the decline in amplitude of variability throughout the bulk MS record: precession-driven river discharge (i.e. precession minima) and wind erosion (i.e. precession maxima) transported fewer clay minerals into the basin, as the clay mineral pool became smaller due to overall decreased rock weathering rates (Eberl, 1984).

The precession signal for the n-alkane proxies should be interpreted a bit more carefully, as the data resolution for the two higher resolution intervals (Fig. 27) is roughly 3 samples/precession cycle. That being said, the precession signal could represent precession driven vegetation changes or, since most n-alkanes reach the basin through river inflow, precession driven changes in the river source of the n-alkanes. For example in more humid conditions during precession minima (Bosmans, Drijfhout, Tuenter, Hilgen, & Lourens, 2015), river water might originate from different latitudes, taking with it n-alkanes from a different source. Moreover, considering n-alkanes are also transported through dust, the signal could potentially represent a precession driven change in dust source. Given precession forces the latitudinal extent and location of convergence zones, it would naturally force a change in direction and strength of surface winds (Bosmans, Drijfhout, Tuenter, Hilgen, & Lourens, 2015), and with that a change in dust source area. While distinguishing between various source regions of n-alkanes is beyond the scope of this study, whether the signal reflects actual precession-driven vegetation changes or shifts in source areas, it underscores the role of precession in determining hydroclimate patterns, akin to the North African monsoon system (Bosmans, Drijfhout, Tuenter, Hilgen, & Lourens, 2015).

The bulk $\delta^{18}O$ record reflects variability in temperature and the $\delta^{18}O$ of the seawater ($\delta^{18}O_w$). $\delta^{18}O_w$ varies through the balance between evaporation and precipitation (i.e. Rayleigh fractionation), and therefore reflects salinity (and global ice volume, if present). Precession driven variability in solar insolation has an effect on both temperature and salinity (Bosmans, Drijfhout, Tuenter, Hilgen, & Lourens, 2015; Bosmans, Drijfhout, Tuenter, Hilgen, Lourens, et al., 2015). Considering hydroclimate variability is better understood in terms of salinity, it would be informative to decouple the temperature and salinity effect on $\delta^{18}O$ for this record. For example, clumped isotope based temperature reconstructions on single planktonic foraminifera can be used to decouple the temperature effect from

the $\delta^{18}O$ value of the foraminiferal calcite, to determine $\delta^{18}O_w$ and accordingly salinisation (Van Der Ploeg et al., 2023). This is however not possible for this study, as no measurements were done on single specimens. However, an estimation of $\delta^{18}O_w$ can be done by subtracting the temperature effect from the bulk $\delta^{18}O$ record with the TEX_{86} based SST reconstructions. For this, Equation 1 is used, whereby $\delta^{18}O_w$ is isolated using the TEX_{86} based SST and bulk $\delta^{18}O$ values. The resulting $\delta^{18}O_w$ record is shown in Figure 30. Spectral analysis on the higher resolution interval of 50 – 47.8 Ma, indeed reveals the presence of precession, obliquity and eccentricity forcing on salinity variability (Bosmans, Drijfhout, Tuenter, Hilgen, Lourens, et al., 2015).

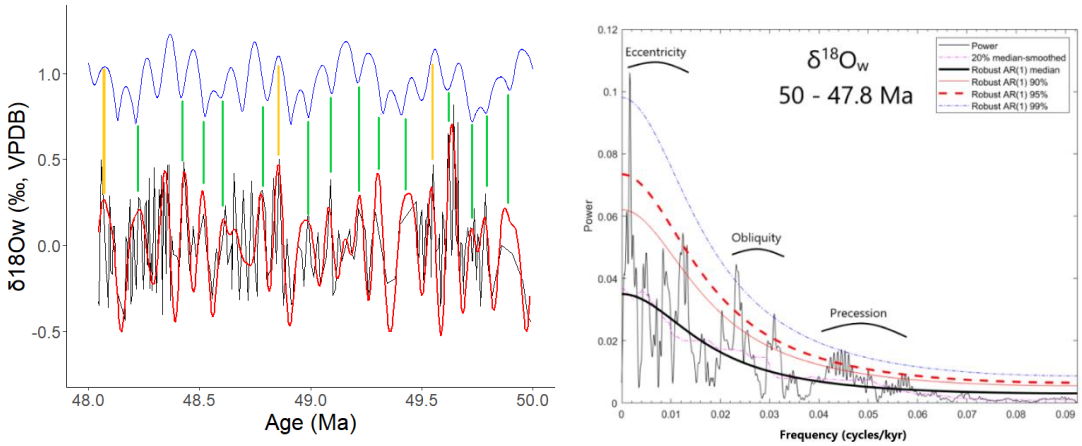

Figure 30. Left: The reconstructed $\delta^{18}O_w$ values through time, as determined using Eq. 1, the TEX_{86} based SST reconstructions and the bulk $\delta^{18}O$ record. The blue line represent the La2010b astronomical solution for eccentricity (not to scale), the red line the eccentricity filter of the $\delta^{18}O_w$ record, the orange lines represent filter maxima correlating with La2010b eccentricity maxima, and the green lines represent filter maxima correlating with eccentricity minima. Right: spectral analysis on the $\delta^{18}O_w$ record for the interval 50 – 47.8 Ma.

In most cases the $\delta^{18}O_w$ eccentricity filter maxima (minima) correlate with La2010b eccentricity minima (maxima) (Fig. 30), which is analogous to the recorded Mediterranean sapropel events (Hilgen, 1991; Larrasoaña et al., 2003). During eccentricity maxima the insolation seasonal contrasts are larger, amplifying summer convective rainfall through increased land-sea temperatures differences, and modulating the effect of precession (Braconnot et al., 2008). Therefore the correspondence between $\delta^{18}O_w$ minima with eccentricity maxima likely reflects the amplification of enhanced precipitation and river-runoff during precession minima, freshening the site. This modulation of the precession forcing by eccentricity is also reflected in the bulk MS record and spectral analysis (Fig. 29 and 31): amplitudes of the precession filter are increased over eccentricity filter maxima, and furthermore, eccentricity filter maxima generally correspond with maxima of the La2010b astronomical solution for eccentricity (Laskar et al., 2011), suggesting precession-forced clay mineral discharge (i.e. river discharge) is amplified during eccentricity maxima.

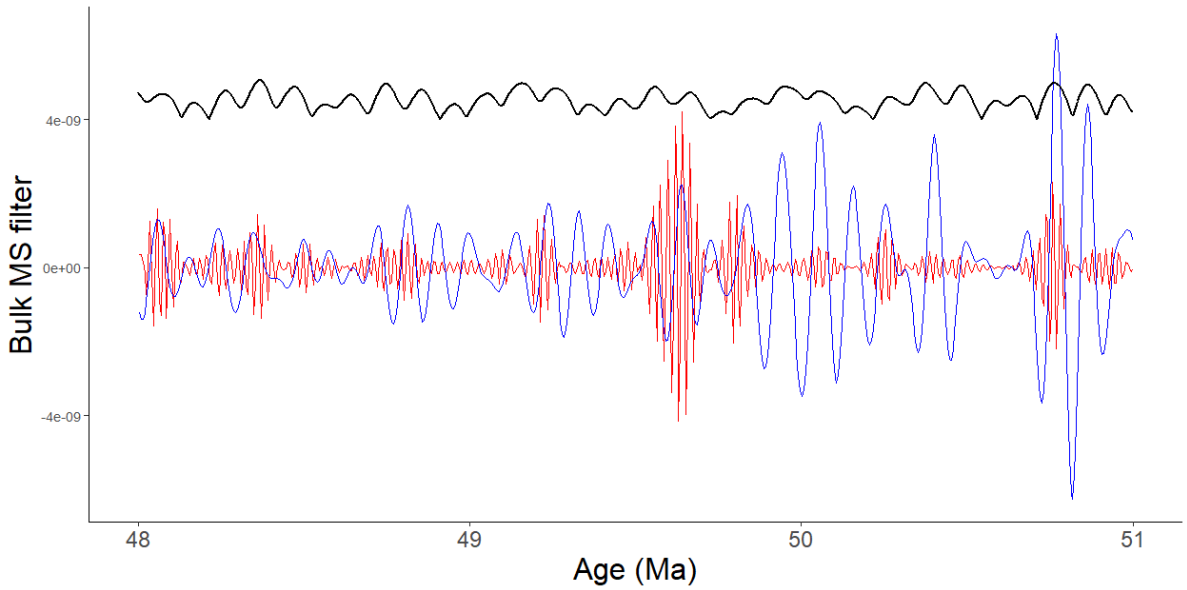

Figure 31. The precession (red) and short eccentricity (blue) filters of the bulk MS record (51 – 48 Ma). The black line represent the La2010b astronomical solution for eccentricity (not to scale). MS peaks generally correspond to eccentricity maxima.

5.4.2.2. Obliquity forced hydrological variability

Moreover, there is a robust presence of an obliquity signal in the MS, $\delta^{18}O_w$ and n-alkane proxy records. Interestingly, the n-alkane proxies record the obliquity signal with a shorter period (~30 kyr) than the bulk MS and $\delta^{18}O$ records (~42 kyr), suggestive of a different vegetational response to obliquity than river runoff. This could be attributed to the fact that obliquity forces both the summer inter-tropic insolation gradient (SITIG), and through that, the strength and latitudinal extent of winds and moisture transport in the summer hemisphere (Bosmans, Hilgen, Tuenter, & Lourens, 2015), as well as winter precipitation through increased winter air-sea temperature differences, resulting in more convective rainfall (Bosmans, Drijfhout, Tuenter, Hilgen, Lourens, et al., 2015). The first could lead to more precipitation extremes, affecting primarily river runoff (i.e. MS and $\delta^{18}O_w$), and the latter results in an overall yearlong wetter climate, affecting aridity and with that potentially vegetation changes (i.e. n-alkanes). Further research, integrating model simulations with high-resolution paleoclimate records, is needed to fully understand the complex responses of different proxies to obliquity-driven North African climate variability.

5.4.3. The hydroclimate of the early middle Eocene southern Tethys

Overall, the southern Tethys background climate likely aridified from the PETM onwards and throughout the EECO, as evident from the bulk MS and brGDGT record (cf. Fokkema et al., 2024; Chapter 6). Which is in line with the 'dry-gets-drier' principle (Held & Soden, 2006). There is no clear evidence of a long term change in hydroclimate over the onset of the cooling. Perhaps the dynamical component of time mean moisture divergence (i.e. changes in circulation strength) outweighed the thermodynamical component (i.e. changes in humidity) due to polar amplification. The potential rise in LTGs as the global climate cooled (Cramwinckel et al., 2018; Fokkema et al., 2023) possibly intensified Hadley cell circulation, whilst humidity did not increase accordingly. This could have inhibited overall humidification during the systematic cooling, mechanistically similar, but opposite, to the hydroclimate response to temperature increase in the Horn of Africa during the early Holocene (Baxter et al., 2023). Obviously, more research is needed to validate this idea.

Climate model simulations of present-day and Eocene North Africa show the regional hydrology to be largely determined by changes in the North African monsoon system (Bosmans, Drijfhout, Tuenter, Hilgen, & Lourens, 2015; Bosmans, Drijfhout, Tuenter, Hilgen, Lourens, et al., 2015; Huber & Goldner, 2012; Williams et al., 2022). All proxies considered, there are multiple lines of evidence suggesting the

monsoon operated according to the same orbital mechanisms during the early (to middle) Eocene. The eccentricity modulated precession forcing of river discharge, as indicated by the MS record, is well in line with the observed salinity variability, as recorded by the $\delta^{18}O_w$ record. This is further validated by the correspondence of MS maxima and $\delta^{18}O_w$ minima with eccentricity maxima of the La2010b astronomical solution. Additionally, lower-resolution evidence from the n-alkane record suggests precession and obliquity forced vegetation and aridity changes. These findings collectively indicate similarities in the orbital behaviour of the North African monsoon between the early Eocene and Miocene to Holocene epochs, as recorded in the Mediterranean sapropels (~13.5 Ma to ~9 ka) (e.g. Hilgen, 1991; Larrasoaña et al., 2003; Rohling et al., 2015). Lastly, it seems short term changes in the early Eocene hydroclimate were more determined by the orbital forcing of monsoon dynamics than transient global climatic events, such as the EECO hyperthermals.

6. Conclusion

In conclusion, we produced the highest-resolution early middle Eocene SST record for the southern Tethys, which shows a systematic cooling around 49.2 Ma of ~1 °C, concurring with the cooling witnessed in high latitudes and the deep sea. This suggests changes in global greenhouse gas concentrations were likely an important driver for this globally occurring cooling event. Furthermore, almost all CIE associated hyperthermals previously found in deep sea records occur consistently in the RH-323 record, which emphasises the global scale associated with these carbon cycle perturbations as represented by the CIEs.

Throughout the EECO, the area around the southern Tethys likely aridified into overall arid conditions, similar to today. However, there is no detectable hydrological change over the onset of the cooling, which suggests the cooling was not a driver enough to cause a phase shift towards a wetter climate. Furthermore, the proxies record precession and obliquity forced river discharge, salinisation and vegetational changes, akin to the orbital operation of the North African monsoon. Therefore, the North African monsoon seems to be a robust feature of Cenozoic Earth.

Future research should focus on the development of more high-resolution SST records, for other low latitude sites, to get a better understanding of zonal variation, but also for mid- and high-latitude sites, to better constrain the timing of the onset of Cenozoic cooling. This could elucidate the mechanism behind the interaction between the global CO_2 drawdown and the onset of systematic cooling. For example, perhaps a combination of the various orogenic and *Azolla* events occurring around ~50 Ma caused a series of cooling pulses, which could have eventually triggered the onset of Cenozoic cooling as a phase shift to an alternative climatic stable state. The comparison of different high-resolution records is needed to get a better understanding of this. Considering hydrological changes, data from different proxy types are needed to get a more detailed understanding of hydrological changes associated with this cooling event. A pollen based paleoenvironmental reconstruction can give a more nuanced picture of vegetation (and aridity) changes, and a hydrogen isotope record could give a better understanding of changes in overall precipitation. Moreover, a $\delta^{18}O_w$ record from decoupled single specimen SST-$\delta^{18}O$ reconstructions could give further insights into salinity/aridity changes.

7. References

1. Adar, E.M., Nativ, R., Siman-Tov, R., and Eshet, Y., 1999, The deep corehole (RH-323) in Ramat Hovav. Final report submitted to the Israeli Water Authority.: Geological Survey Israel, v. 6.
2. Anagnostou, E., John, E. H., Babila, T. L., Sexton, P. F., Ridgwell, A., Lunt, D. J., Pearson, P. N., Chalk, T. B., Pancost, R. D., & Foster, G. L. (2020). Proxy evidence for state-dependence of climate sensitivity in the Eocene greenhouse. Nature Communications, 11(1), 4436. https://doi.org/10.1038/s41467-020-17887-x
3. Anagnostou, E., John, E. H., Edgar, K. M., Foster, G. L., Ridgwell, A., Inglis, G. N., Pancost, R. D., Lunt, D. J., & Pearson, P. N. (2016). Changing atmospheric CO2 concentration was the primary driver of early Cenozoic climate. Nature, 533(7603), 380-384. https://doi.org/10.1038/nature17423
4. Barke, J., Van Der Burgh, J., Van Konijnenburg-van Cittert, J. H. A., Collinson, M. E., Pearce, M. A., Bujak, J., Heilmann-Clausen, C., Speelman, E. N., Van Kempen, M. M. L., Reichart, G.-J., Lotter, A. F., & Brinkhuis, H. (2012). Coeval Eocene blooms of the freshwater fern Azolla in and around Arctic and Nordic seas. Palaeogeography, Palaeoclimatology, Palaeoecology, 337-338, 108-119. https://doi.org/10.1016/j.palaeo.2012.04.002
5. Baxter, A. J., Verschuren, D., Peterse, F., Miralles, D. G., Martin-Jones, C. M., Maitituerdi, A., Van Der Meeren, T., Van Daele, M., Lane, C. S., Haug, G. H., Olago, D. O., & Sinninghe Damsté, J. S. (2023). Reversed Holocene temperature–moisture relationship in the Horn of Africa. Nature, 620(7973), 336-343. https://doi.org/10.1038/s41586-023-06272-5
6. Bijl, P. K., Bendle, J. A. P., Bohaty, S. M., Pross, J., Schouten, S., Tauxe, L., Stickley, C. E., McKay, R. M., Röhl, U., Olney, M., Sluijs, A., Escutia, C., Brinkhuis, H., Expedition 318 Scientists, Klaus, A., Fehr, A., Williams, T., Carr, S. A., Dunbar, R. B., … Yamane, M. (2013). Eocene cooling linked to early flow across the Tasmanian Gateway. Proceedings of the National Academy of Sciences, 110(24), 9645-9650. https://doi.org/10.1073/pnas.1220872110
7. Bijl, P. K., Frieling, J., Cramwinckel, M. J., Boschman, C., Sluijs, A., & Peterse, F. (2021). Maastrichtian–Rupelian paleoclimates in the southwest Pacific – a critical re-evaluation of biomarker paleothermometry and dinoflagellate cyst paleoecology at Ocean Drilling Program Site 1172. Climate of the Past, 17(6), 2393-2425. https://doi.org/10.5194/cp-17-2393-2021
8. Bijl, P. K., Houben, A. J. P., Schouten, S., Bohaty, S. M., Sluijs, A., Reichart, G.-J., Sinninghe Damsté, J. S., & Brinkhuis, H. (2010). Transient Middle Eocene Atmospheric CO 2 and Temperature Variations. Science, 330(6005), 819-821. https://doi.org/10.1126/science.1193654
9. Blaga, C. I., Reichart, G.-J., Heiri, O., & Sinninghe Damsté, J. S. (2009). Tetraether membrane lipid distributions in water-column particulate matter and sediments: A study of 47 European lakes along a north–south transect. Journal of Paleolimnology, 41(3), 523-540. https://doi.org/10.1007/s10933-008-9242-2
10. Bliedtner, M., Schäfer, I. K., Zech, R., & Von Suchodoletz, H. (2018). Leaf wax <i>n</i>-alkanes in modern plants and topsoils from eastern Georgia (Caucasus) – implications for reconstructing regional paleovegetation. Biogeosciences, 15(12), 3927-3936. https://doi.org/10.5194/bg-15-3927-2018
11. Bosmans, J. H. C., Drijfhout, S. S., Tuenter, E., Hilgen, F. J., & Lourens, L. J. (2015). Response of the North African summer monsoon to precession and obliquity forcings in the EC-Earth GCM. Climate Dynamics, 44(1-2), 279-297. https://doi.org/10.1007/s00382-014-2260-z
12. Bosmans, J. H. C., Drijfhout, S. S., Tuenter, E., Hilgen, F. J., Lourens, L. J., & Rohling, E. J. (2015). Precession and obliquity forcing of the freshwater budget over the Mediterranean. Quaternary Science Reviews, 123, 16-30. https://doi.org/10.1016/j.quascirev.2015.06.008
13. Bosmans, J. H. C., Hilgen, F. J., Tuenter, E., & Lourens, L. J. (2015). Obliquity forcing of low-latitude climate. Climate of the Past, 11(10), 1335-1346. https://doi.org/10.5194/cp-11-1335-2015
14. Bouligand, C., Dyment, J., Gallet, Y., & Hulot, G. (2006). Geomagnetic field variations between chrons 33r and 19r (83–41 Ma) from sea-surface magnetic anomaly profiles. Earth and Planetary Science Letters, 250(3-4), 541-560. https://doi.org/10.1016/j.epsl.2006.06.051
15. Braconnot, P., Marzin, C., Gregoire, L., Mosquet, E., & Marti, O. (2008). Monsoon response to changes in Earth's orbital parameters: Comparisons between simulations of the Eemian and of the Holocene. Clim. Past.
16. Brinkhuis, H., the Expedition 302 Scientists, Schouten, S., Collinson, M. E., Sluijs, A., Damsté, J. S. S., Dickens, G. R., Huber, M., Cronin, T. M., Onodera, J., Takahashi, K., Bujak, J. P., Stein, R., Van Der Burgh, J., Eldrett, J. S., Harding, I. C., Lotter, A. F., Sangiorgi, F., Cittert, H. V. K., … Moran, K. (2006). Episodic fresh surface waters in the Eocene Arctic Ocean. Nature, 441(7093), 606-609. https://doi.org/10.1038/nature04692
17. Burls, N. J., & Fedorov, A. V. (2017). Wetter subtropics in a warmer world: Contrasting past and future hydrological cycles. Proceedings of the National Academy of Sciences, 114(49), 12888-12893. https://doi.org/10.1073/pnas.1703421114
18. Bush, R. T., & McInerney, F. A. (2013). Leaf wax n-alkane distributions in and across modern plants: Implications for paleoecology and chemotaxonomy. Geochimica et Cosmochimica Acta, 117, 161-179. https://doi.org/10.1016/j.gca.2013.04.016
19. Carmichael, M. J., Inglis, G. N., Badger, M. P. S., Naafs, B. D. A., Behrooz, L., Remmelzwaal, S., Monteiro, F. M., Rohrssen, M., Farnsworth, A., Buss, H. L., Dickson, A. J., Valdes, P. J., Lunt, D. J., & Pancost, R. D. (2017).

Hydrological and associated biogeochemical consequences of rapid global warming during the Paleocene-Eocene Thermal Maximum. Global and Planetary Change, 157, 114-138. https://doi.org/10.1016/j.gloplacha.2017.07.014
20. Carr, A. S., Boom, A., Grimes, H. L., Chase, B. M., Meadows, M. E., & Harris, A. (2014). Leaf wax n-alkane distributions in arid zone South African flora: Environmental controls, chemotaxonomy and palaeoecological implications. Organic Geochemistry, 67, 72-84. https://doi.org/10.1016/j.orggeochem.2013.12.004
21. Castañeda, I. S., Schouten, S., Pätzold, J., Lucassen, F., Kasemann, S., Kuhlmann, H., & Schefuß, E. (2016). Hydroclimate variability in the Nile River Basin during the past 28,000 years. Earth and Planetary Science Letters, 438, 47-56. https://doi.org/10.1016/j.epsl.2015.12.014
22. Cramwinckel, M. J., Burls, N. J., Fahad, A. A., Knapp, S., West, C. K., Reichgelt, T., Tindall, J. C., Huber, M., Sluijs, A., Trabucho-Alexandre, J., Belopolsky, A. V., Sewall, J. O., Eldrett, J. S., Legarda-Lisarri, A., Batenburg, S. J., Huck, C. E., Littler, K., Zachos, J. C., & Inglis, G. N. (2023). Global and zonal-mean hydrological response to early Eocene warmth. Paleoceanography and Paleoclimatology, 38(6), e2022PA004542. https://doi.org/10.1029/2022PA004542
23. Cramwinckel, M. J., Huber, M., Kocken, I. J., Agnini, C., Bijl, P. K., Bohaty, S. M., Frieling, J., Goldner, A., Hilgen, F. J., Kip, E. L., Peterse, F., Van Der Ploeg, R., Röhl, U., Schouten, S., & Sluijs, A. (2018). Synchronous tropical and polar temperature evolution in the Eocene. Nature, 559(7714), 382-386. https://doi.org/10.1038/s41586-018-0272-2
24. Crouch, E. M., Shepherd, C. L., Morgans, H. E. G., Naafs, B. D. A., Dallanave, E., Phillips, A., Hollis, C. J., & Pancost, R. D. (2020). Climatic and environmental changes across the early Eocene climatic optimum at mid-Waipara River, Canterbury Basin, New Zealand. Earth-Science Reviews, 200, 102961. https://doi.org/10.1016/j.earscirev.2019.102961
25. De Jonge, C., Hopmans, E. C., Zell, C. I., Kim, J.-H., Schouten, S., & Sinninghe Damsté, J. S. (2014). Occurrence and abundance of 6-methyl branched glycerol dialkyl glycerol tetraethers in soils: Implications for palaeoclimate reconstruction. Geochimica et Cosmochimica Acta, 141, 97-112. https://doi.org/10.1016/j.gca.2014.06.013
26. De Jonge, C., Stadnitskaia, A., Hopmans, E. C., Cherkashov, G., Fedotov, A., & Sinninghe Damsté, J. S. (2014). In situ produced branched glycerol dialkyl glycerol tetraethers in suspended particulate matter from the Yenisei River, Eastern Siberia. Geochimica et Cosmochimica Acta, 125, 476-491. https://doi.org/10.1016/j.gca.2013.10.031
27. Dearing Crampton-Flood, E., Van Der Weijst, C. M. H., Van Der Molen, G., Bouquet, M., Yedema, Y., Donders, T. H., Sangiorgi, F., Sluijs, A., Sinninghe Damsté, J. S., & Peterse, F. (2021). Identifying marine and freshwater overprints on soil-derived branched GDGT temperature signals in Pliocene Mississippi and Amazon River fan sediments. Organic Geochemistry, 154, 104200. https://doi.org/10.1016/j.orggeochem.2021.104200
28. Eberl, D. D. (1984). Clay mineral formation and transformation in rocks and soils. Philosophical Transactions of the Royal Society of London. Series A, Mathematical and Physical Sciences, 311(1517), 241-257.
29. Eberle, J. J., & Greenwood, D. R. (2012). Life at the top of the greenhouse Eocene world—A review of the Eocene flora and vertebrate fauna from Canada's High Arctic. Geological Society of America Bulletin, 124(1-2), 3-23. https://doi.org/10.1130/B30571.1
30. Ehrmann, W., Schmiedl, G., Beuscher, S., & Krüger, S. (2017). Intensity of African Humid Periods Estimated from Saharan Dust Fluxes. PLOS ONE, 12(1), e0170989. https://doi.org/10.1371/journal.pone.0170989
31. Fokkema, C. D., Kelly, L., Mannucci, A., Theijse, B., Agterhuis, T., Brinkhuis, H., Agnini, C., Bialik, O. M., Waldmann, N., Dickens, G. R., Galeotti, S., Peterse, F., & Sluijs, A. (2024). Chapter 6: Trends, rhythms, and aberrations in late Paleocene – early Eocene (hydro)climate in the northern African arid zone. In C. D. Fokkema (Ed.), PhD Thesis, submitted. Utrecht University.
32. Fokkema, C. D., Agterhuis, T., Gerritsma, D., De Goeij, M., Liu, X., De Regt, P., Rice, A., Vennema, L., Agnini, C., Bijl, P. K., Frieling, J., Huber, M., Peterse, F., & Sluijs, A. (2023). Polar amplification of orbital-scale climate variability in the early Eocene greenhouse world [Preprint]. Feedback and Forcing/Marine Archives/Cenozoic. https://doi.org/10.5194/cp-2023-70
33. Fokkema, C. D., Buijs, S., Bialik, O. M., Meilijson, A., Waldmann, N. D., Makovsky, Y., Frieling, J., Dickens, G. R., & Sluijs, A. (2022). Late Paleocene to middle Eocene carbon isotope stratigraphy of the Northern Negev, Southern Israel: Potential for paleoclimate reconstructions. Newsletters on Stratigraphy, 55(3), 361-384. https://doi.org/10.1127/nos/2022/0684
34. Foucault, A., & Mélières, F. (2000). Palaeoclimatic cyclicity in central Mediterranean Pliocene sediments: The mineralogical signal. Palaeogeography, Palaeoclimatology, Palaeoecology, 158(3-4), 311-323. https://doi.org/10.1016/S0031-0182(00)00056-0
35. Geen, R., Bordoni, S., Battisti, D. S., & Hui, K. (2020). Monsoons, ITCZs, and the Concept of the Global Monsoon. Reviews of Geophysics, 58(4), e2020RG000700. https://doi.org/10.1029/2020RG000700
36. Grant, K. M., Amarathunga, U., Amies, J. D., Hu, P., Qian, Y., Penny, T., Rodriguez-Sanz, L., Zhao, X., Heslop, D., Liebrand, D., Hennekam, R., Westerhold, T., Gilmore, S., Lourens, L. J., Roberts, A. P., & Rohling, E. J. (2022). Organic carbon burial in Mediterranean sapropels intensified during Green Sahara Periods since 3.2 Myr ago. Communications Earth & Environment, 3(1), 11. https://doi.org/10.1038/s43247-021-00339-9
37. Guo, J., Glendell, M., Meersmans, J., Kirkels, F., Middelburg, J. J., & Peterse, F. (2020). Assessing branched tetraether lipids as tracers of soil organic carbon transport through the Carminowe Creek catchment (southwest England). Biogeosciences, 17(12), 3183-3201. https://doi.org/10.5194/bg-17-3183-2020

38. Handley, L., O'Halloran, A., Pearson, P. N., Hawkins, E., Nicholas, C. J., Schouten, S., McMillan, I. K., & Pancost, R. D. (2012). Changes in the hydrological cycle in tropical East Africa during the Paleocene–Eocene Thermal Maximum. Palaeogeography, Palaeoclimatology, Palaeoecology, 329-330, 10-21. https://doi.org/10.1016/j.palaeo.2012.02.002
39. Harper, D. T., Hönisch, B., Zeebe, R. E., Shaffer, G., Haynes, L. L., Thomas, E., & Zachos, J. C. (2020). The Magnitude of Surface Ocean Acidification and Carbon Release During Eocene Thermal Maximum 2 (ETM-2) and the Paleocene-Eocene Thermal Maximum (PETM). Paleoceanography and Paleoclimatology, 35(2). https://doi.org/10.1029/2019PA003699
40. Held, I. M., & Soden, B. J. (2006). Robust Responses of the Hydrological Cycle to Global Warming. Journal of Climate, 19(21), 5686-5699. https://doi.org/10.1175/JCLI3990.1
41. Hemingway, J. D., Schefuß, E., Dinga, B. J., Pryer, H., & Galy, V. V. (2016). Multiple plant-wax compounds record differential sources and ecosystem structure in large river catchments. Geochimica et Cosmochimica Acta, 184, 20-40. https://doi.org/10.1016/j.gca.2016.04.003
42. Hernández-Sánchez, M. T., Woodward, E. M. S., Taylor, K. W. R., Henderson, G. M., & Pancost, R. D. (2014). Variations in GDGT distributions through the water column in the South East Atlantic Ocean. Geochimica et Cosmochimica Acta, 132, 337-348. https://doi.org/10.1016/j.gca.2014.02.009
43. Herold, N., Buzan, J., Seton, M., Goldner, A., Green, J. A. M., Müller, R. D., Markwick, P., & Huber, M. (2014). A suite of early Eocene (~ 55 Ma) climate model boundary conditions. Geoscientific Model Development, 7(5), 2077-2090. https://doi.org/10.5194/gmd-7-2077-2014
44. Hilgen, F. J. (1991). Astronomical calibration of Gauss to Matuyama sapropels in the Mediterranean and implication for the Geomagnetic Polarity Time Scale. Earth and Planetary Science Letters, 104(2-4), 226-244. https://doi.org/10.1016/0012-821X(91)90206-W
45. Hopmans, E. C., Schouten, S., & Sinninghe Damsté, J. S. (2016). The effect of improved chromatography on GDGT-based palaeoproxies. Organic Geochemistry, 93, 1-6. https://doi.org/10.1016/j.orggeochem.2015.12.006
46. Hopmans, E. C., Weijers, J. W. H., Schefuß, E., Herfort, L., Sinninghe Damsté, J. S., & Schouten, S. (2004). A novel proxy for terrestrial organic matter in sediments based on branched and isoprenoid tetraether lipids. Earth and Planetary Science Letters, 224(1-2), 107-116. https://doi.org/10.1016/j.epsl.2004.05.012
47. Huber, M., & Goldner, A. (2012). Eocene monsoons. Journal of Asian Earth Sciences, 44, 3-23. https://doi.org/10.1016/j.jseaes.2011.09.014
48. Hurley, S. J., Lipp, J. S., Close, H. G., Hinrichs, K.-U., & Pearson, A. (2018). Distribution and export of isoprenoid tetraether lipids in suspended particulate matter from the water column of the Western Atlantic Ocean. Organic Geochemistry, 116, 90-102. https://doi.org/10.1016/j.orggeochem.2017.11.010
49. Inglis, G. N., Bragg, F., Burls, N. J., Cramwinckel, M. J., Evans, D., Foster, G. L., Huber, M., Lunt, D. J., Siler, N., Steinig, S., Tierney, J. E., Wilkinson, R., Anagnostou, E., De Boer, A. M., Dunkley Jones, T., Edgar, K. M., Hollis, C. J., Hutchinson, D. K., & Pancost, R. D. (2020). Global mean surface temperature and climate sensitivity of the early Eocene Climatic Optimum (EECO), Paleocene–Eocene Thermal Maximum (PETM), and latest Paleocene. Climate of the Past, 16(5), 1953-1968. https://doi.org/10.5194/cp-16-1953-2020
50. Inglis, G. N., Farnsworth, A., Lunt, D., Foster, G. L., Hollis, C. J., Pagani, M., Jardine, P. E., Pearson, P. N., Markwick, P., Galsworthy, A. M. J., Raynham, L., Taylor, Kyle. W. R., & Pancost, R. D. (2015). Descent toward the Icehouse: Eocene sea surface cooling inferred from GDGT distributions: DESCENT TOWARD THE ICEHOUSE. Paleoceanography, 30(7), 1000-1020. https://doi.org/10.1002/2014PA002723
51. Kim, J.-H., Van Der Meer, J., Schouten, S., Helmke, P., Willmott, V., Sangiorgi, F., Koç, N., Hopmans, E. C., & Damsté, J. S. S. (2010). New indices and calibrations derived from the distribution of crenarchaeal isoprenoid tetraether lipids: Implications for past sea surface temperature reconstructions. Geochimica et Cosmochimica Acta, 74(16), 4639-4654. https://doi.org/10.1016/j.gca.2010.05.027
52. Kirtland Turner, S., Sexton, P. F., Charles, C. D., & Norris, R. D. (2014). Persistence of carbon release events through the peak of early Eocene global warmth. Nature Geoscience, 7(10), 748-751. https://doi.org/10.1038/ngeo2240
53. Larrasoaña, J. C., Roberts, A. P., & Rohling, E. J. (2008). Magnetic susceptibility of eastern Mediterranean marine sediments as a proxy for Saharan dust supply? Marine Geology, 254(3-4), 224-229. https://doi.org/10.1016/j.margeo.2008.06.003
54. Laskar, J., Fienga, A., Gastineau, M., & Manche, H. (2011). La2010: A new orbital solution for the long-term motion of the Earth. Astronomy & Astrophysics, 532, A89.
55. Larrasoaña, J. C., Roberts, A. P., & Rohling, E. J. (2013). Dynamics of Green Sahara Periods and Their Role in Hominin Evolution. PLoS ONE, 8(10), e76514. https://doi.org/10.1371/journal.pone.0076514
56. Larrasoaña, J. C., Roberts, A. P., Rohling, E. J., Winklhofer, M., & Wehausen, R. (2003). Three million years of monsoon variability over the northern Sahara. Climate Dynamics, 21(7-8), 689-698. https://doi.org/10.1007/s00382-003-0355-z
57. Lauretano, V., Hilgen, F. J., Zachos, J. C., & Lourens, L. J. (2016). Astronomically tuned age model for the early Eocene carbon isotope events: A new high-resolution δ13 Cbenthic record of ODP Site 1263 between ~ 49 and ~ 54 Ma. Newsletters on Stratigraphy, 49(2), 383-400. https://doi.org/10.1127/nos/2016/0077

58. Lazarus, D., Bittniok, B., Diester-Haass, L., Meyers, P., & Billups, K. (2006). Comparison of radiolarian and sedimentologic paleoproductivity proxies in the latest Miocene–Recent Benguela Upwelling System. Marine Micropaleontology, 60(4), 269-294. https://doi.org/10.1016/j.marmicro.2006.06.003
59. Lengger, S. K., Kraaij, M., Tjallingii, R., Baas, M., Stuut, J.-B., Hopmans, E. C., Sinninghe Damsté, J. S., & Schouten, S. (2013). Differential degradation of intact polar and core glycerol dialkyl glycerol tetraether lipids upon post-depositional oxidation. Organic Geochemistry, 65, 83-93. https://doi.org/10.1016/j.orggeochem.2013.10.004
60. Li, M., Hinnov, L., & Kump, L. (2019). Acycle: Time-series analysis software for paleoclimate research and education. Computers & Geosciences, 127, 12-22. https://doi.org/10.1016/j.cageo.2019.02.011
61. Licht, A., Van Cappelle, M., Abels, H. A., Ladant, J.-B., Trabucho-Alexandre, J., France-Lanord, C., Donnadieu, Y., Vandenberghe, J., Rigaudier, T., Lécuyer, C., Terry Jr, D., Adriaens, R., Boura, A., Guo, Z., Soe, A. N., Quade, J., Dupont-Nivet, G., & Jaeger, J.-J. (2014). Asian monsoons in a late Eocene greenhouse world. Nature, 513(7519), 501-506. https://doi.org/10.1038/nature13704
62. Liu, Q., Larrasoaña, J. C., Torrent, J., Roberts, A. P., Rohling, E. J., Liu, Z., & Jiang, Z. (2012). New constraints on climate forcing and variability in the circum-Mediterranean region from magnetic and geochemical observations of sapropels S1, S5 and S6. Palaeogeography, Palaeoclimatology, Palaeoecology, 333-334, 1-12. https://doi.org/10.1016/j.palaeo.2012.02.036
63. Lourens, L. J., Sluijs, A., Kroon, D., Zachos, J. C., Thomas, E., Röhl, U., Bowles, J., & Raffi, I. (2005). Astronomical pacing of late Palaeocene to early Eocene global warming events. Nature, 435(7045), 1083-1087. https://doi.org/10.1038/nature03814
64. Lourens, L. J., & Tuenter, E. (2009). The Role of Variations of the Earth's Orbital Characteristics in Climate Change. In Climate Change (pp. 103-123). Elsevier. https://doi.org/10.1016/B978-0-444-53301-2.00005-1
65. Lunt, D. J., Bragg, F., Chan, W.-L., Hutchinson, D. K., Ladant, J.-B., Morozova, P., Niezgodzki, I., Steinig, S., Zhang, Z., Zhu, J., Abe-Ouchi, A., Anagnostou, E., De Boer, A. M., Coxall, H. K., Donnadieu, Y., Foster, G., Inglis, G. N., Knorr, G., Langebroek, P. M., … Otto-Bliesner, B. L. (2021). DeepMIP: Model intercomparison of early Eocene climatic optimum (EECO) large-scale climate features and comparison with proxy data. Climate of the Past, 17(1), 203-227. https://doi.org/10.5194/cp-17-203-2021
66. Lunt, D. J., Dunkley Jones, T., Heinemann, M., Huber, M., LeGrande, A., Winguth, A., Loptson, C., Marotzke, J., Roberts, C. D., Tindall, J., Valdes, P., & Winguth, C. (2012). A model–data comparison for a multi-model ensemble of early Eocene atmosphere–ocean simulations: EoMIP. Climate of the Past, 8(5), 1717-1736. https://doi.org/10.5194/cp-8-1717-2012
67. Maffione, M., Speranza, F., Faccenna, C., & Rossello, E. (2010). Paleomagnetic evidence for a pre-early Eocene (~50Ma) bending of the Patagonian orocline (Tierra del Fuego, Argentina): Paleogeographic and tectonic implications. Earth and Planetary Science Letters, 289(1-2), 273-286. https://doi.org/10.1016/j.epsl.2009.11.015
68. Misra, S., & Froelich, P. N. (2012). Lithium Isotope History of Cenozoic Seawater: Changes in Silicate Weathering and Reverse Weathering. Science, 335(6070), 818-823. https://doi.org/10.1126/science.1214697
69. Molnar, P., England, P., & Martinod, J. (1993). Mantle dynamics, uplift of the Tibetan Plateau, and the Indian Monsoon. Reviews of Geophysics, 31(4), 357-396. https://doi.org/10.1029/93RG02030
70. Monerie, P. A., Roucou, P., & Fontaine, B. (2013). Mid-century effects of Climate Change on African monsoon dynamics using the A1B emission scenario. International Journal of Climatology, 33(4), 881-896.
71. Parés, J. M. (2015). Sixty years of anisotropy of magnetic susceptibility in deformed sedimentary rocks. Frontiers in Earth Science, 3. https://doi.org/10.3389/feart.2015.00004
72. Pearson, P. N., Van Dongen, B. E., Nicholas, C. J., Pancost, R. D., Schouten, S., Singano, J. M., & Wade, B. S. (2007). Stable warm tropical climate through the Eocene Epoch. Geology, 35(3), 211. https://doi.org/10.1130/G23175A.1
73. Peterse, F., Kim, J.-H., Schouten, S., Kristensen, D. K., Koç, N., & Sinninghe Damsté, J. S. (2009). Constraints on the application of the MBT/CBT palaeothermometer at high latitude environments (Svalbard, Norway). Organic Geochemistry, 40(6), 692-699. https://doi.org/10.1016/j.orggeochem.2009.03.004
74. Pierrehumbert, R. T. (2002). The hydrologic cycle in deep-time climate problems. Nature, 419(6903), 191-198. https://doi.org/10.1038/nature01088
75. Reghellin, D., Coxall, H. K., Dickens, G. R., & Backman, J. (2015). Carbon and oxygen isotopes of bulk carbonate in sediment deposited beneath the eastern equatorial Pacific over the last 8 million years. Paleoceanography, 30(10), 1261-1286. https://doi.org/10.1002/2015PA002825
76. Rohling, E. J., Marino, G., & Grant, K. M. (2015). Mediterranean climate and oceanography, and the periodic development of anoxic events (sapropels). Earth-Science Reviews, 143, 62-97. https://doi.org/10.1016/j.earscirev.2015.01.008
77. Schmitz, B., & Pujalte, V. (2007). Abrupt increase in seasonal extreme precipitation at the Paleocene-Eocene boundary. Geology, 35(3), 215. https://doi.org/10.1130/G23261A.1
78. Schouten, S., Hopmans, E. C., Schefuß, E., & Sinninghe Damsté, J. S. (2002). Distributional variations in marine crenarchaeotal membrane lipids: A new tool for reconstructing ancient sea water temperatures? Earth and Planetary Science Letters, 204(1-2), 265-274. https://doi.org/10.1016/S0012-821X(02)00979-2

79. Schreuder, L. T., Stuut, J.-B. W., Korte, L. F., Sinninghe Damsté, J. S., & Schouten, S. (2018). Aeolian transport and deposition of plant wax n-alkanes across the tropical North Atlantic Ocean. Organic Geochemistry, 115, 113-123. https://doi.org/10.1016/j.orggeochem.2017.10.010
80. Sexton, P. F., Norris, R. D., Wilson, P. A., Pälike, H., Westerhold, T., Röhl, U., Bolton, C. T., & Gibbs, S. (2011). Eocene global warming events driven by ventilation of oceanic dissolved organic carbon. Nature, 471(7338), 349-352. https://doi.org/10.1038/nature09826
81. Shackleton, N. J. (1986). Paleogene stable isotope events. Palaeogeography, Palaeoclimatology, Palaeoecology, 57(1), 91-102. https://doi.org/10.1016/0031-0182(86)90008-8
82. Sijp, W. P., England, M. H., & Huber, M. (2011). Effect of the deepening of the Tasman Gateway on the global ocean. Paleoceanography, 26(4), 2011PA002143. https://doi.org/10.1029/2011PA002143
83. Sinninghe Damsté, J. S. (2016). Spatial heterogeneity of sources of branched tetraethers in shelf systems: The geochemistry of tetraethers in the Berau River delta (Kalimantan, Indonesia). Geochimica et Cosmochimica Acta, 186, 13-31. https://doi.org/10.1016/j.gca.2016.04.033
84. Sinninghe Damsté, J. S., Rijpstra, W. I. C., Foesel, B. U., Huber, K. J., Overmann, J., Nakagawa, S., Kim, J. J., Dunfield, P. F., Dedysh, S. N., & Villanueva, L. (2018). An overview of the occurrence of ether- and ester-linked iso-diabolic acid membrane lipids in microbial cultures of the Acidobacteria: Implications for brGDGT paleoproxies for temperature and pH. Organic Geochemistry, 124, 63-76. https://doi.org/10.1016/j.orggeochem.2018.07.006
85. Sluijs, A., Pross, J., & Brinkhuis, H. (2005). From greenhouse to icehouse; organic-walled dinoflagellate cysts as paleoenvironmental indicators in the Paleogene. Earth-Science Reviews, 68(3-4), 281-315. https://doi.org/10.1016/j.earscirev.2004.06.001
86. Sluijs, A., Schouten, S., Donders, T. H., Schoon, P. L., Röhl, U., Reichart, G.-J., Sangiorgi, F., Kim, J.-H., Sinninghe Damsté, J. S., & Brinkhuis, H. (2009). Warm and wet conditions in the Arctic region during Eocene Thermal Maximum 2. Nature Geoscience, 2(11), 777-780. https://doi.org/10.1038/ngeo668
87. Song, X.-Y., Spicer, R. A., Yang, J., Yao, Y.-F., & Li, C.-S. (2010). Pollen evidence for an Eocene to Miocene elevation of central southern Tibet predating the rise of the High Himalaya. Palaeogeography, Palaeoclimatology, Palaeoecology, 297(1), 159-168. https://doi.org/10.1016/j.palaeo.2010.07.025
88. Speelman, E. N., Van Kempen, M. M. L., Barke, J., Brinkhuis, H., Reichart, G. J., Smolders, A. J. P., Roelofs, J. G. M., Sangiorgi, F., De Leeuw, J. W., Lotter, A. F., & Sinninghe Damsté, J. S. (2009). The Eocene Arctic Azolla bloom: Environmental conditions, productivity and carbon drawdown. Geobiology, 7(2), 155-170. https://doi.org/10.1111/j.1472-4669.2009.00195.x
89. Struck, J., Bliedtner, M., Strobel, P., Schumacher, J., Bazarradnaa, E., & Zech, R. (2020). Leaf wax <i>n</i>-alkane patterns and compound-specific <i>δ</i>¹³C of plants and topsoils from semi-arid and arid Mongolia. Biogeosciences, 17(3), 567-580. https://doi.org/10.5194/bg-17-567-2020
90. Taylor, K. W. R., Huber, M., Hollis, C. J., Hernandez-Sanchez, M. T., & Pancost, R. D. (2013). Re-evaluating modern and Palaeogene GDGT distributions: Implications for SST reconstructions. Global and Planetary Change, 108, 158-174. https://doi.org/10.1016/j.gloplacha.2013.06.011
91. Tegen, I., Harrison, S. P., Kohfeld, K., Prentice, I. C., Coe, M., & Heimann, M. (2002). Impact of vegetation and preferential source areas on global dust aerosol: Results from a model study. Journal of Geophysical Research: Atmospheres, 107(D21). https://doi.org/10.1029/2001JD000963
92. Ulfers, A., Zeeden, C., Voigt, S., Sardar Abadi, M., & Wonik, T. (2022). Half-precession signals in Lake Ohrid (Balkan) and their spatio-temporal relations to climate records from the European realm. Quaternary Science Reviews, 280, 107413. https://doi.org/10.1016/j.quascirev.2022.107413
93. Van Der Does, M., Brummer, G. A., Korte, L. F., & Stuut, J. W. (2021). Seasonality in Saharan Dust Across the Atlantic Ocean: From Atmospheric Transport to Seafloor Deposition. Journal of Geophysical Research: Atmospheres, 126(11), e2021JD034614. https://doi.org/10.1029/2021JD034614
94. Van Der Does, M., Brummer, G. A., Van Crimpen, F. C. J., Korte, L. F., Mahowald, N. M., Merkel, U., Yu, H., Zuidema, P., & Stuut, J. W. (2020). Tropical Rains Controlling Deposition of Saharan Dust Across the North Atlantic Ocean. Geophysical Research Letters, 47(5), e2019GL086867. https://doi.org/10.1029/2019GL086867
95. Van Der Ploeg, R., Cramwinckel, M. J., Kocken, I. J., Leutert, T. J., Bohaty, S. M., Fokkema, C. D., Hull, P. M., Meckler, A. N., Middelburg, J. J., Müller, I. A., Penman, D. E., Peterse, F., Reichart, G.-J., Sexton, P. F., Vahlenkamp, M., De Vleeschouwer, D., Wilson, P. A., Ziegler, M., & Sluijs, A. (2023). North Atlantic surface ocean warming and salinization in response to middle Eocene greenhouse warming. Science Advances, 9(4), eabq0110. https://doi.org/10.1126/sciadv.abq0110
96. Van Der Weijst, C. M. H., Van Der Laan, K. J., Peterse, F., Reichart, G.-J., Sangiorgi, F., Schouten, S., Veenstra, T. J. T., & Sluijs, A. (2022). A 15-million-year surface- and subsurface-integrated TEX 86 temperature record from the eastern equatorial Atlantic. Climate of the Past, 18(8), 1947-1962. https://doi.org/10.5194/cp-18-1947-2022
97. Van Hinsbergen, D. J. J., De Groot, L. V., Van Schaik, S. J., Spakman, W., Bijl, P. K., Sluijs, A., Langereis, C. G., & Brinkhuis, H. (2015). A Paleolatitude Calculator for Paleoclimate Studies. PLOS ONE, 10(6), e0126946. https://doi.org/10.1371/journal.pone.0126946

98. Varma, D., Hättig, K., Van Der Meer, M. T. J., Reichart, G., & Schouten, S. (2023). Constraining Water Depth Influence on Organic Paleotemperature Proxies Using Sedimentary Archives. Paleoceanography and Paleoclimatology, 38(6), e2022PA004533. https://doi.org/10.1029/2022PA004533
99. Vogts, A., Moossen, H., Rommerskirchen, F., & Rullkötter, J. (2009). Distribution patterns and stable carbon isotopic composition of alkanes and alkan-1-ols from plant waxes of African rain forest and savanna C3 species. Organic Geochemistry, 40(10), 1037-1054. https://doi.org/10.1016/j.orggeochem.2009.07.011
100. Wang, Q., Wyman, D. A., Li, Z.-X., Sun, W., Chung, S.-L., Vasconcelos, P. M., Zhang, Q., Dong, H., Yu, Y., Pearson, N., Qiu, H., Zhu, T., & Feng, X. (2010). Eocene north–south trending dikes in central Tibet: New constraints on the timing of east–west extension with implications for early plateau uplift? Earth and Planetary Science Letters, 298(1-2), 205-216. https://doi.org/10.1016/j.epsl.2010.07.046
101. Wattel-Koekkoek, E. J., & Buurman, P. (2004). Mean residence time of kaolinite and smectite-bound organic matter in Mozambiquan soils. Soil Science Society of America Journal, 68(1), 154-161.
102. Wattel-Koekkoek, E. J. W., Buurman, P., Van Der Plicht, J., Wattel, E., & Van Breemen, N. (2003). Mean residence time of soil organic matter associated with kaolinite and smectite. European journal of soil science, 54(2), 269-278.
103. Weijers, J. W. H., Lim, K. L. H., Aquilina, A., Sinninghe Damsté, J. S., & Pancost, R. D. (2011). Biogeochemical controls on glycerol dialkyl glycerol tetraether lipid distributions in sediments characterized by diffusive methane flux: TEX 86 IN SULFATE-METHANE TRANSITION ZONE. Geochemistry, Geophysics, Geosystems, 12(10), n/a-n/a. https://doi.org/10.1029/2011GC003724
104. Weijers, J. W. H., Schefuß, E., Kim, J.-H., Sinninghe Damsté, J. S., & Schouten, S. (2014). Constraints on the sources of branched tetraether membrane lipids in distal marine sediments. Organic Geochemistry, 72, 14-22. https://doi.org/10.1016/j.orggeochem.2014.04.011
105. Weijers, J. W. H., Schouten, S., Spaargaren, O. C., & Sinninghe Damsté, J. S. (2006). Occurrence and distribution of tetraether membrane lipids in soils: Implications for the use of the TEX86 proxy and the BIT index. Organic Geochemistry, 37(12), 1680-1693. https://doi.org/10.1016/j.orggeochem.2006.07.018
106. Westerhold, T., Marwan, N., Drury, A. J., Liebrand, D., Agnini, C., Anagnostou, E., Barnet, J. S. K., Bohaty, S. M., De Vleeschouwer, D., Florindo, F., Frederichs, T., Hodell, D. A., Holbourn, A. E., Kroon, D., Lauretano, V., Littler, K., Lourens, L. J., Lyle, M., Pälike, H., … Zachos, J. C. (2020). An astronomically dated record of Earth's climate and its predictability over the last 66 million years. Science, 369(6509), 1383-1387. https://doi.org/10.1126/science.aba6853
107. Westerhold, T., Röhl, U., Donner, B., & Zachos, J. C. (2018). Global Extent of Early Eocene Hyperthermal Events: A New Pacific Benthic Foraminiferal Isotope Record From Shatsky Rise (ODP Site 1209). Paleoceanography and Paleoclimatology, 33(6), 626-642. https://doi.org/10.1029/2017PA003306
108. Westerhold, T., Röhl, U., Frederichs, T., Agnini, C., Raffi, I., Zachos, J. C., & Wilkens, R. H. (2017). Astronomical calibration of the Ypresian timescale: Implications for seafloor spreading rates and the chaotic behavior of the solar system? Climate of the Past, 13(9), 1129-1152. https://doi.org/10.5194/cp-13-1129-2017
109. Williams, C. J. R., Lunt, D. J., Salzmann, U., Reichgelt, T., Inglis, G. N., Greenwood, D. R., Chan, W., Abe-Ouchi, A., Donnadieu, Y., Hutchinson, D. K., De Boer, A. M., Ladant, J., Morozova, P. A., Niezgodzki, I., Knorr, G., Steinig, S., Zhang, Z., Zhu, J., Huber, M., & Otto-Bliesner, B. L. (2022). African Hydroclimate During the Early Eocene From the DeepMIP Simulations. Paleoceanography and Paleoclimatology, 37(5), e2022PA004419. https://doi.org/10.1029/2022PA004419
110. Xiao, W., Wang, Y., Liu, Y., Zhang, X., Shi, L., & Xu, Y. (2020). Predominance of hexamethylated 6-methyl branched glycerol dialkyl glycerol tetraethers in the Mariana Trench: Source and environmental implication. Biogeosciences, 17(7), 2135-2148. https://doi.org/10.5194/bg-17-2135-2020
111. Yedema, Y. W., Sangiorgi, F., Sluijs, A., Sinninghe Damsté, J. S., & Peterse, F. (2023). The dispersal of fluvially discharged and marine, shelf-produced particulate organic matter in the northern Gulf of Mexico. Biogeosciences, 20(3), 663-686. https://doi.org/10.5194/bg-20-663-2023
112. Zachos, J. C., Röhl, U., Schellenberg, S. A., Sluijs, A., Hodell, D. A., Kelly, D. C., Thomas, E., Nicolo, M., Raffi, I., Lourens, L. J., McCarren, H., & Kroon, D. (2005). Rapid Acidification of the Ocean During the Paleocene-Eocene Thermal Maximum. Science, 308(5728), 1611-1615. https://doi.org/10.1126/science.1109004
113. Zachos, J. C., Stott, L. D., & Lohmann, K. C. (1994). Evolution of Early Cenozoic marine temperatures. Paleoceanography, 9(2), 353-387. https://doi.org/10.1029/93PA03266
114. Zahirovic, S., Matthews, K. J., Flament, N., Müller, R. D., Hill, K. C., Seton, M., & Gurnis, M. (2016). Tectonic evolution and deep mantle structure of the eastern Tethys since the latest Jurassic. Earth-Science Reviews, 162, 293-337. https://doi.org/10.1016/j.earscirev.2016.09.005
115. Zeebe, R. E., Westerhold, T., Littler, K., & Zachos, J. C. (2017). Orbital forcing of the Paleocene and Eocene carbon cycle: ORBITAL FORCING PALEOCENE-EOCENE C CYCLE. Paleoceanography, 32(5), 440-465. https://doi.org/10.1002/2016PA003054
116. Zell, C., Kim, J.-H., Hollander, D., Lorenzoni, L., Baker, P., Silva, C. G., Nittrouer, C., & Sinninghe Damsté, J. S. (2014). Sources and distributions of branched and isoprenoid tetraether lipids on the Amazon shelf and fan: Implications for the use of GDGT-based proxies in marine sediments. Geochimica et Cosmochimica Acta, 139, 293-312. https://doi.org/10.1016/j.gca.2014.04.038

117. Zhang, Y. G., Pagani, M., & Wang, Z. (2016). Ring Index: A new strategy to evaluate the integrity of TEX 86 paleothermometry. Paleoceanography, 31(2), 220-232. https://doi.org/10.1002/2015PA002848
118. Zhang, Y. G., Zhang, C. L., Liu, X.-L., Li, L., Hinrichs, K.-U., & Noakes, J. E. (2011). Methane Index: A tetraether archaeal lipid biomarker indicator for detecting the instability of marine gas hydrates. Earth and Planetary Science Letters, 307(3-4), 525-534. https://doi.org/10.1016/j.epsl.2011.05.031
119. Zhu, C., Weijers, J. W. H., Wagner, T., Pan, J.-Ming., Chen, J.-F., & Pancost, R. D. (2011). Sources and distributions of tetraether lipids in surface sediments across a large river-dominated continental margin. Organic Geochemistry, 42(4), 376-386. https://doi.org/10.1016/j.orggeochem.2011.02.002